Impurity transport modelling in the scrape off layer of the MAST tokamak using DIVIMP-OSM-EIRENE and carbon injection

Mr. Huw Jonathan Leggate

A dissertation submitted in fulfilment of the
requirements for the award of
Doctor of Philosophy (Ph.D.)

presented to the

School of Physical Science
Faculty of Science and Health
Dublin City University

Supervisor: Prof. Miles M. Turner

December, 2015

Declaration

I hereby certify that this material, which I now submit for assessment on the programme of study leading to the award of Doctor of Philosophy is entirely my own work, that I have exercised reasonable care to ensure that the work is original, and does not to the best of my knowledge breach any law of copyright, and has not been taken from the work of others save and to the extent that such work has been cited and acknowledged within the text of my work.

Signed .....

Huw Jonathan Leggate

Student ID: 58116192

Date: December 21, 2015

Contents

CONTENTS

Acknowledgements

I would first like to thank my Supervisor Miles Turner for his long lasting support and trust, in particular in allowing me to explore my experimental side in the early stages of this work, also my thanks go to my co-supervisor Steven Lisgo for providing both ideas and knowledge. I would also like to thank the support staff in the National Centre for Plasma Science and Technology, in particular Samantha Fahy, Sarah Hayes and Sheila Boughton, without whom very little of this work would have been possible.

Several past members of the NCPST also helped me during this time, James Lawlor, Niall O'Connor and Dave O'Farrell, who successfully prevented me from electrocuting myself in the lab and also shared a mutual appreciation of beer. Also in the laboratory, Pat Wogan, Nishant Sirse, Gurusharan Singh Gogna and Mubarak Mujawar for providing guidance. Shantanu Karkari for asking awkward questions and Sarveshwar Sharma also for asking awkward questions as well as a constant smiling presence and many knowledgeable discussions on cricket. I would also like to mention more re-

cent colleagues at DCU, Nina Hanzlikova, Sean Kelly and Samir Kechkar for their help and occasional heated discussions.

I would not have completed this work without the generous support of all those at the Culham Science Centre, in particular James Harrison, Andrew Thornton, Andrew Kirk, Geoff Fishpool, Scott Allan, Sarah Elmore, Scott Silburn, Robert Stephen, Ian Fitzgerald, Brian Lloyd and William Morris, apologies for those I have missed off this list.

I would like to express my thanks and love to my dear friend David Norland, who is not here to see the completion of this work but throughout my life always kept me honest and truthful.

The support of my wife Claire McKenna has been invaluable and I will be ever grateful for her ability to remain fun and loving under enormous pressure.

I would like to thank Father Christmas for making Cian smile.

My greatest thanks go to my Mother and Father, Gaynor and Peter, who have put up with considerably more than should have been and are still most wonderfully loving and supportive.

This work was part-funded by the RCUK Energy Programme [under grant EP/I501045] and by the European Communities. To obtain further information on the data and models underlying this paper please contact PublicationsManager@ccfe.ac.uk. The views and opinions expressed herein do not necessarily reflect those of the European Commission or the ITER Organisation.

Publications

- *Divertor impurity injection using high voltage arcs for impurity transport studies on the Mega Amp Spherical Tokamak*, H. J. Leggate, S. W. Lisgo, J. R. Harrison, S. Elmore, S. Y. Allan, R. C. Gaffka, R. C. Stephen and M. M. Turner, Review of Scientific Instruments, 85, 123503 (2014);`http://dx.doi.org/10.1063/1.4903352`

- *Carbon injection into MAST L-mode and H-mode plasmas as an indicator of impurity transport*, H. J. Leggate, J.R. Harrison, S.A. Silburn and M.M. Turner, 41^{st} EPS Conference on Plasma, Berlin, Germany, 23-27 June, 2014

- *Impurity transport studies using fast imaging of injected carbon on the MAST tokamak*, H. J. Leggate, S. W. Lisgo, J. R. Harrison, S. Elmore, S. Y. Allan and M. M. Turner, 39^{th} EPS Conference on Plasma Physics, Stockholm, Sweden, 2-6 July, 2012

List of Figures

List of Tables

Abstract

Impurity transport modelling in the scrape off layer of the MAST tokamak using DIVIMP-OSM-EIRENE and carbon injection

Mr. Huw Jonathan Leggate

Non-hydrogenic impurities play a significant role in the performance of magnetically confined fusion devices, causing increased radiation and dilution of the Deuterium-Tritium fuel isotopes. Impurities are generated at the plasma wall interfaces as well as being deliberately introduced into the plasma in order to reduce heat loads to the vessel walls. The quantity of impurities reaching the core plasma is determined by the impurity source and the nature of transport in the plasma core and scrape-off layer. Direct measurements of impurity transport have been made by injecting carbon ions into the MAST tokamak using an electrical discharge between 2 carbon electrodes. The emission of the resultant carbon plumes was measured by 2 cameras operating at $75kHz - 100kHz$ mounted on the MAST vessel. The resultant transport of the carbon ions parallel to the background magnetic field was then compared against simulation using the DIVIMP-OSM-EIRENE code.

CHAPTER 1

Introduction

An understanding of transport phenomena in the Scrape-Off Layer (SOL) of tokamak plasmas is of key importance in the development of next generation fusion devices such as ITER [2]. Both the control of the heat load on plasma facing components and the control of impurities including helium ash removal are critically dependent on SOL transport. An improved understanding of the processes in the SOL may also provide insight into other plasma processes associated with the plasma boundary such as the edge transport barrier present in H-mode discharges. It is useful at this point to make a distinction between the plasma edge and the SOL, the former covers not only the region outside the Last Closed Flux Surface (LCFS) of the plasma but extends a short distance inwards from the LCFS, covering the H-mode edge transport barrier and associated complex atomic physics. The SOL, although included in the term edge plasma, stops at the last closed flux surface. This

thesis deals only with SOL physics and will use the terms SOL and plasma boundary interchangeably.

Over the first few decades of fusion research little attention was paid to the plasma boundary. However, the introduction of the diverted tokamak [3] and the discovery of the H-mode [4] focused attention on the problems of impurity transport into the core plasma via the SOL and on the higher levels of power loading on the small plasma wetted areas of the first wall. Since then the resources directed to diagnosing and modelling the plasma boundary have increased significantly. Much of the early results of this work are documented in a book written by Peter Stangeby, The Plasma Boundary of Magnetic Fusion Devices[5], which also explores the foundations of the physics of the plasma boundary. Since this publication, efforts towards an improved understanding have continued and a large body of work on the edge of tokamak plasmas now exists. This thesis aims to add to this work through an understanding of the transport of impurities in the tokamak divertor and here briefly describes the mechanisms affecting this as well as the experimental and computational methods commonly used.

1.1 Edge plasma transport

1.1.1 Parallel and perpendicular transport

The transport of impurities is naturally dependant on the hydrogenic background plasma itself and the transport processes operating within it. In general plasma transport parallel to the local magnetic field is orders of magnitude greater than transport perpendicular to the field lines. This makes it useful to treat parallel transport independently from other directions of transport. Parallel flows exist in the SOL, primarily driven by particle sources

arising from the ionisation of neutrals from the targets and main chamber wall, by cross field diffusion across the separatrix from the bulk plasma and particle sinks present at the targets. These sources and sinks create variations in the plasma pressure along the SOL resulting in pressure gradient forces $-\frac{1}{n}\frac{dp}{dx}$ that drive flows in the SOL. The large source at the separatrix mean that these flows are often, though not always directed along the magnetic field towards the divertor targets. The fluid is transported along field lines with a velocity of the order the plasma sound speed c_s where[5]

$$c_s = [(\gamma_e Z k T_e + \gamma_i k T_i)/m_i]^{1/2} \approx \sqrt{\frac{2kT_e}{m_i}} \tag{1.1}$$

where T_e and T_i are the electron and ion temperatures, m_i is the ion mass and γ_e and γ_i are the adiabatic indices of the electrons and ions. For typical SOL temperatures in the range 1-100 keV and assuming $T_e = T_i$, the sound speed is of order $10^4 - 10^5 ms^{-1}$. The SOL length $L \approx \pi R q$ is typically $\sim$ 50m, giving a typical dwell time in the SOL of $\tau_{SOL} \approx$ 1ms. This estimate of the SOL dwell time relies on $\nabla T = 0$, which in a tokamak plasma is not the case. This approximation of an isothermal SOL is one feature of what is known as the simple SOL, when temperature gradients are included the SOL is referred to as complex.

Cross-field plasma velocities $v_\perp$ are often orders of magnitude less than the fast parallel flow $v_\parallel$, so that the SOL width is very small. If one makes the assumption that cross-field transport is diffusive [6],

$$v_\perp \approx D_\perp / l_\perp \tag{1.2}$$

where $l_\perp$ is the characteristic density scale length and $D_\perp$ is the cross-field diffusion coefficient, then the SOL width is given by

$$\lambda_{SOL} \approx \left[\frac{D_\perp L}{c_s}\right]^{1/2} \tag{1.3}$$

However, diffusivities calculated from first principles lead to SOL widths that are considerably less than those observed experimentally[7, 8]. This leads to the conclusion that cross field diffusion is not sufficient to account for cross-field transport in the SOL, and other mechanisms such as particle drifts and turbulence are likely to play a significant role.

1.1.2 Radial asymmetry

From early on in tokamak development it was observed that strong asymmetries existed in temperature, density and power measurements measurements between the inner and outer targets of divertor discharges [9] [10] [11]. Temperature and power are seen to be significantly higher on the outboard divertor, while plasma density is higher on the inboard divertor. These asymmetries can be largely explained due to the geometric configuration of tokamaks. Firstly the outboard surface area of a tokamak discharge is several times larger than the inboard surface area, leading to an increased power flux across the separatrix into the outboard SOL assuming uniform power flow density over the SOL. A second effect is that of flux compression on the outboard side due to Shafranov shift, which increases the power density to the outboard SOL and hence outboard divertor target based on the assumption that cross field transport is dependent on spatial gradients.

The observed asymmetry is highly dependent on the plasma configuration. Double null configuration experiments on the PDX tokamak have shown a ratio in deposited energy between the inner and outer divertor targets of ~ 9[9]. Single null configurations typically showed much less asymmetry[12], closer to a ratio of 2. This difference can be heuristically explained by the

connection between the inner and outer SOL for single null discharges, the fast parallel transport acts to equalise temperature and density across the SOL.

Although the in/out asymmetries can be partially explained by geometric considerations continued research showed that the asymmetries also depend on the direction of the toroidal magnetic field B_T [13][14] and on the discharge density[15], with the asymmetries increasing as density increases until both divertor targets enter the detached regime when the asymmetries all but disappear.

1.1.3 Particle drifts

When searching for mechanisms to drive the change in asymmetry with the direction of magnetic field it is natural to look for forces acting on the plasma fluid that are themselves dependent on the magnetic field. The toroidal plasma current present in tokamak plasmas is driven by the toroidal electric field E_ϕ created by the transformer action of the central solenoid. This field causes ions in the SOL to drift towards the inner or outer targets depending on the direction of B_T. The direction of B_T is best defined using the direction of the induced $\mathbf{B} \times \nabla B$ drift[6],

$$\mathbf{v}_{\nabla \mathbf{B}} = \pm \frac{v_\perp^2 m}{2eB^3} \mathbf{B} \times \nabla \mathbf{B} \tag{1.4}$$

where $v_\perp$ is the gyroscopic speed and m is the mass of the species. This drift is vertical and for the direction of 'normal' clockwise B_T is downwards towards the targets for ions and upwards for electrons. For ∇B drift towards the targets the E_ϕ ion drift is directed towards the inner target, independent of the direction of plasma current[5].

Aside from the toroidally induced drifts, the electric fields present in the SOL also affect particle transport in the form of $\mathbf{E} \times \mathbf{B}$ drifts [16]

$$v_{\mathbf{E}\times\mathbf{B}} = \frac{\mathbf{E} \times \mathbf{B}}{B^2} \tag{1.5}$$

Electric fields exist throughout the SOL, affecting both parallel and perpendicular transport. Radial electric fields due to the temperature gradient across the SOL cause poloidal drifts and the poloidal electric fields along the SOL cause radial drifts, strong fields close to the targets due to the plasma sheath also cause radial drifts. It should be noted that the drifts do not depend on the sign of the electric charge, so electrons and ions are affected in the same way and no charge separation occurs.

The poloidal $\mathbf{E_r} \times \mathbf{B}$ drift acts in the same direction as the standard parallel flow seen in the SOL, for $\mathbf{B} \times \nabla B$ downwards the drifts tend to increase density at the outer target and decrease density at the inner. This pressure imbalance should then result in plasma flow from the outer to inner divertor. Radial $\mathbf{E}_\theta \times \mathbf{B}$ particle drifts cause a particle flux across the separatrix, for $\mathbf{B} \times \nabla B$ downwards the flux is from the SOL into the main plasma on the outer SOL and from the main plasma into the SOL on the inboard side. In the simplest case this flux creates a source at the inboard SOL which then drives plasma flow from the inner to outer targets. One would then expect an increase in density at the inner target and a drop in target temperature.

Pressure gradient induced drifts are also present in the SOL, known as diamagnetic drifts

$$v_{\nabla p} = \frac{\mathbf{B} \times \nabla p}{enB^2} \tag{1.6}$$

These drifts are divergence free and therefore do not result in net plasma flow to the divertor targets [17]. However $v_{\nabla p}$ is dependent on the sign of

the charge and so ion and electron drifts are in opposite directions, leading to currents in the SOL.

Drifts in the SOL can also contribute to the parallel flow. The ∇B drift(1.4) causes ions and electrons to drift vertically in opposite directions. The curvature drift[6]

$$v_{curv} = \pm \frac{v_{\parallel}^2 m}{eB^3} \mathbf{B} \times \nabla B \tag{1.7}$$

due to the curvature of the magnetic field lines acts in the same direction and these two drifts result in vertical charge separation. This then drives parallel currents in the SOL that contribute to parallel flow in the SOL, known as Pfirsch-Schluter (P-S) flow. Poloidal $E_r \times B$ drift also contributes to the P-S flow directly, though does not contribute to the Pfirsch-Schluter currents as the drift direction is independent of species charge. An important prediction of P-S flow is that the flow velocity will be at a maximum at the outer midplane and a negative minimum at the inner midplane, changing with field direction.

The drifts present in the SOL play a significant role, a simple example illustrates this, estimating the poloidal $\mathbf{E} \times \mathbf{B}$ drift velocity as[5],

$$v_{\mathbf{E}\times B} \approx \frac{3kT_e}{e\lambda_{T_e} B} \tag{1.8}$$

where $\lambda_{T_e} = 10^{-2} m$ is the electron temperature decay length, $T_e = 25eV$ and $B = 3T$ gives $v_{\mathbf{E}\times B} \approx 2500 ms^{-1}$. A typical magnetic pitch angle of 10 degrees gives a poloidal projection of the sound speed estimated previously (1.1) of approximately $2000ms - 20000ms$, so in this example the drift velocity is at the lower end of the range of sound speeds and would be likely to have an observable effect on the SOL.

1.1.4 Flow reversal

One might expect parallel plasma flow in the SOL to be towards the targets at all points, taking particles that have diffused across the separatrix towards the targets. However, it has been shown [18] that under certain conditions the plasma flow can reverse close to the separatrix. This has been verified experimentally [19] [20] though the exact mechanisms governing this effect are not fully understood. One basic explanation [5] is that of radial temperature gradients across the SOL that allow neutrals from the walls of the divertor to cross the outer (cooler) part of the SOL and become ionised close to the separatrix upstream from the target, introducing a particle source potentially greater than the sink available at the target. Particle balance is satisfied by flow away from this over dense region towards the main plasma. However, observations have shown that flow-reversal can be instigated by reversing the toroidal magnetic field [21] [20] implying that B_T dependent plasma drifts and associated flows also play a role. Flow-reversal is of particular importance as it can allow the transport of impurities from the targets in to the main plasma, which is problematic for future reactor design, see 1.2.1.

1.1.5 Turbulence

In recent work on asymmetries, flow reversal and plasma transport has started to include turbulence as a significant and potentially dominant process[8, 22]. It has long been recognised that turbulence was likely to play a major role in tokamak plasmas but it is only recently that high speed diagnostics and High Performance Computing (HPC) environments have allowed the subject to be more fully explored. Though the effect of turbulence on plasma transport is far from fully understood it is clear that it plays a ma-

jor role in cross-field transport [23]. The first indication that a turbulent explanation was required was the large SOL widths observed in experiment, considerably greater than that expected due to purely diffusive transport[24], 1.3.

Turbulent transport in the plasma core has been shown to have the characteristics of drift-Alfvén turbulence[25, 26]. Edge turbulence is less easy to characterise, though it appears to be dominated by large cross-field transport events known as 'blobs' [23]. The turbulent transport of these blobs has been suggested to be interchange-mode-like in character[27] while another approach[28] suggests radial advection of the blob structures. Detailed investigation of the edge turbulence has shown that the fluctuations are intermittent and strongly non-Gaussian with the probability distribution function of density fluctuations being asymmetric and having tails that are consistent with exponential decay of probability with fluctuation amplitude[29, 30]. It is also important to note the large range of length scales associated with the turbulent fluctuations[31]. These structures have been observed experimentally [32, 33] and understanding their dynamics is key to understanding SOL transport.

The effect of turbulent fluctuations on parallel flow is poorly understood. It is likely that the convective cells caused by plasma blobs generate sheared zonal flows[34], however sheared flows tend to suppress turbulence [35], so that parallel flows and turbulence are likely to be strongly coupled. Turbulence may also play a strong role in flow asymmetries, for double null discharges parallel flow at the mid-plane inner SOL is much weaker than flows in the outer SOL, while for single null discharges the difference is much less pronounced. It has been suggested that poloidal gradients caused by ballooning induced turbulence in the outer SOL drive flows that in single

null discharges also affect the inner SOL[36]. For double-null discharges the inner SOL particle flux has been measured to be considerably lower than the outboard side [37], which is again consistent with ballooning-like turbulence.

1.2 Impurities

1.2.1 The effect of impurities on the plasma

Impurities are defined as any element other than the deuterium/tritium fuel that composes the main chamber plasma, this includes the helium ash that is the result of the D-T fusion reaction. The main effect of these impurities is to cool the plasma via radiation, which directly affects plasma performance. The radiation from any given element is highly dependent on the charge on that element and the plasma temperature. Generally, higher Z impurities radiate more than lower Z impurities and so are undesirable in a fusion device. For fully ionised impurities radiation is caused by Bremsstrahlung losses due to collisions with electrons and ions and is approximately given by [38]

$$W_b = 0.5 \times 10^{-24} n_e n_i Z^2 T^{1/2} W/m^3 \tag{1.9}$$

The Z^2 dependence immediately shows the problem of high Z impurities. To add to this, high Z impurities are more likely to retain some of their inner electrons, even at the high energies found in tokamak plasmas ($\approx 10keV$). This allows radiation due to excitation of electrons and provides a much higher radiative efficiency.

As well as cooling by radiation the impurity ions can cause an effect known as fuel dilution. The plasma β, the total plasma pressure over the magnetic pressure $B^2/2\mu_0$ cannot exceed the Troyon β-limit[6]

$$\beta_{max}[\%] = \frac{2.8 I_p}{aB} \tag{1.10}$$

As all electrons and ions contribute to the plasma pressure and therefore β the increased number of electrons from high Z impurities can quickly cause the plasma to approach this limit, even for low impurity fractions.

Low-Z impurities can also cause current profile contraction due to radiation near the plasma edge, where the temperatures are relatively low and some electrons can remain bound to the impurity ion. This potentially strong radiation can reduce the plasma conductivity to a point where the current profile contracts causing high current gradients inside the q=2 surface[6] which can then lead to plasma instabilities.

As well as these negative effects impurities can also be beneficial, notably by radiative cooling of the SOL, reducing the heat load on the divertor targets. Radiative cooling of the H-mode pedestal via impurities has also been used to control the heat load on the targets due to Edge Localised Modes (ELMs) [39].

1.2.2 Impurity generation

Impurities in tokamaks are primarily generated by either chemical or physical sputtering. Physical sputtering is the principle mechanism in impurity generation and occurs when an energetic particle striking a solid surface transfers enough momentum to eject an atom from the solid lattice. This process occurs on all plasma wetted areas but can also occur on surfaces a large distance away from the main plasma due to the escape of energetic charge-exchange neutrals. Lower energy particles can cause chemical sputtering when impacting on a carbon surface, the chemical potential energy of hydrogenic or oxygen atoms or ions can break carbon bonds and allow the

creation of $C-D$ or other reactive compounds. This can easily result in the emission of volatiles such as CH_4. In cool dense divertor plasmas chemical sputtering can in fact dominate over physical sputtering[40]. Once an impurity has entered the main plasma it is likely at some point to return to the wall, potentially resulting in self-sputtering and increasing the impurity content of the plasma. Gaseous impurities can also add to the impurity source through recycling at the targets.

As well as impurities entering the plasma from vessel structures there exists a completely unavoidable source of impurities in any burning plasma. Helium produced by the D-T reaction is an unwanted impurity in the bulk plasma and as a gas is also recycled at the targets. This is a serious problem for future burning plasma devices due to the conflicting requirements to reduce the impurity source to the main plasma while attempting to remove helium ash.

1.2.3 Impurity transport

Stangeby[5] provides a useful analysis of the primary forces acting on impurities parallel to the magnetic field. A basic treatment leads to five force terms acting on the plasma, the electrostatic force, the pressure gradient force, a friction force and forces due to ion and electron gradients.

$$F_Z = ZeE - \frac{1}{n_Z}\frac{dp_Z}{ds} + m_Z\frac{(v_i - v_Z)}{\tau_s} + \alpha_e\frac{d(kT_e)}{ds} + \beta_i\frac{d(kT_i)}{ds} + ... \quad (1.11)$$

where Z is the impurity species atomic number, n_Z is the impurity species density in $particles/m^3$, p_Z the impurity pressure in Pa, v_i and v_Z are the hydrogenic ion and impurity ion velocities respectively, τ_s is the impurity stopping time, T_e and T_i are the electron and ion temperatures, s is the

parallel distance along the field line and α_e and β_i are coefficients that depend primarily on Z.

The electrostatic force ZeE is simply the force exerted on the charged impurity ions by the parallel electric field present in the SOL. The pressure gradient force $-\frac{1}{n_Z}\frac{dp_Z}{ds}$ acts in the direction opposite to ∇P_Z due to the imbalance of pressure on each side of a given volume. The friction force $m_Z\frac{(v_i - v_Z)}{\tau_s}$ is due to the background flow of the hydrogenic plasma and acts in the same direction as the flow, generally towards the targets.

The final two terms are slightly less intuitive and are due to the collision cross-section and hence collision frequency between impurities and either electrons or hydrogenic ions having an inverse dependence on temperature. Ions or electrons colliding with the impurity ions will have travelled on average λ_{ii} or λ_{ee} since their last collision with another similar species, meaning that the average temperature and therefore collision frequency for ions or electrons impacting the impurity ions from the cooler side will be higher and more momentum will be transferred than for ions or electrons impacting from the hotter side. This drives impurity ions up the temperature gradient, in general away from the targets, see figure 1.1

A more rigorous treatment of these forces is presented by Spitzer [41], in which collisions between particles are dealt with from first principles. However the Spitzer treatment assumes a constant temperature plasma and so does not include the ion and electron temperature gradient terms. A more detailed treatment including temperature gradients has been carried out by Reiser[42] that includes these terms.

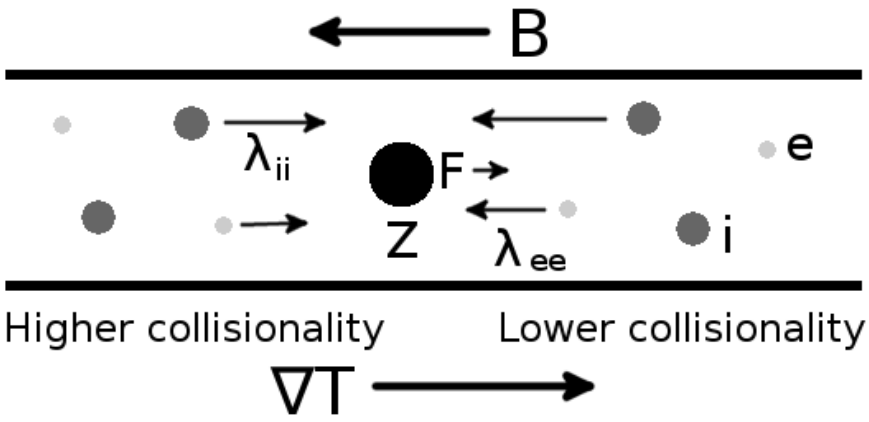

Figure 1.1: The temperature gradient force drives impurities up the temperature gradient. Ions and electrons impacting the impurity ion Z from the lower temperature side will have lower average temperatures and collision frequency than ions and electrons from the hotter side. They will therefore transfer less momentum to the impurity ion resulting in a net force F in the direction of increasing temperature.

1.3 Plasma boundary diagnostics and experimental techniques

1.3.1 Principle plasma boundary diagnostics

A variety of diagnostics are used in the edge plasma, the three most common techniques, Langmuir probes, spectroscopic imaging and Thomson scattering are described below.

Langmuir probes

A sufficiently negatively biased surface in contact with the plasma will repel all electrons, positive ions will flow to the surface causing a current j^i_{sat} that

is independent of the applied voltage. Assuming $T_i = T_e$ this saturation current is given by

$$j^i_{sat} = en_e c_s \tag{1.12}$$

As the bias is increased electrons begin to reach the surface and the net current decreases until it reaches zero at the floating potential V_f when $j_i = j_e$. The measured current is given by

$$I = (j_i + j_e)A = j_i(1 - exp(e(V - V_f)/T_e))A \tag{1.13}$$

where A is the projected area of the probe, V is the bias voltage relative to the plasma and j_i, j_e are the current densities due to electrons and ions. As the voltage is further increased ions are prevented from reaching the surface and an electron saturation current is reached. By sweeping the bias voltage one can determine the electron temperature and density. This is the single electrode Langmuir probe, double and triple probe configurations are also possible where probes are biased to different levels with respect to each other.

Langmuir probes are cheap and robust and provide one of the most important tokamak diagnostics. Several hundred may be found located in the typical tokamak divertor and they provide valuable information for experiment and modelling. Reciprocating probes also allow the use of Langmuir probes inside the SOL, however the probe itself will perturb the plasma and can only be in contact with the plasma for short periods of time.

A pair of Langmuir probes aligned with **B** and with the collection faces pointing outwards along the field allow one to make an estimate of parallel flow in the SOL. This technique relies on the premise that the ion current will be greater for the probe facing into the plasma flow. The ratio of the

upstream to downstream current being a function of the ratio of the flow velocity to the ion sound speed. Langmuir probes in this configuration are known as Mach probes. Mach probe measurements are however subject to significant errors and care must be taken in their interpretation[43].

Thomson scattering

Several non-invasive methods exist for probing the SOL. One of the most common of these is Thomson scattering, powerful infra-red or visible lasers are fired into the plasma and the light scattered from electrons is detected by spectroscopically filtered cameras. The total intensity of the scattered light is proportional to the plasma density and the electron temperature is calculated from the observed Doppler broadening of the scattered light due to the electron thermal motion. Thomson scattering systems exist on many tokamaks and typically provide electron temperature and density profile measurements at resolutions better than 1cm [44, 45].

Spectroscopic imaging

At the relatively cool temperatures in the SOL plasma emission is predominantly in the visible spectrum. This makes spectroscopic investigation of the SOL particularly useful. First the deuterium confinement time can be obtained by measuring the D_α line intensity and assuming that the rate of recombination is much less than the ionisation rate in the SOL. The effective plasma atomic number Z_{eff} can also be determined by measuring the background Bremsstrahlung radiation, which is a function of electron temperature, density and Z_{eff}. Aside from these two techniques edge line emission provides valuable information. Charge exchange between plasma ions, impurities or heating or diagnostic beams provides a measurement of T_i. Doppler

broadening and shifting of emission lines provides information on T_i, plasma rotation and SOL flow. Emission from impurities allows spatially resolved measurements of both impurity temperature and density as well as providing information on impurity transport and plasma flow. Helium and lithium are typically used in diagnostic beams while carbon has several strong visible lines, particularly CII at 514nm and CIII at 465nm. The presence of carbon in standard plasmas and the existence of these lines makes carbon a particularly useful tool in studying plasma flow. Modern fast cameras are able to image the emission on microsecond timescales and several experiments have been carried out using impurity injection to probe plasma flow, see section 1.3.2.

Other edge diagnostics

Aside from the diagnostics mentioned above a whole range of options exist for diagnosing the edge plasma. These include bolometer arrays for the measurement of radiated power, charge exchange recombination spectroscopy for density and temperature profiles of low Z impurities, reflectometry for edge density profiles and turbulence measurements, interferometry for integrated electron density measurements and divertor pressure gauges. Spectroscopic imaging of Lithium and Helium beams also provide measurements of temperature and density

Coherence imaging spectroscopy

Accurate measurements of plasma flow are particularly hard to achieve, Mach probes, already described here in 1.3.1 perturb the plasma and have a large measurement error. A method for passive measurements of plasma flow has been developed on the DIII-D tokamak using coherence imaging [46–48]. This

technique uses an imaging 2 beam interferometer; a fixed delay is introduced between the two beams at all positions on a 2D image of the plasma. An additional delay is then added which varies along one image direction and results in a set of parallel fringes superimposed on the image. Any phase change due to Doppler shifts arising from plasma flow cause a distortion in these fringes and comparison with an un-distorted calibration pattern using FFT techniques yields flow information. It should be noted that the spatial resolution differs between the horizontal and vertical directions, assuming the variable delay is introduced horizontally the vertical resolution is defined by the scale of the fringes which can be many pixels.

1.3.2 Impurity injection experiments

Stangeby [5] categorises impurity injection experiments into those using recycling and non-recycling elements. Experiments using recycling gases such as helium and argon are usually concerned with gaining an understanding of impurity retention and pumping. Obtaining information about local conditions is more difficult due to the competition between the injected source and any recycling that occurs after this, although valuable information can still be gained [49]. Experiments using non-recycling impurities can provide measurements of the parallel and poloidal drift velocities [50–52] and directly show the level of impurity screening and whether impurities can become trapped in the SOL [53, 54]. The primary method used for these types of studies is 2 dimensional spectroscopic imaging of the lower charge states of the impurity used. Carbon has been the most commonly used impurity due to its prevalence in many tokamaks, the ease with which it forms gaseous compounds with hydrogenic elements, the existence of strong visible emission lines and the availability of the carbon-13 isotope which allows postmortem

examination of carbon deposition from injected carbon.

Edge impurity injection experiments have been carried out on a range of tokamaks including DITE[54], TEXT[55], Alcator C-Mod[51], DIII-D[56], ASDEX Upgrade[57, 58], JET[59] and TEXTOR[60]. Various techniques are used and a selection of these are briefly discussed below.

Gas injection

Gas injection systems designed to inject trace quantities of gas into the SOL have been installed on several tokamaks. Recent experiments have been carried out on both Alcator C-Mod and DII-D using impurity injection for the study of local impurity transport and SOL flows. On Alcator C-Mod Gangadhara et al.[51] used a reciprocating fast scanning probe[61] to inject deuterated ethylene (C_2D_4) into the SOL at various depths. The gas injection had a typical duration of 10ms and injected approximately $\approx 5 \times 10^{16}$ molecules, resulting in $\approx 10^{17}$ carbon atoms. The carbon II and III lines where then imaged using gated CCD cameras. The aim of this study was to compare data obtained from the plume imaging with data previously obtained from fast scanning Langmuir/Mach probes, specifically to improve the understanding of parallel and $\mathbf{E} \times \mathbf{B}$ flows that affect the transport of impurities into the bulk plasma. The results clearly showed that the surface of the probe had a significant effect on the plume structure, causing jetting parallel to the local magnetic field. Transport modelling that includes this effect suggests that values for E_r obtained using probes are in error and that probes over-estimate the parallel flow to the divertor in the far SOL, suggesting that main chamber recycling and not target recycling is the dominant process in the Alcator C-Mod SOL.

A different approach has been taken at DIII-D where a Porous Plug Injec-

tor (PPI)[56, 62] has been developed that mimics the carbon impurity source due to chemical sputtering. This is achieved by siting a gas injector behind a porous graphite cap of diameter 4.2cm that has a regular square lattice of 1004 0.25mm holes drilled into its surface. This injector is mounted on the divertor materials evaluation system (DiMES) near the outer strike point in the DIII-D divertor. This allows a diffuse cloud of methane molecules to be injected into the divertor at an energy of approximately 0.05eV, similar to that expected from chemically sputtered hydrocarbons. The injection is distributed over an area that is large relative to the mean free path of the plasma-molecular processes being studied, allowing detailed studies of the photon emission of CH_4 molecules injected at known flow rates. This experiment has confirmed that the intrinsic chemical erosion yield is close to that measured in the laboratory.

Several experiments using gas injection have been carried out on ASDEX Upgrade [52, 58, 63] using $^{13}CH_4$. In these experiments gas is injected into the lower divertor at the end of a campaign, a selection of tiles close to the injection location is then removed and the deposition of carbon-13 studied. Differences in deposition are highlighted for forward and reversed fields [52], between H-mode and L-mode discharges[58] and for graphite and tungsten tiles[63]. These differences can be attributed to the effect of the $\mathbf{E} \times \mathbf{B}$ and $\mathbf{B} \times \nabla B$ forces and to the effect of surface roughness in the case of the different tile types. For certain L-mode shots significant upstream transport is observed which is not observed in either H-mode shots or when using lower puffing rates[58]. Carbon-12 has also been used on several machines [64–66] to study hydrocarbon fluxes and erosion yields by spectroscopic imaging of injected carbon.

Impurity injection experiments aiming to understand the levels of impu-

rities reaching the core due to chemical sputtering have also been carried out, an example of this being the studies on JET[59, 67]. The more recent of these[59] used methane injected from several ports in the JET divertor and midplane and at the top of the vessel. The core carbon content was then measured using charge exchange recombination spectroscopy and Z_{eff} measurements from visible Bremsstrahlung. The experiment was performed in a range of L-mode and H-mode plasma conditions and the carbon injection and transport to the core was modelled using the DIVIMP and EDGE2D codes (see section 1.4. Various observations were then made including increased penetration to the core from the private flux region compared to the rest of the SOL and increased penetration for limiter plasmas. It was also noted that close to the separatrix carbon transport is dominated by diffusion while further out it is dominated by parallel flow. It should be noted that this approach is fundamentally different to the other two methods mentioned previously as it does not use data on local SOL transport and relies completely on modelling to infer transport properties. Similar experiments designed to study the bulk penetration of gases such as neon and argon into the core have also been performed on JET[68]. These elements are likely to be used on future machines to reduce the power loading to the divertor through impurity seeding [39].

A supersonic gas injector[69] was developed for use on the NSTX[70] spherical tokamak. This injector was intended for both fuelling and diagnostic applications and is capable of injecting up to 10^{22} particles per second at velocities up to Mach 4 into the edge plasma.

Laser ablation and sublimation

Gas injection systems are intrinsically limited in the impurities that they can inject. They are also unable to inject impurities on very short timescales. Laser ablation systems are able to inject a variety of solid materials by focusing a high power laser beam onto a target inside the tokamak over very short timescales.

The laser ablation system on JET has been used to inject Tungsten, Hafnium and Nickel[71–73]. The system uses a ruby laser to fire pulses of up to 10J at a target positioned on the vessel wall, typically 10^{18} particles are ablated into the chamber, with around 5% of the particles reaching the plasma core. This system provides important information on core impurity transport and penetration, however the influx of high Z particles is highly perturbing and provides limited information on local edge transport. Experiments using laser ablation have also been carried out on several other machines including ASDEX Upgrade[74], TCV[75] and TEXT[55]. Experiments using laser ablation tend to rely heavily on spectroscopic imaging of the impurity emission, for heavy elements this emission is generally in the UV and X-ray, this and the complexity of the spectra make this area of work extremely challenging.

Silicon has been injected into ASDEX Upgrade using the Laser-blow-off technique in order to study core transport[74]. A significant increase in core transport is observed in plasmas with central electron-cyclotron heating, which is promising as a method for helium ash extraction in a burning reactor. A novel method for the injection of small quantities of high Z material has also been developed on ASDEX Upgrade[76]. A small heated chamber mounted on a probe head allows small quantities of suitable materials to be sublimated and then injected into the plasma. This allows high Z materi-

als to be injected in controllable quantities, although still over a relatively long timescale. Tungsten carbonyl [$W(CO)_6$] was used in experiment, this allows the tungsten particle flux to be accurately estimated by observing the emission from the carbon and oxygen ions.

1.4 Modelling Impurities in the Scrape-Off Layer

1.4.1 Approaches to Impurity Modelling

Two basic approaches are generally employed when modelling impurities in the edge plasma. The first of these is to use a multi-fluid approach and treat both the hydrogenic background plasma and the impurity particles as fluids. This approach has the disadvantage that impurities in lower charge states tend to exist only for a very short time and so are not in thermal equilibrium with the background plasma[42], these approaches can also be computationally very expensive[77]. However they do include the effect of the impurities themselves on the edge plasma and are therefore valuable tools. The other approach is to model the background plasma as a fluid, with or without the effect of neutrals and impurities, and then adopt a fully kinetic treatment for the impurity particles to be studied[78].

1.4.2 The Two-Point Model

The simplest approach to modelling the SOL while neglecting impurities uses two reference points, one at the target t and the other upstream at or close to the LCFS (u). This is known as the Two-Point model[12, 79] and despite its simplicity is able to replicate many observed plasma conditions[80]. The

upstream location can be taken as half way between the targets (assuming a single null divertor plasma) or at the midplane, the choice of location does not have a significant effect on the results.

Three basic assumptions are used in the two point model[5]:

1. Recycling neutrals are re-ionised in a thin layer close to the targets on the same field line as followed by the original ion that impacted the target. There is also no parallel flow along most of the SOL and no cross-field flow.

2. There is no friction between the plasma and the targets and no viscous effects so that the total pressure is constant along the flux tube.

3. The parallel power flux density is carried solely by conduction.

Following Stangeby these assumptions lead to a set of three equations containing three unknowns n_t, T_t, T_u,

$$2n_t T_t = n_u T_u \tag{1.14}$$

$$T_u^{7/2} = T_t^{7/2} + \frac{7}{2}\frac{q_\parallel L}{\kappa_{0e}} \tag{1.15}$$

$$q_\parallel = \gamma n_t k T_t c_{st} \tag{1.16}$$

with the specified constants L being the distance between the two points along the magnetic field, κ_{0e} the electron parallel conductivity coefficient and γ the sheath heat transmission coefficient. c_{st} is the sound speed at the target and the control parameters n_u and $q_\parallel$ are the upstream density and parallel power flux density.

It is possible to extend this basic model to include radiative and charge exchange power loss, momentum loss due to friction and viscous forces, non-zero parallel heat convection and energy lost by electrons re-ionising recycled neutrals, these extensions are described by Stangeby.

1.4.3 1D fluid modelling along B

The complexity of modelling the SOL essentially increases with the number of dimensions that one chooses to model. The two point model described above is a zero dimensional model, no attempt is made to model the relevant parameters as a function of parallel distance $s_{\|}$ along the SOL. In order to model these parameters one starts with the one dimensional velocity distribution given by the Fokker-Planck kinetic vector equation [5, 81]

$$v_x \frac{\partial f}{\partial x} + \frac{eE}{m}\frac{\partial f}{\partial v_x} = \frac{\partial f}{\partial t}\Big|_{coll} + S(x,v) \tag{1.17}$$

where $\partial f/\partial t|_{coll}$ is the change due to collisions other than events where particles are created or destroyed and S is the difference between particle creation and destruction rates. Taking moments of this equation by multiplying by $d\mathbf{v}, mv_x d\mathbf{v}, \frac{1}{2}mv_x^2 d\mathbf{v}$, etc. and integrating results in a set of fluid equations that describe the plasma in 1-dimension. A brief derivation of these can be found in Stangeby but they can be summarised by a set of three conservation equations in three unknowns n, v, T by assuming $T_e = T_i$ and $p = p_e + p_i$ and ignoring viscous stress,

Particle conservation

$$\frac{d}{dx}[nv] = S_p \tag{1.18}$$

Momentum conservation

$$\frac{d}{dx}[(m_i v^2 + 2kT)n] = -m_i v \bar{\sigma} \bar{v}_{in} n n_n \tag{1.19}$$

Energy conservation

$$\frac{d}{dx}\left[\frac{1}{2}(m_i v^2 + 5kT)nv - \kappa_{0e}T_e^{5/2}\frac{dT_e}{dx}\right] = Q_R + Q_E \tag{1.20}$$

where S_p is the net particle source, Q_R is the heating source due to net particle drift and Q_E is the power source due to hydrogenic recycling. These fluid equations require significantly less computational time to perform, however further approximations are required in order to close the equations. Ignoring heat conduction $q_\parallel$ allows one to do this. When self-collisionality is high the particle distribution tends to Maxwellian and $q_\parallel \to 0$, the equations then close with only convection appearing in the energy equation. When collisionality is lower an approximation can be made of $q_{\parallel cond} = -\kappa_0 T^{5/2} dT/dx$ this works for moderate collisionality but fails as collisionality becomes small. For a rigorous treatment in this regime it is necessary to calculate higher moments of the kinetic equation that may then be approximated in order to close the system.

When using these equations for modelling in one dimension it is common to view the SOL as being in one of two regimes, either sheath limited or conduction limited. The defining property of these regimes is the existence or lack of a significant parallel temperature gradient in the SOL.

The Sheath Limited Regime

The sheath limited regime is characterised by the absence of parallel temperature gradients in the SOL and low collisionality. For a given particle and power source from the bulk plasma the sheath at the targets defines the conditions in the SOL. This situation can occur without the need for parallel flow, high parallel conductivity and small temperature gradients can transmit all the power from the bulk plasma to the targets. For the case of low

heat conductivity it is parallel flow that must carry this power. It should be noted that T_i need not be constant, assuming that the assumption of $T_i = T_e$ is dropped.

The Conduction Limited Regime

In the absence of strong convective flows parallel conduction can become the limiting factor for the SOL properties although the sheath still plays an important role. Due to the lack of significant flow, recycling ionisation is assumed to occur very close to the targets so any flows that are present are confined to a thin region close to the targets. Large temperature gradients characterise this regime.

When modelling the sheath limited regime the obvious assumption to make is to treat T_e and T_i as constant parameters that can be obtained by some other means than the fluid equations. The energy conservation equation is not then required and ignoring collisions the particle and momentum conservation equations become

$$\frac{d}{dx}(nv) = S_p \tag{1.21}$$

$$\frac{d}{dx}(m_i n v^2 + nkT_i + nkT_e) = 0 \tag{1.22}$$

Plasma parameters calculated from these simplified equations agree surprisingly well with full kinetic treatments[5, 82], particularly considering that this system is completely collisionless.

In the conduction limited regime the isothermal assumption is invalid and parallel heat conduction is dominant. The choice of boundary conditions then becomes critical in this regime. It is possible to specify these boundary conditions entirely at the target and Langmuir probes(1.3.1) incorporated into

the target provide both density and temperature information. Other diagnostics such as Thomson scattering can then be used to further constrain the solution at other points along the SOL. The question of particle, momentum and energy sources also becomes more complicated in the conduction limited regime and it is usually necessary to employ a Monte-Carlo neutral code such as EIRENE[83] to calculate these sources. The effect of impurities, in particular radiation, can be dealt with in a similar way using a dedicated impurity code such as DIVIMP[84].

1.4.4 Modelling the SOL in 2 dimensions

Modelling of the SOL in 1 dimension naturally neglects any cross-field processes that occur. Several codes exist that use a multi-fluid approach to model the SOL in 2 dimensions and include the cross-field drift and diffusion terms that the 1 dimensional approach does not, notable examples being SOLPS[77, 85], EDGE2D[86, 87] and UEDGE[88, 89]. For all of these codes toroidal symmetry is assumed and the remaining 2 dimensions are radial and either along $\mathbf{B}$ or the projection of the parallel direction in the poloidal plane. The necessary boundary conditions for these codes are complex and great care must be taken at the four boundaries, the two targets, the LCFS and the outer SOL or first wall. It is also necessary to specify values for the anomalous cross field transport coefficients.

The SOLPS package primarily consists of the B2 multi-fluid code[77] and the EIRENE neutral particle Monte-Carlo code[90]. It has been used extensively on many tokamaks[91–94] and is one of the principle tools for SOL modelling. Stangeby [95] has used SOLPS to form a simple relationship between upstream electron density and temperature decay widths and the power width in the divertor, a vital parameter in the operation of ITER.

Studies carried out on ASDEX Upgrade[96] have also used SOLPS to understand the effect of cross-field drifts on plasma flow and target conditions in the SOL, showing good agreement between simulation and experiment in the low-recycling regime. SOLPS has also been used to study divertor detachment on ASDEX Upgrade and DIII-D[97], concluding that our current understanding does not allow effective simulations of detached conditions.

EDGE2D also comprises a multi-fluid plasma solver coupled to a Monte-Carlo neutral code, although there exists the choice of either EIRENE or an alternative neutral code NIMBUS[87]. This code has been primarily used on the JET tokamak although it has also been applied to ASDEX Upgrade[98] and used as a predictive tool for future devices [99, 100]. Its use on JET however has been extensive, studying the edge temperature and density profiles[101], SOL flows [43], migration of carbon-13[102], the effect of atomic processes on detachment [103] and in-out asymmetry[104]. Results from the code are also used in cross-code comparisons[105] that help improve the reliability of simulation results.

The majority of work using the UEDGE code has used data from the DIII-D tokamak. This has included scenario development[106], studies on visible carbon emission[107], the dependency of the behaviour of injected argon on the up-down magnetic balance in double null plasmas[108], studies of plasma wall interaction in the presence of ELMs[109], the effect of $E \times B$ drifts on the transport of intrinsic impurities[110] and the importance of edge transport on core carbon concentrations[111].

UEDGE has also been used in multi-machine studies, such as Groth[112] who showed the necessity of the inclusion of cross-field drifts to model divertor particle and heat loads on DIII-D ASDEX Upgrade and JET. In this work enhanced chemical sputtering yields were also required to closely repli-

cate observed conditions although these enhanced factors may conceal the fact that some other mechanism is inadequately modelled. The simulated flow was also shown to be incorrect on the machines studied, although this issue is also frequently the case for other edge codes. Detachment in the snowflake divertor on the spherical tokamak NSTX has also been studied using UEDGE[113] where a gas power loss mechanism was identified that may contribute to the high recycling seen in the snow-flake divertor simulation. This work also highlighted the need to improve the DEGAS neutral model used in the code. ITER simulations to study the effect of a 2^{nd} X-point have also been carried out[114].

1.4.5 The Onion Skin Method

Sitting between the 1 and 2 dimensional approaches described above is a modelling technique known as the the Onion-Skin Method, which relies on the assumption that the 1 dimensional conservation equations are valid over a finite radial extent. This method treats the boundary plasma as a sequence of nested flux tubes (fig. 1.2) and applies a suitable SOL model along $\mathbf{B}$ for each tube. This model can be anything from a simple two-point model to a comprehensive 1D model that solves the 1D conservation equations along $\mathbf{B}$ and includes volumetric sources and sinks for particle momentum and energy. Boundary conditions are set for each tube, usually at the targets from Langmuir probe data although upstream measurements from other diagnostics can also be used. This essentially results in a 2D solution derived from the 1D solutions for each flux tube.

Each flux tube is considered independently with no perpendicular transport between the tubes, this is a marked difference with a full 2-D code. In the 2-D approach the cross-field diffusivity must be set as an input param-

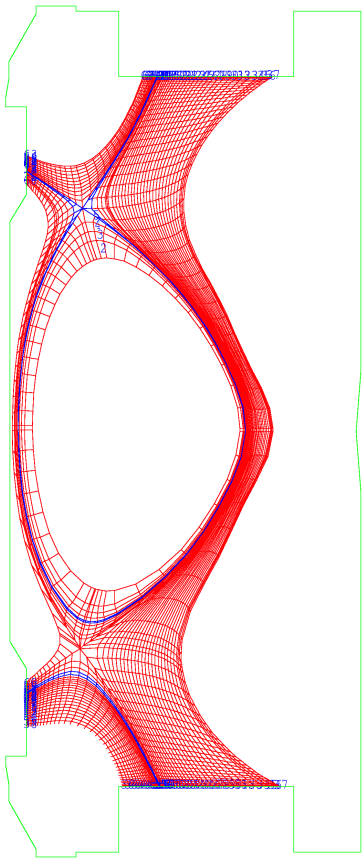

Figure 1.2: A typical onion skin geometry in the poloidal plane from a MAST plasma with the MAST first wall also plotted

eter, in OSM the cross-field fluxes can be extracted from the series of 1-D solutions using the radial variations of density and temperature across the target. An excess or deficit between the net particle source along a flux tube and the particle outflow to the target is attributed to the cross field transport of particles, which is treated as sources and sinks along the length of each tube[115]. The OSM 2-D plasma solution made up of the individual flux tubes can be used as a background for neutral or impurity codes that provide particle sources and sinks. The onion skin method can then be performed iteratively with these codes to obtain the best plasma solution incorporating

the effect of these sources and sinks. This approach provides a robust 2D simulation of the plasma and compares favourably with full 2D models such as EDGE2D[116].

A code based on the onion skin method and named OSM has been developed by Stangeby and Elder[84] and has been used on several machines. Neutral behaviour has been studied on Alcator C-Mod[117], cross field transport in the SOL on JET[118], the effect of including SOL currents in the model on MAST[119] and the midplane SOL conditions reconstructed on the EAST tokamak. When compared to the more complex 2D codes the OSM approach has the advantage of shorter run-times on the order of minutes compared to hours, days or longer for the 2D approach, meaning it can potentially be used for basic modelling during experiments. The extensive use of experimental data in constraining the solution also simplifies the simulation process, so that a reasonably reliable model of SOL conditions can be inferred quickly. OSM does not currently include drift terms, casting some doubt on the validity of the solutions[120], particularly in spherical tokamaks where these terms can be larger than in standard aspect ratio tokamaks.

1.4.6 Further SOL modelling

The development of ergodic divertors and a requirement for detailed modelling of plasma wall interactions for next generation devices such as ITER has called for the use of 3D fluid codes such as EMC3[121, 122] and BOUT++[123]. Full kinetic treatments of the SOL remain prohibitive, however more recently high performance computing environments have expanded the use of gyro-averaged kinetic treatments of the SOL plasma. Particle properties are averaged around a single gyro-orbit, removing the high frequency gyro-motion that makes full kinetic treatments intractable. This guiding centre approach

is used in massively parallel environments by several codes such as XGC[124], TEMPEST[125], GENE[126], GS2[127], GEM[128] and COGENT[129]. The coupling of these codes has also improved, with tools such as KEPLER[130] being used to allow many dedicated codes to be coupled relatively easily.

1.4.7 Kinetic impurity models

The 2D and OSM methods both provide a plasma background which can then be used as input to kinetic Monte-Carlo codes that follow impurity ions such as ERO[131], IMPMC[132] and DIVIMP[84]. These codes all follow impurity ions on the background plasma, including the transitions between ionisation states. They are commonly used to simulate impurity injection as the localised source means only a limited number of particles are required to gather adequate statistics, reducing the computational requirements that can become prohibitive when modelling a large domain in this manner.

ERO is often used with a background provided by SOLPS, and has been used in a large number of studies on ASDEX Upgrade. Aho-Mantila[133] showed that $\mathbf{E} \times \mathbf{B}$ drifts have a significant impact on the carbon migration in the ASDEX Upgrade divertor. Carbon re-deposition was also studied by Pugno[58] although these simulations did not include drift terms, which appear necessary to account for the deposition patterns deviating from the magnetic field direction. Makkonen[134] used ERO to study the flow of carbon by injecting methane at the midplane and suspected temperature gradient forces of driving flow towards the upper divertor in low density cases.

ERO has also been used on other machines such as JT-60U[135], where it was used to study asymmetry in divertor carbon deposition, TEXTOR[131], where material erosion was studied, and JET[136] to study material migra-

tion and erosion.

IMPMC is now included in the SONIC[137] package along with the two-dimensional fluid code SOLDOR and neutral code NEUT2D[138]. These codes have primarily been used on the JT-60U tokamak, Shimizu[139] and Hoshino[140] have studied impurity transport in detached plasmas, and is being used extensively in the design of the new JT-60SA tokamak[141–143]

The DIVIMP code has been used on a wide variety of machines with several plasma solvers being used to provide the background solution, although it is commonly bundled with OSM in a package called OEDGE. Lisgo[117] used this combination to study and improve the simulation of neutral behaviour in the C-mod divertor as well as studying detached plasmas in the DIII-D divertor. McLean and Mu[144, 145] have also used OEDGE on DIII-D to study CH_4 injection experiments. Tungsten transport has been studied on JET[146] using EDGE2D-EIRENE to provide the plasma solution, with this work leading to the conclusion that extrinsic impurity seeding is required to reduce the tungsten source and limit the core tungsten concentrations. SOLPS has been used to provide background solutions in simulations of carbon injection into ASDEX Upgrade plasmas[134, 147]. These simulations highlighted the importance of accurate modelling of the SOL flow, which is believed to be a cause of discrepancies between the simulated and measured carbon deposition. This combination has also been used to make predictions for tungsten erosion and transport in ITER[148], showing that in divertor plasma configurations running a tungsten divertor on ITER can maintain a core tungsten concentration below that required for successful operation.

Drift terms are not included in DIVIMP, when run with OSM providing the background plasma this means that significant physics is missing from the model. The use of DIVIMP for ITER predictions further increases the

importance of this omission. However the interpretive nature of OSM to some extent mitigates the lack of these terms, especially in light of the poor replication of plasma flow in current models.

1.5 The MAST tokamak

The Mega Amp Spherical Tokamak (MAST)[149] tokamak is a tight aspect ratio spherical tokamak with typical major radius $R = 0.85m$ and minor radius $r = 0.5m$. During normal operation the plasma has a maximum plasma current $I_p = 0.9MA$ and toroidal field $B_T = 0.52T$ measured at the magnetic axis. MAST typically operates in a double null divertor configuration. The open nature of the spherical tokamak design allows excellent diagnostic coverage of the plasma. As well as large arrays of divertor Langmuir probes MAST has several viewing ports at different toroidal locations around the machine, allowing comprehensive imaging of the plasma. A Thomson scattering system also provides measurements of both the core and edge plasma. MAST pulses are often referred to as shots and are numbered using a sequential numbering system, at the time of writing the latest shot number is 30473. These numbers will be used to refer to a particular discharge.

The lower divertor includes a system named the Divertor Science Facility (DSF)[150] for inserting samples and probes without any requirement to vent the machine. This system permits electrical connections and allows the installation of systems such as the impurity injector described here, a Retarding Field Energy Analyser (RFEA)[151] and a sample holder for the introduction of dust[150] in a single day during scheduled breaks in operation.

There are significant quantitative differences between spherical and the more common large aspect ratio tokamaks, however there is no fundamental

difference between the two designs. The achievable β (see section 1.2.1) is significantly higher in spherical tokamaks due to a reduction in both ballooning and kink instabilities. The increased curvature also means that the radial gradient of magnetic field is larger, resulting in stronger $\nabla \mathbf{B}$ drifts which can affect transport in the SOL. The plasma wetted area on the divertor surfaces is significantly smaller in a spherical tokamak due to the reduced major radius. This means that the heat flux to the targets is higher for a given total power, making the progression to reactor scale machines more difficult. Results from experiments on spherical tokamaks are generally comparable to those from large aspect ratio machines, and simulations can be carried out on both using the same software[152].

CHAPTER 2

Carbon injector design and testing

2.1 Design motivation

Impurities have a significant effect on plasma performance and can also be used to alleviate the problems of excessive heat loads on plasma facing components (see 1.2.1). An understanding of the transport of any impurities is therefore of great importance in the design and operation of existing and future tokamaks. The use of injected impurities in order to further this understanding is discussed in section 1.3.2. The most common methods of injection used in previous edge impurity transport experiments are laser ablation and the injection of impurity gases (section 1.3.2). For gas injection the number of particles injected is often significant when compared to the plasma density and the injected impurities significantly perturb the plasma. The injection also occurs over a timescale that is greater than the typical SOL

dwell time of the plasma so information on timescales shorter than this is restricted. Laser ablation offers the option of very short plume duration and accurate control of the number of ablated particles. However this method is technically very difficult to achieve and expensive. Another method that has been used previously on the START tokamak is that of ablation from arcs occurring between electrodes composed of the impurity to be injected, this work was unfortunately not published. Carbon is one of the more commonly studied impurities due to its presence in the majority of tokamaks and strong line emission and is also ideally suited for use as an electrode. Arcs can also occur on very short timescales $\approx 1\mu s$ and the equipment required to produce them is cheap and readily available. It was therefore decided that an injector using a short duration arc would be designed to ablate carbon into the SOL of the MAST tokamak. Data obtained from spectroscopic imaging and other diagnostics would then be used to model the observed impurity transport.

2.2 The injector design

2.2.1 The spark head

The geometry of the electrodes has a significant effect on the nature and result of an arc between them. The basic geometries one can envisage are planar, cylindrical, concentric and spark plug type electrodes. These possibilities can be seen in figure 2.1. Concentric electrodes were chosen for the prototype design as these have several advantages over the other geometries. A schematic of this design can be seen in figure 2.2. Concentric electrodes are simple to build and the inter-electrode gap remains stable under stress. They also take advantage of the Marshall effect, described below.

The Marshall Effect

A current discharge between concentric electrodes results in an axial force on the ions and electrons making up the discharge. This effect was first published by J Marshall in 1960 [153]. The magnetic field caused by the current flowing along the central electrode causes a $j \times \mathbf{B}$ force on the radial discharge current in the same direction as the positive current, accelerating the ions and electrons away from the electrode for both possible polarities. A reasonable approximation for the impulse delivered to the plasma is given by [153]

$$\int_t f dt = ln(r_1/r_2) \int_t I^2 dt \tag{2.1}$$

where r_1 and r_2 are the outer radius of the inner electrode and inner radius of the outer electrode respectively and I is the discharge current.

It should be noted that at the currents generated in the injector head the typical magnetic field created is many times smaller than the typical field of several Teslas found in tokamaks. Due to this the effect is expected to be weak during operation within MAST but may be augmented at points around the electrodes that are suitably aligned with the toroidal field.

2.3 Injector development

2.3.1 Test conditions

A dedicated vacuum chamber was built for the development and testing of the injector. The chamber was largely constructed from components already owned by the National Centre for Plasma Science and Technology. It uses a TPH 240 ISO 100 Pfeiffer turbo pump and has a base pressure of $5 \times 10^{-5} Pa$,

significantly lower than the MAST divertor pressure ($\sim 10^{-3}Pa$). Initial testing was carried out using a capacitor bank of up to 20nF charged using an Ultravolt 15A12P4-C power supply capable of delivering 15kV at 0.4mA. The final design for use on MAST ran significantly lower voltages up to 2.5kV, this limit was largely due to safety considerations imposed by the MAST team. In order to accomplish breakdown at voltages below this limit a significantly higher capacitance of $1.5\mu F$ was used in the final system. Triggering was initially performed using a mechanical switch made in the laboratory, this was later replaced with an Insulated Gate Bipolar Transistor(IGBT), see section 2.4.2.

The outer electrode was made up of a carbon cylinder manufactured by the MAST Special Techniques group. Cylinders of outer diameter 8mm and inner diameter 3.1mm and 4.1mm allowed for testing of variable gaps between the inner and outer electrode. The inner electrode consisted of carbon rods that were available at DCU. For testing the concentric electrodes were fitted into an SHV clamp connector, allowing easy interchange of the injector head, see figure 2.3. An aluminium oxide sleeve was used as the insulator between the two electrodes. This sleeve allowed the end of the electrodes to protrude by 1-5mm, providing the spark gap itself.

2.3.2 Observed pressure increase

Large pressure increases in the vacuum chamber were observed after the test discharges, figure 2.4. Although variable, this pressure increase was dependent on the chamber pressure and both the capacitance and voltage used. The increase was measured using a Tektronix TD3000 oscilloscope connected to a Pfeiffer ion-combi gauge. The initial rise occurred over a timescale of 100ms immediately after each discharge, this leads to the conclusion that

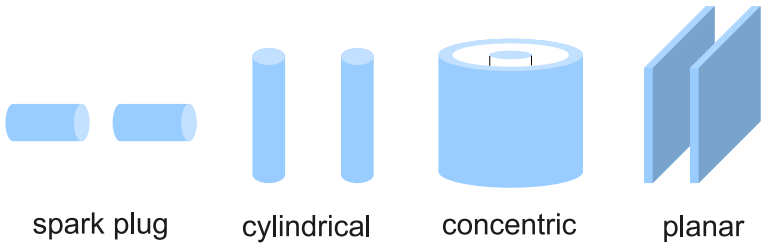

Figure 2.1: Possible electrode geometries

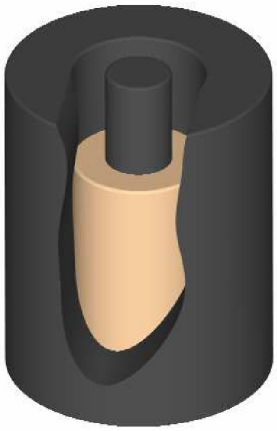

Figure 2.2: Conceptual design for the carbon injector

Figure 2.3: The carbon electrodes of the injector head fitted to an SHV clamp connector

the increase was due to material ablated from the injector. However, ablated carbon is likely to stick to any surface it encounters so is unlikely to have diffused to the pressure gauge mounted at the end of a short KF25 elbow tube mounted above the chamber. The pressure increase was then suspected to be due to hydrogen and oxygen from the dissociation of water present on the injector head. This was then confirmed by using a mass spectrometer attached to the vacuum vessel, a significant increase in both hydrogen and oxygen was observed after each discharge, although a small increase in the carbon content was also observed. This is also consistent with the dependence on voltage and capacitance, the higher the energy released during discharge the more water is dissociated.

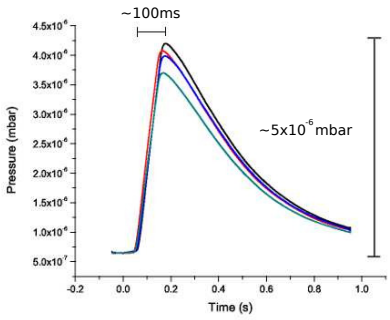

Figure 2.4: Pressure increase observed after a 10kV 20nF discharge

This presented a significant issue regarding the sparker operation on MAST where there is essentially zero water content. If it is the water initiating the breakdown then the system would not work on MAST or any other tokamak. In order to test this efforts were made to reduce the water content in the chamber, which was measured using a Pfeiffer QMS200 mass spectrometer. While at atmosphere the vessel was baked to remove water from the walls, the vessel was purged with a flow of nitrogen and then pumped down, finally the vessel was cooled to cause the water vapour to condense

on the chamber walls. This only partially succeeded in reducing the water content although the chamber pressure was reduced to $3 \times 10^{-5} Pa$. At this pressure the mono layer formation time is approximately 4s, using the relation $\tau_{mlf} \approx 4/P$[154], this allows the possibility of testing the discharge in the absence of water by repeatedly firing the injector at a frequency greater than $1Hz$, effectively cleaning the injector head and not allowing for the formation of a water layer before each discharge. The injector continued to break down in these conditions verifying that breakdown was possible in the absence of a water layer. The associated pressure increase also decreased after the initial discharges, showing that water dissociation associated with the discharge was significantly decreased and attributable to water existing as vapour close to the injector head.

2.3.3 Ablated mass measurements

The most important parameter of most injection systems is the quantity of material injected. This can be measured using quartz crystal monitors placed in front of the injector (figure 2.5, carbon ablated from the injector then adheres to the face of the quartz crystal, changing its resonant frequency. The frequency shift for a rigid mass evenly deposited onto the crystal is given by the Sauerbrey equation[155]

$$\Delta f \approx \frac{-2\Delta m f_0}{A\sqrt{\rho_q \mu_q}} \tag{2.2}$$

for $\Delta f / f_0 < 2\%$. Where f_0 is the resonant frequency, Δf is the change in frequency, Δm is the change in mass, A is the piezo-electric active area, ρ_q is the density of quartz ($2.648 \times 10^3 kgm^{-3}$) and μ_q is the shear modulus of the crystal ($2.947 \times 10^{10} kgm^{-1}s^{-2}$). The crystals were mounted in a specially made probe that can be seen in figure 2.5.

An intellimetrics IL150 Quartz Crystal Growth Rate Monitor was used to drive the crystal and the thickness measurements were then converted into masses. There are large uncertainties in the plume size and quantity of carbon sticking to the crystal surface, however a lower limit can be placed on the mass of carbon ablated by each discharge. The dependency of ablated mass on the discharge voltage and stored charge can also be investigated.

The IL150 provides a measure of deposited thickness in nanometres, in order to translate this measure into a mass it was assumed that the ablated carbon formed a uniform coating on the monitor. Although this is clearly not the case the uncertainties already present in the measurement make this a reasonable assumption. The portion of the crystal exposed to the plume is circular with diameter 8mm, making a total area of approximately $50mm^2$. The IL150 takes as input the density of the deposited material and this was set at the density of amorphous carbon $2g.cm^{-3}$ in the units used by the IL150. This gives an ablated mass of $\approx 10^{-7}g/nm$, equivalent to 6×10^{15} atoms/nm.

Using the lossy mechanical switch deposition experiments were carried out using 3-5kV and a capacitance of 200nF, equating to a stored energy of up to 2.5J. No magnetic fields were applied to the plasma. Due to the low sensitivity of the monitor crystal 5 shots were performed before each measurement. A series of shots were also performed immediately before the measurements in order to remove any water layer that may have formed on the injector head. At 3kV no breakdown occurred however breakdown did occur at 3.5kV. At 4kV the average deposition for each pulse was 0.04nm while at 5kV the average deposition was 0.06nm. This equates to 2.4×10^{14} particles at 4kV and 3.6×10^{24} particles at 5kV.

2.3.4 Imaging

High speed imaging of the plume was also carried out in order to confirm the plume duration and extent. An Andor DH5H7 18F 03 single shot visible camera was used to image the plume at different times during the discharge. The camera was triggered using a Stanford DG535 pulse delay generator connected to a C-T current monitor located between the capacitor bank and the spark head. The delay was varied from 0ns to 3000ns and the integration time from 5ns to 60ns. A capacitor bank of 20nF was used at a voltage of 8kV giving a stored energy of 0.64J. The extent of the plume is very limited, up to 5mm, however it is expected that the extent will increase as the capacitance used is increased towards $1\mu F$. Looking at figure 2.6, the duration of the plume can be seen to be less than 3ms, figure 2.6 shows the last remnants of the plume. This duration matches the duration of the current pulse measured using a Bergoz C-T current monitor, see figure 2.7.

Scanning electron microscopy and energy dispersive X-ray spectroscopy

A significant concern raised by the MAST team was that of contamination of the vessel by the injector. In order to verify the purity of the ablated material the crystal used for ablated mass measurements was subjected to Energy Dispersive X-Ray spectroscopy (EDX) once a significant carbon layer had been built up. Spectrograms taken with beam energies of 10 and 20kV can be seen in figure 2.8. The depth of penetration of the beam is dependant on the energy of the beam, the gold line seen in figure 2.8 b is due to the beam penetrating through the thin layer of deposited carbon and interacting with the gold substrate of the crystal. The 10kV spectrogram can therefore be taken to be that of the carbon layer on the crystal. The only significant

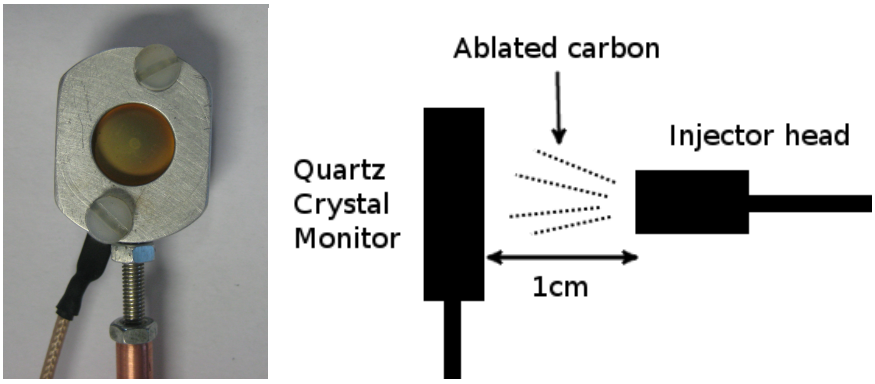

(a) (b)

Figure 2.5: a) Probe containing a quartz crystal, the discolouring evident on the crystal surface is due to ablated carbon. b) Side on schematic of the quartz crystal placed in front of the injector head for ablation measurements.

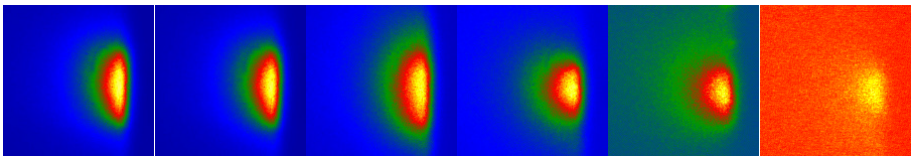

(a) (b) (c) (d) (e) (f)

Figure 2.6: Visible images at 0, 50, 500, 1000, 2000 and 3000 nanoseconds after the beginning of the discharge. Figures a to d were taken with a 40ns integration time and figures e and f with a 20ns integration time. Each image is 10mm by 10mm in the plane of the injector head which is on the right hand side of each image.

non-carbon element detected is fluorine and this is likely to be due to contamination from the atmosphere or contact with skin. It should be noted that EDX spectroscopy is particularly insensitive to carbon, strengthening the conclusion that the material ejected from the injector is largely pure and not contaminated by the ceramic used in the injector head or any other source.

The EDX technique is performed in a Scanning Electron Microscope (SEM), as part of the process high resolution images were taken of the crystal surface. This provides useful information on the size of the particles that are ablated from the injector, ideally the carbon would be produced in purely ionised form, however in reality this is not the case and significant quantities of neutral carbon are produced along with larger carbon fragments. Figure 2.9 shows one image of the surface and covers an area of approximately $23mm \times 18mm$. One large particle of carbon measuring about $100\mu m$ can be seen in the lower half of the image. Particles of this size are likely to perturb the plasma so that it may be necessary to include a fine mesh in front of the injector to catch large particles such as these. Other than this and a few other smaller particles the carbon deposition appears uniform, implying that a significant quantity of the ablated material consists of particles on the sub-micron scale and carbon ions.

2.4 Final design

2.4.1 The injector head

The spark head used for laboratory testing used small quantities of adhesive to hold the carbon electrodes in place. This is not suitable for use in a tokamak environment so the final design required that the components in

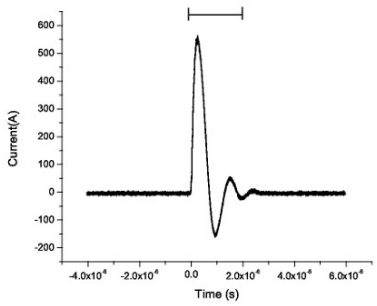

Figure 2.7: The current pulse for an 8KV 20nF discharge. The classic ringing of a capacitor discharge can be seen as the current drops below zero and recovers.

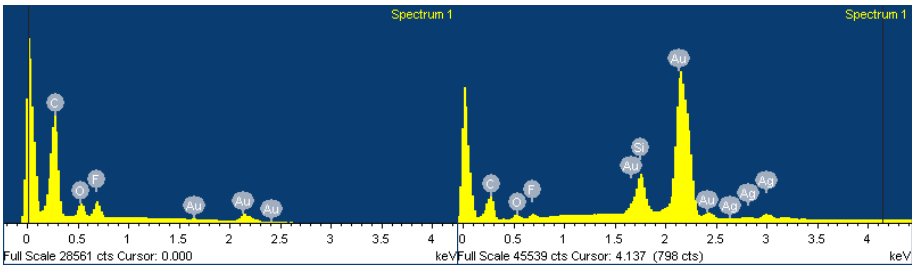

(a) (b)

Figure 2.8: EDX spectrograms for beam energies of 10kV and 20kV showing no significant contamination other than a small quantity of fluorine that is likely due to external contamination

the spark head be held together mechanically. Aluminium oxide is also not suitable for use in a tokamak so boron nitride was used as the insulator. The electrodes and insulator were held in place by incorporating a series of steps in their design, a pair of springs then holds the components in place, see figures 2.10 and 2.11. Before installation on MAST the injector head was cleaned and baked in vacuum for 24 hours to remove any contamination caused during assembly. An image of the assembled head can be seen in figure 2.13

A Langmuir probe was included in the head design and can be seen in the top right corner of figure 2.10 and in closeup in figure 2.14. This probe provides a Temperature/Density measurement close to the point of injection. It also provides a good indication of the passing time of the strike point over the DSF as the ion saturation current peaks as the strike point crosses the Langmuir probe. The signal from the LP is recorded at 1MHz by the existing Langmuir probe system on MAST.

The cables used to carry the electrical pulse were 311-KAP50 coaxial cable supplied by Allectra. Coaxial cable was chosen as it was believed the outer conductor would shield the vessel from electrical noise. The inner conductor of this cable is just 0.45mm, although this is sufficient for transmitting the electrical pulse it proved very fragile and made construction of the probe head difficult. The cable is soldered to the copper contacts using flux-less solder and this connection often broke when the head was being assembled. It is likely that for future designs a larger, possibly non-coax wire will be used.

Full manufacturing drawings of the injector head mounted on the DSF can be seen in appendix A.

2.4.2 Power supplies and triggering

The electrical pulse that creates the spark is delivered by a bank of capacitors located under the MAST vessel in a box installed for DSF specific equipment. All the circuitry to charge and trigger the capacitor bank is contained in a polycarbonate box that will be referred to as the Injector Power Supply or IPS. This box is temporarily mounted in the permanent DSF box. Power and signal cables installed in the DSF box are connected to the IPS. The layout and operation of this box can be seen in drawings M115-02-101 and M115-02-102 located in Appendix B.

The capacitor bank itself consists of 10 $0.15\mu F$ polypropylene capacitors mounted in parallel. The box electronics are powered by a Calex 24V DC power supply. A Spellman MPS2.5kV10W24V HV power supply was used for capacitor charging, this unit has a peak voltage of 2.5kV and a maximum current of 4mA. An optical trigger signal is received from the MAST data acquisition system and converted to a 5V electrical signal that is used to drive an IXYS IGBT which triggers the capacitor discharge across the injector electrodes. The IGBT (Insulated Gate Bipolar Transistor) is a power semiconductor device that combines an isolated gate FET and a bipolar power transistor to achieve fast switching at high voltages and currents. As the peak voltage used in the final design is 2.5kV a single IXGL75N250 2.5kV IGBT was sufficient while during testing several of these were used in parallel to switch voltages up to 5kV. The triggering circuit can be seen in appendix B.

The HV power supply is regulated by a 0-5V signal from the MAST control system and returns the actual operating voltage via a 0-5V output signal. Both these signals use isolation amplifiers to protect the MAST diagnostic systems. A Bergoz CT-B0.05 current transformer is situated on the capacitor

bank output and provides a measure of the discharge current that is passed to the MAST data acquisition system.

An optical enable signal is required for the HV supply to operate to avoid the capacitors becoming accidentally charged when not mounted in the DSF box. There is also an interlock on the IPS lid comprising of a normally closed high voltage relay that is only opened when the 24V supply is on and the lid is closed. If the 24V supply fails or the lid is opened the capacitors are then discharged through a 300Ω resistor in a fraction of a second.

2.4.3 Modification after initial commissioning

During the first set of commissioning experiments in MAST campaign 8, October 2011 the IGBT switch failed and was replaced so as to allow further experiments. Although the cause of this was not known it is believed that it was caused by a reverse voltage applied to the IGBT, possibly as the strike point crossed the injector head in a beam heated discharge. The power supplies were not disconnected from the injector head between experimental sessions due to the difficult access during operations. To mitigate this risk a transient suppression diode was added in parallel to the spark gap for the second set of experiments in MAST campaign 9, June 2013.

2.5 Installation on MAST

The spark head was mounted in the head of the Divertor Science Facility (DSF)[150], see figure 2.15. This system was developed on MAST to allow samples and diagnostics easy access to the MAST divertor plasma in a similar way to the DiMES system on DIII-D[156]. The DSF allows probes to be installed in the MAST divertor without venting the machine and is placed at a

radial location of 0.98m. Before installing the head it was cleaned and baked for 24 hours to remove any contaminants from the manufacturing and assembly. The head was then installed on the DSF in a vacuum chamber isolated from the MAST vessel by a gate valve. This process was completed in under 2 hours. Once this was done the vacuum chamber was pumped down using an external rotary pump and a turbo-molecular pump to bring the pressure to that inside the MAST vessel. Heating straps were then placed around the chamber which was baked for several days to remove any contaminants introduced in the installation process. The gate valve to the MAST vessel was then opened and a pneumatic pump used to lift the DSF and injector head into position in the MAST divertor. Figures 2.16 and 2.17 show the injector head in its final location in the MAST divertor.

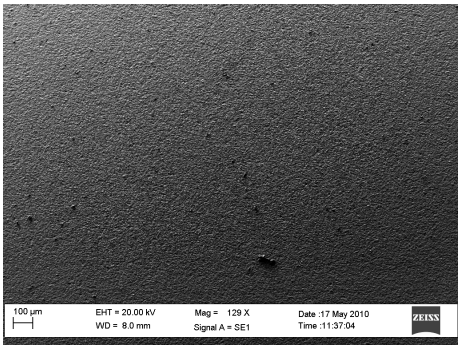

Figure 2.9: SEM image of carbon deposited on the surface of a quartz crystal microbalance. Carbon particles up to $100\mu m$ can be seen, the overall width of the image is approximately 20mm.

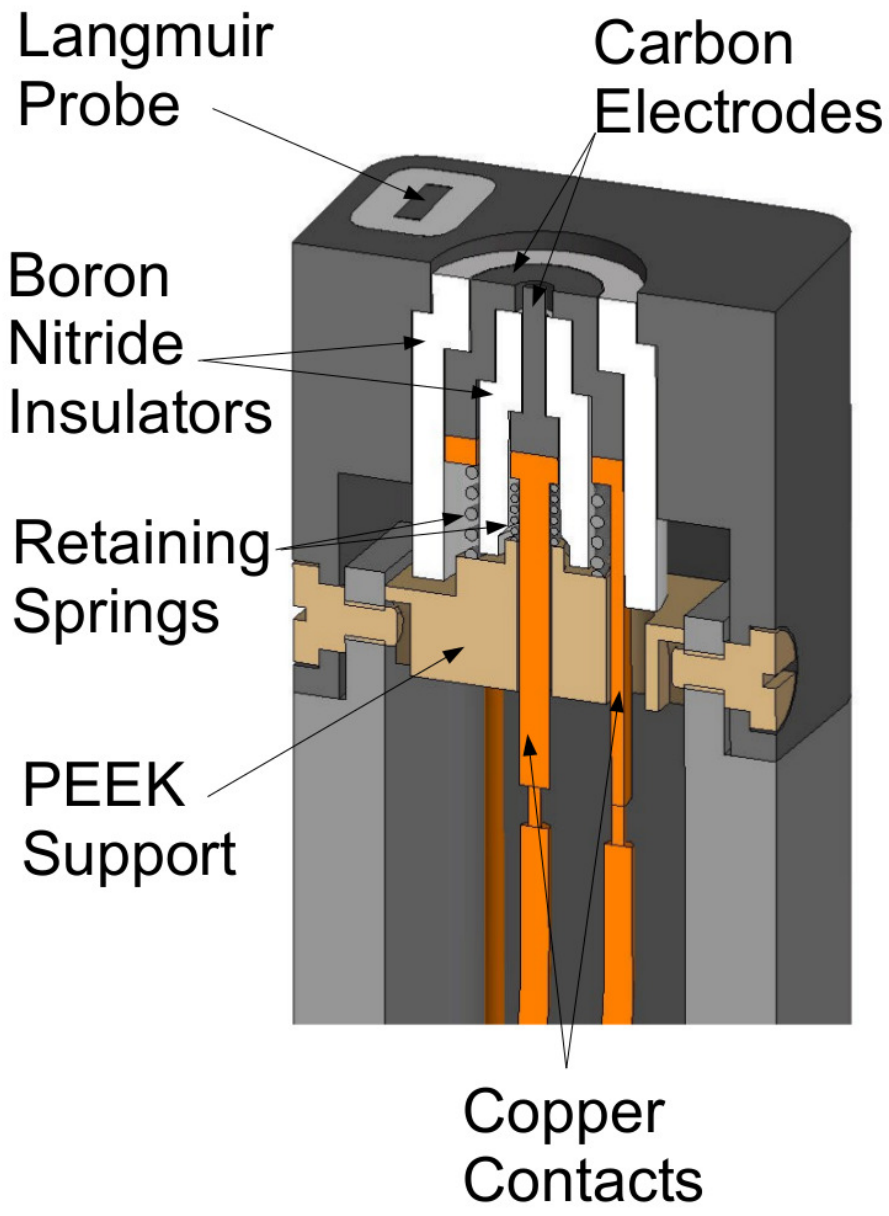

Figure 2.10: Close up of the injector head on top of the DSF probe. The carbon electrodes, boron nitride insulators, copper contacts and the PEEK support can all be seen as well as the integrated Langmuir probe.

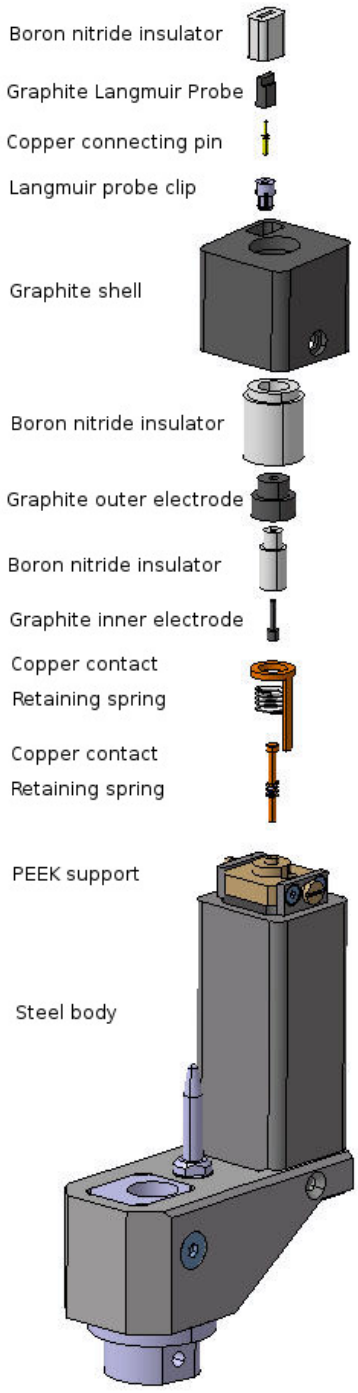

Figure 2.11: Exploded view of the injector head on top of the DSF probe showing the stepped construction allowing the components to be held in place without the use of adhesives.

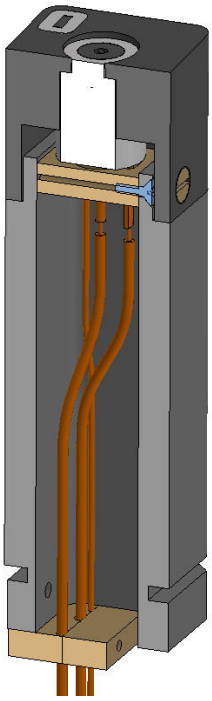

Figure 2.12: Cutaway view of the assembled injector head.

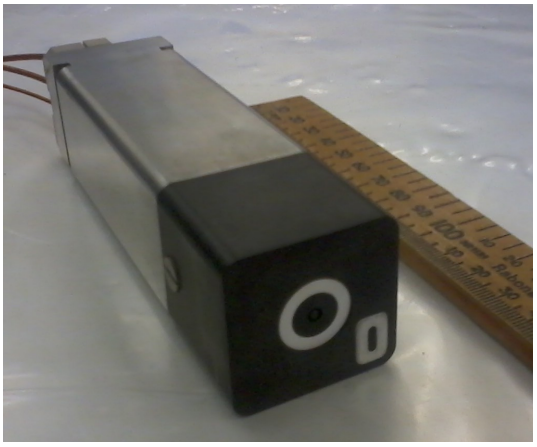

Figure 2.13: Image of the injector head prior to installation on MAST.

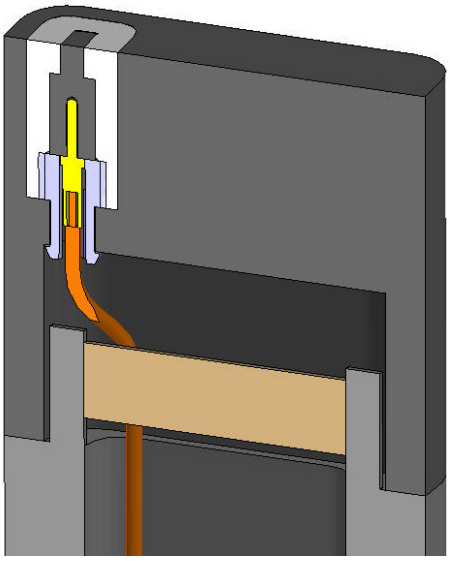

Figure 2.14: Cutaway view of the assembled injector head showing the integrated Langmuir probe.

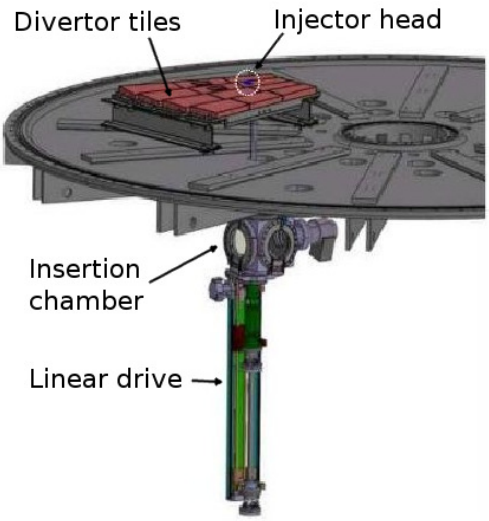

Figure 2.15: Schematic overview drawing of the DSF showing the insertion system and the independent pumping system. The drawing shows the DSF configuration when the head is fully inserted into the machine

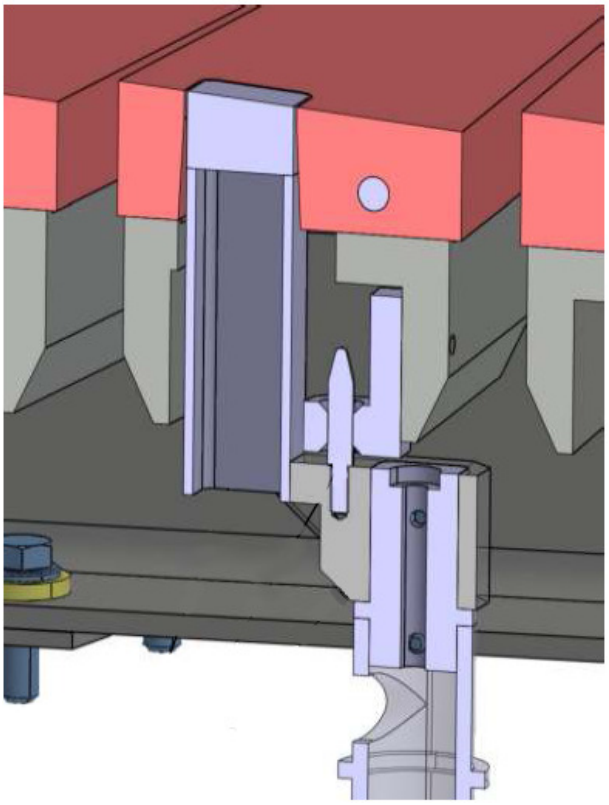

Figure 2.16: Cutaway of dummy injector head in place in the MAST divertor.

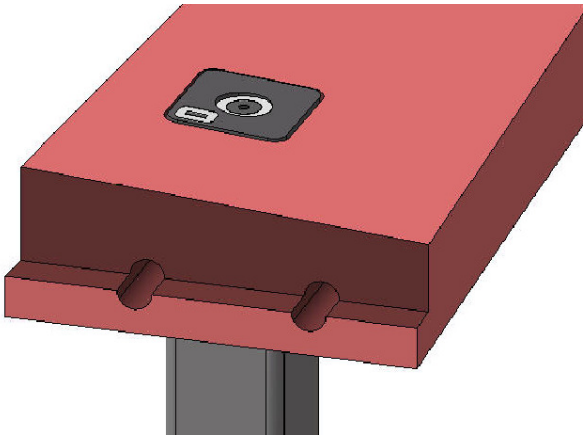

Figure 2.17: Schematic of the the installed injector head seen from above.

CHAPTER 3

Experimental method and data

3.1 Experimental approach

3.1.1 First use

Commissioning of the injector was carried out on MAST during September 2011. Images of impurity injection were subsequently taken in two sets of experiments, once in October 2011 during campaign 8 and then again in June 2013 during campaign 9. The data used for comparison with simulation was from the second set of experiments, however a brief description of the commissioning process and initial experiments and is included in appendix C.

3.1.2 Diagnostics

In order to make useful comparisons of impurity transport between modelling and experiment it is important to accurately characterise the background plasma. This is particularly true when using the Onion Skin Method (see 1.4.5). Langmuir probes positioned in the MAST divertor[157] and a mid-plane Thomson scattering system[158, 159] provide electron density and temperature data that forms the basis for the OSM reconstruction of the background plasma. These diagnostics are available routinely on MAST.

The goal of the experiments was to image injected carbon at different points relative to the outer strike point from a few centimetres into the private flux region to a few centimetres into the outer SOL. This is achieved by varying the timing of the injection as the strike points sweep across the targets. An initial guess of the location of the strike point relative to the DSF at a given time was made using EFIT [160] equilibrium construction. This was then compared with data from the Langmuir probe mounted on the injector head and with data from the divertor Langmuir probes. There are often discrepancies between the values obtained from EFIT and those from the Langmuir probes, this will be discussed on a shot by shot basis where appropriate.

The primary diagnostic requirement for this experiment is for the fast visible cameras positioned in sectors 1 and 11 of the MAST vessel, see figures 3.1 and 3.2. Photron Ultima APX-RS cameras were used at both locations. A significant part of the experimental process was concerned with obtaining the highest temporal resolution possible. Taking the plasma sound speed (equation 1.1) as an estimate for the ion velocity using typical near target temperatures of $T_i = T_e = 25ev$ gives $c_s \approx 5x10^4 ms^{-1}$. An ion moving at this speed would take $50\mu s$ to travel 10cm, frame rates better than this are

therefore required to resolve the formation and transport of the plume. In order to achieve a strong signal the standard 50mm lenses on the fast cameras was replaced by a $25mm$ lens that reduced both the field of view and the spatial resolution by a factor of 2 but allowed shorter integration times so that the cameras could be run at $75kHz$-$100kHz$, giving a time between frames of $10 - 13\mu s$.

Band-pass filters were used to select the carbon II and carbon III lines emitted by the ablated carbon as it is ionised within the SOL. The carbon II filter on sector 1 had a bandwidth of $2.76nm$ centred around $514.91nm$ and the carbon II filter on sector 11 had a bandwidth of $2.75nm$ centred on $514.79nm$, although the primary emission of the carbon II multiplet is centred at $514nm$ this wavelength is within the range of both filters. The carbon III filter had a bandwidth of $1.42nm$ centred around $465.29nm$, encompassing the carbon III multiplet also centred around 465nm. Filters for the D_α line at 656.1nm and CI line at 910nm were also fitted to the cameras on a remotely changeable carousel. In order to achieve a strong signal the standard 50mm lenses on the fast cameras was replaced by a $25mm$ lens that reduced both the field of view and the spatial resolution by a factor 2 but allowed shorter integration times so that the cameras could be run at $75kHz$-$100kHz$, giving a time between frames of $10 - 13\mu s$.

Having access to two cameras at different positions allowed the choice of either running the same filters on both cameras or to run two different filters. Using the same filters provides tighter constraints on the plume dynamics for a single charge state. This was restricted to the carbon II line as carbon III filters were not available for both cameras. In addition the carbon II emission was generally too weak to show the plume evolution. Using two different filters has the obvious advantage of showing the evolution of the ionisation

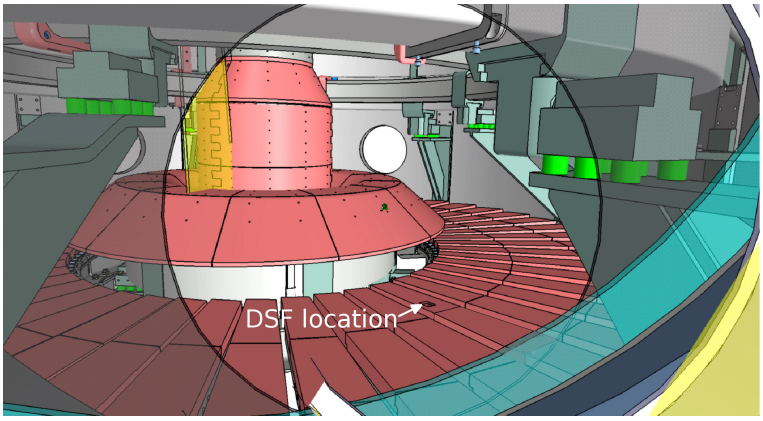

Figure 3.1: View of the DSF from the fast camera situated at a view port in sector 1 of MAST

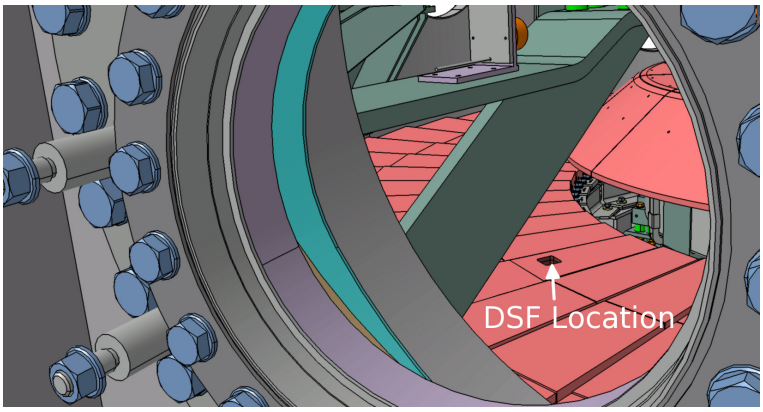

Figure 3.2: View of the DSF from the fast camera situated at a view port in sector 11 of MAST

states of the injected carbon providing additional modelling constraints.

Flow data was also available for some of the experimental sessions, this was provided by a coherence imaging diagnostic (see 1.3.1) using the carbon III emission line[1]. The MAST instrument operates with each pixel corresponding to $1.5mm$ in the plasma cross-section with a vertical resolution of approximately 12 pixels. This diagnostic produces a 2D map of line averaged flow with a temporal resolution of 1ms and a flow resolution of approximately $1km/s$.

3.2 Experimental data

Although useful data was obtained during the first experimental sessions detailed analysis and simulation was not performed before the opportunity of a further set of experiments in June 2013. As MAST was due to begin a shutdown for the upgrade to the super-X divertor this would be the last possibility for experiment over the timescale of this project. No external heating was used in the initial experiments due to the risk of damage to the injector system. The temperature and density of the plasma was therefore relatively low and the relevance to future devices limited. The data shown here was taken during an experimental session using beam heated plasmas on Thursday 20^{th} June 2013.

3.2.1 Plasma configuration

Two plasma configurations were used in the final experimental session. A single beam heated L-mode plasma based on reference 28787 and a 2 beam heated ELM-free H-mode plasma based on reference 28982. An ELM-free H-mode was chosen so as to avoid the complexities in both measurement and

simulation introduced by the ELMS. The strike point in the reference H-mode shot did not cross the injection location, the P2 and solenoid coil current were increased to move the strike point and allow injection into the outer SOL although not at the strike point itself. At the injection times the L-mode plasmas parameters were $I_p \approx 900MA$, $B_T \approx 0.55T$, $n_e \approx 13 \times 10^{19}m^{-2}$ and $P_{NBI} = 1.8MW$ where P_{NBI} is the total power from Neutral Beam Injection (NBI). The H-mode parameters were $I_p \approx 900MA$, $B_T \approx 0.55T$, $n_e \approx 25 \times 10^{19}m^{-2}$ and $P_{NBI} = 3.5MW$. In total data was taken for 6 shots, table 3.1 shows the injection timing, strike point position given by EFIT, the distance between the injection location and the strike point and the camera filters used for each shot. For the L-mode shots a charging voltage of $1.5kV$ was used, equating to a stored energy of $1.7J$, for the H-mode shots only limited emission was seen at this voltage so it was increased to $2.4kV$, equating to a stored energy of $4.3J$.

Shot	t_{spark} (ms)	Strike point position (m)	ΔR (cm)	Sector 1 filter	Sector 11 filter
29125 - L-mode	250	0.981	0.4	Carbon II	Carbon II
29126 - L-mode	250	0.976	0.9	Carbon II	Carbon II
29128 - L-mode	240	0.971	1.4	Carbon I	Carbon III
29129 - L-mode	240	0.973	1.2	Carbon I	Carbon III
29139 - H-mode	320	0.985	0.0	Carbon II	Carbon II
29142 - H-mode	320	0.989	-0.4	Carbon I	Carbon III

Table 3.1: Shots from the final experimental session

For reference time traces for D_α emission, plasma current, neutral beam total injected power, line integrated density and toroidal magnetic field on the magnetic axis for the L-mode and H-mode shots can be seen in figures 3.3

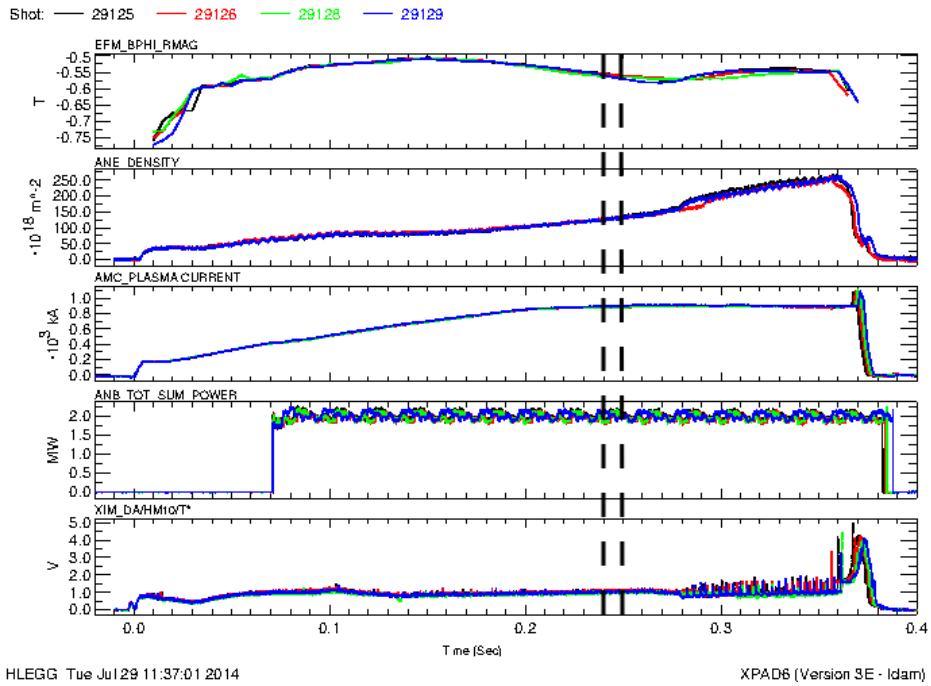

Figure 3.3: D_α emission, plasma current, neutral beam total injected power, line integrated density and toroidal magnetic field on the magnetic axis for the L-mode shots 29125, 29126, 29128 and 29129. The impurity injection times are denoted by dashed vertical black lines.

and 3.4. The line integrated density data was not available for shot 29139.

3.2.2 Injection duration

It can reasonably be assumed that ion and neutral injection occurs predominantly while current is flowing across the spark gap from the capacitor bank. The measured current leaving the capacitor bank for the 6 shots of interest can be seen in figure 3.5. The current can be seen to oscillate or 'ring' as is expected from a capacitor discharge. The width of the initial positive current surge is approximately $10\mu s$ while the ringing continues for $40\mu s$ for the L-mode shots and $60\mu s$ for the H-mode shot, which used a higher charg-

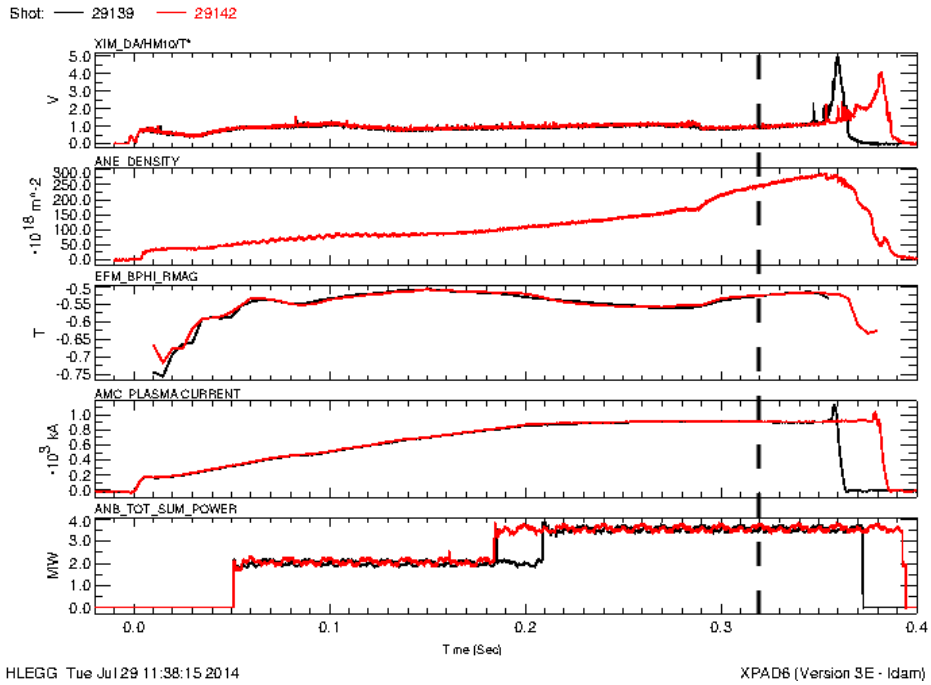

Figure 3.4: D_α emission, plasma current, neutral beam total injected power, line integrated density and toroidal magnetic field on the magnetic axis for the H-mode shots 29139 and 29142. The impurity injection time is denoted by a dashed vertical black line.

ing voltage (see 3.2.1). An estimate for the injection duration can also be obtained from the CCD imaging, figure 3.6 shows the time evolution of the emission observed by the CCD at the point of injection. Although there is a large degree of uncertainty in this method the duration of the high emission peaks support the view that the injection occurs over the duration of the ringing cycle and not just during the initial current surge or significantly after the discharge has ended. A further inaccuracy arises due to the capacitance of the transmission line from the power supplies to the injector head. Charge may build up in the coaxial cables which can then discharge across the spark gap at a later time.

3.2.3 Injection location

Identifying the injection location relative to the strikepoint is very important when comparing experiments with simulation. For the L-mode shot injection was performed at 2 locations, due to the limited experimental time available only 1 injection location was performed for the H-mode shot. Analysis is presented for the three locations. Figures 3.7, 3.8 and 3.9 each show the strike point location calculated from EFIT, data from the divertor Langmuir probes and data from the injector Langmuir probe for the three injection locations.

Plasma perturbation

The on-board Langmuir probe provides a means of estimating the perturbation to the plasma at the targets caused by the injection. The LP ran at a frame rate of $6.5 \times 10^{-5}s$, approximately $15kHz$ longer than the spark duration however any significant effect would likely be visible in the data. Figure 3.10 shows the measured saturation current against time for the 6 shots of

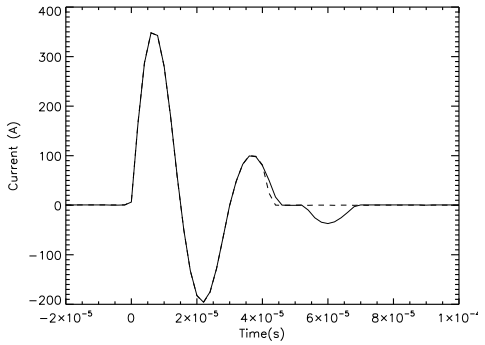

(a) 29125 & 29129

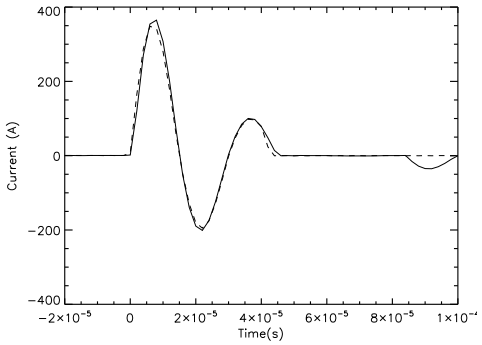

(b) 29126 & 29128

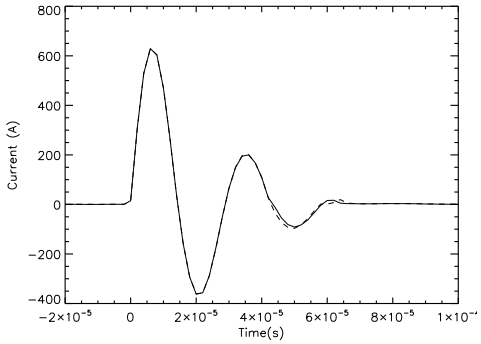

(c) 29139 & 29142

Figure 3.5: Injector discharge current measure by the integrated current transformer. The solid lines show the current from the first shot in each plot while the dashed line the second.

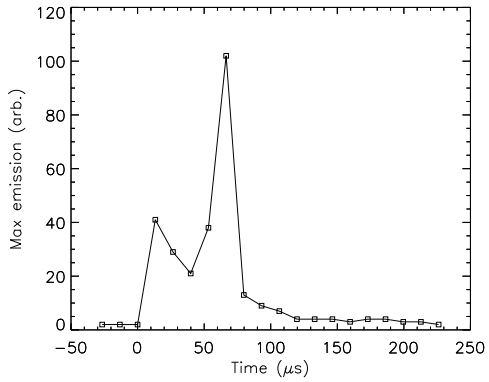

(a) 29125

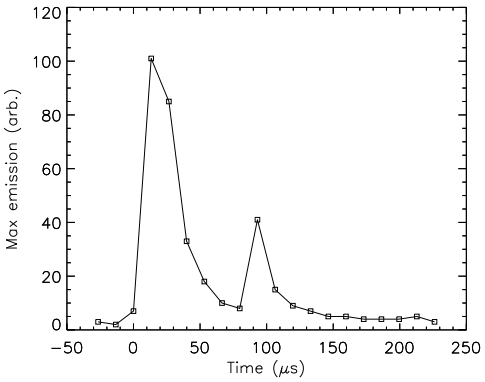

(b) 29126

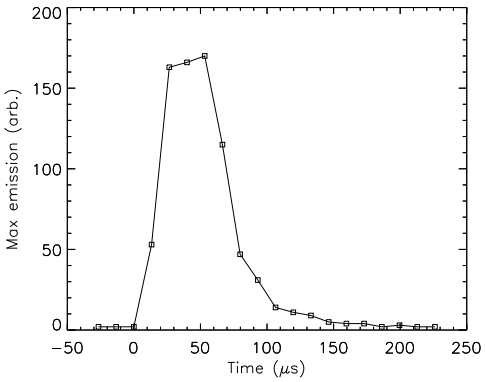

(c) 29139

Figure 3.6: Maximum carbon II emission observed within 5 pixels of the injection location for the three shots 29125, 29126 and 29139. This provides an estimate of the duration of carbon injection of approximately $40\mu s$ for the L-mode cases and $60\mu s$ for the H-mode case.

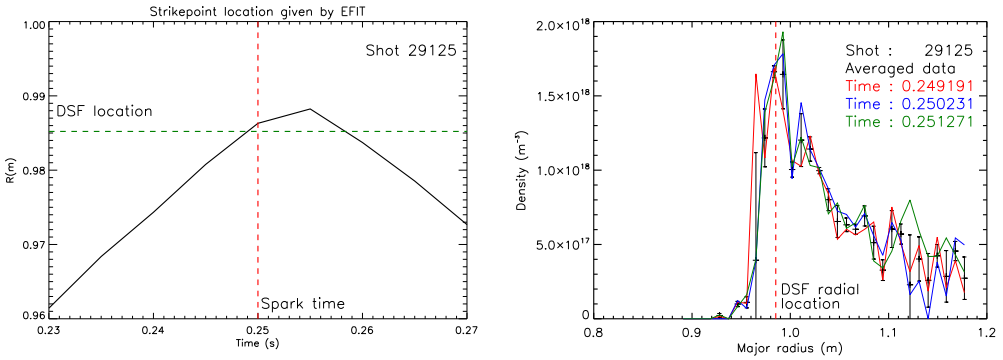

(a) EFIT

(b) Divertor LPs

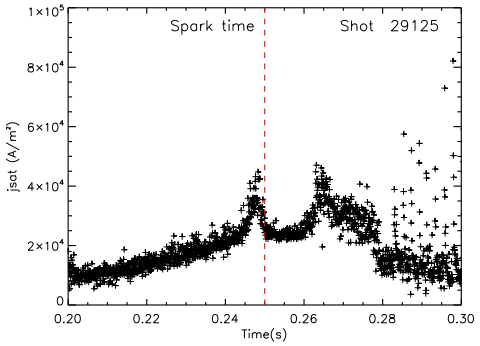

(c) Injector LP

Figure 3.7: EFIT and LP data from shot 29125 showing the strike point position at the injection time of 250ms. a) Strike point location plotted against time shows the strike point moving outwards until it crosses the injector head then moves inwards again. b) Radial density profile from the divertor Langmuir probes, the strike point lies close to the peak of this profile. c) Saturation current from the on-board Langmuir probe plotted against time showing an increase just before the injections time as the strike point crosses the injector.

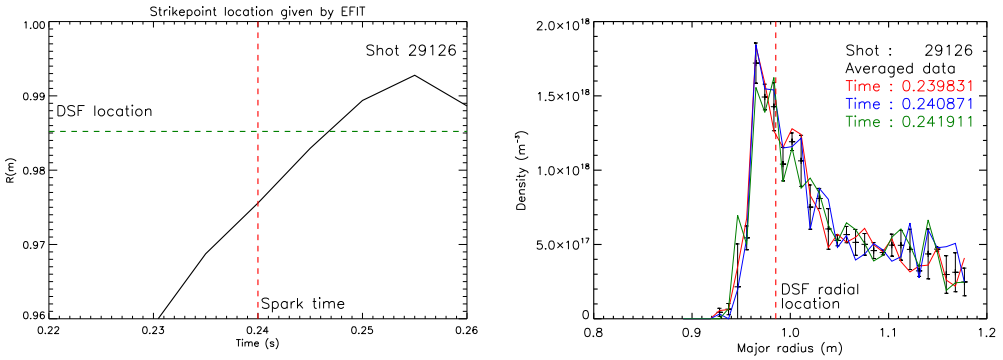

(a) EFIT

(b) Divertor LPs

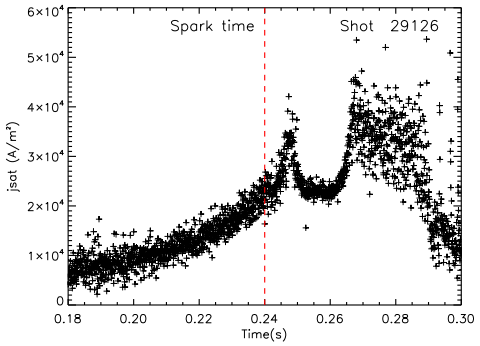

(c) Injector LP

Figure 3.8: EFIT and LP data from shot 29126 showing the strike point position at the injection time of 240ms. a) Strike point location plotted against time shows the strike point moving outwards until it crosses the injector head then moves inwards again. b) Radial density profile from the divertor Langmuir probes, the strike point lies close to the peak of this profile. c) Saturation current from the on-board Langmuir probe plotted against time showing an increase just before the injections time as the strike point crosses the injector.

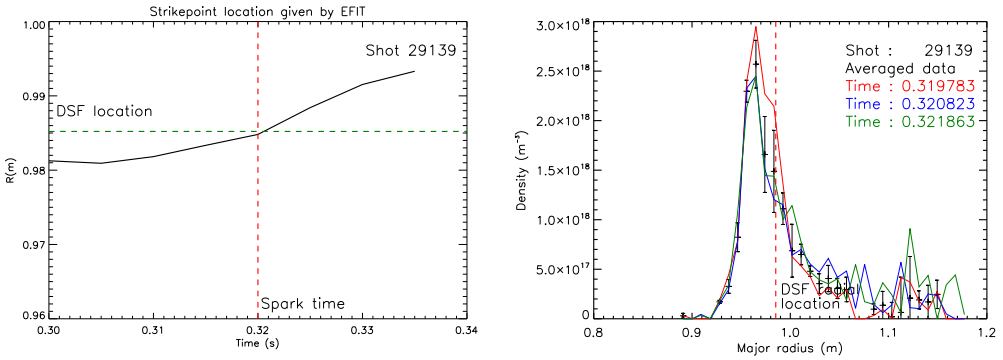

(a) EFIT

(b) Divertor LPs

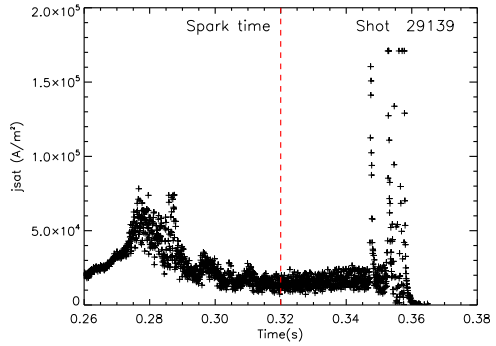

(c) Injector LP

Figure 3.9: EFIT and LP data from shot 29139 showing the strike point position at the injection time of 320ms. a) Strike point location plotted against time shows the strike point moving outwards until it crosses the injector head then moves inwards again. b) Radial density profile from the divertor Langmuir probes, the strike point lies close to the peak of this profile. c) Saturation current from the on-board Langmuir probe plotted against time showing an increase just before the injections time as the strike point crosses the injector.

interest. It can be seen that there is no evidence for significant perturbation of the background plasma.

3.2.4 Electron temperature and density data

Target data

Langmuir probes are installed on both the upper and lower divertor on MAST. For the six shots of interest strike point data was only available from the outer divertor arrays. In the case of the upper inner divertor probes the amplifier used to drive the probes was used to drive the probe on the injector head. For the lower inner divertor the strike point was too high to register on the probes at the time of the injection. For shot 29139 no Langmuir probe data exists however shot 29142 was a repeat of this shot so the data taken in 29142 is used for simulation of 29139. Data for shots 29125, 29126 and 29139/29142 can be seen in figures 3.11, 3.12 and 3.13.

A spline fit to the data has also been plotted over the raw data. This fit was used as input for simulation, see section 5.2.2. The data has been averaged over 3 timeslices from centre on the injection time. The lower target data for shot 29139 has also been shifted radially so that the density peak aligns with the strike point location calculated by EFIT as there is significant error in the EFIT reconstruction. For the L-mode shot 29126 and H-mode shot 29139 the upper divertor temperature data appears to be purely noise, this data has been fixed at an value of 6eV. The initial data can be seen as crosses on all plots. In the presence of magnetic fields Langmuir probes are sensitive to the angle of incidence of the field, this has been accounted for simplistically by using the projected area of the Langmuir probes with respect to the incident magnetic field.

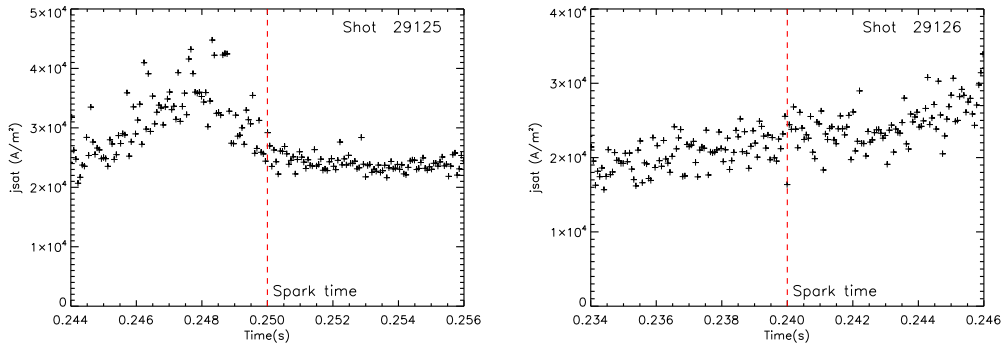

(a) 29125

(b) 29126

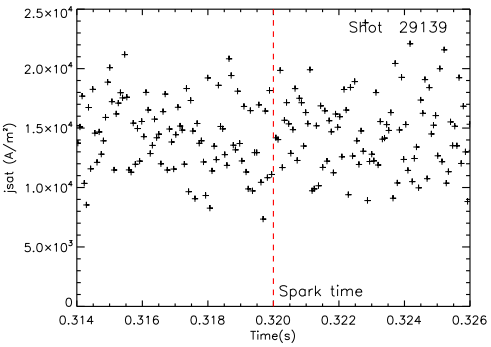

(c) 29139

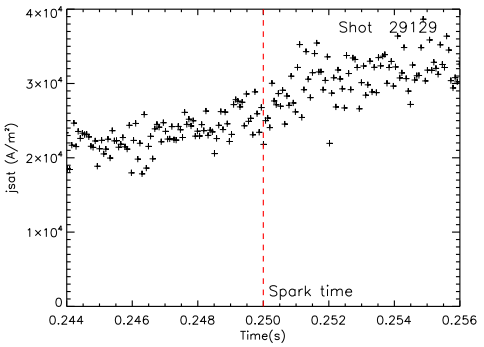

(d) 29129

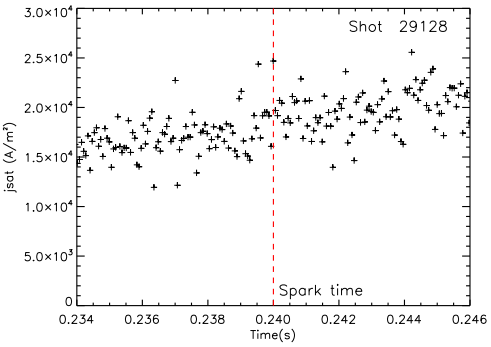

(e) 29129

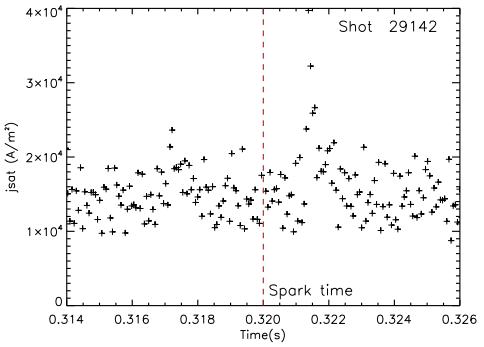

(f) 29142

Figure 3.10: Saturation current plotted against time taken from the on-board Langmuir probe. There is no discernible perturbation seen at the injection time for each shot, shown by a dashed vertical line.

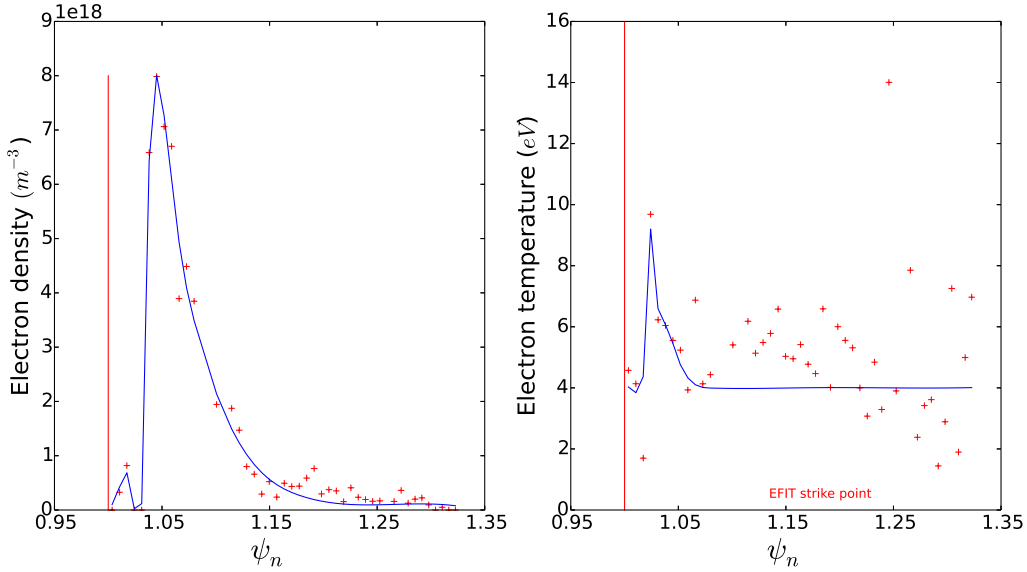

(a) Upper divertor

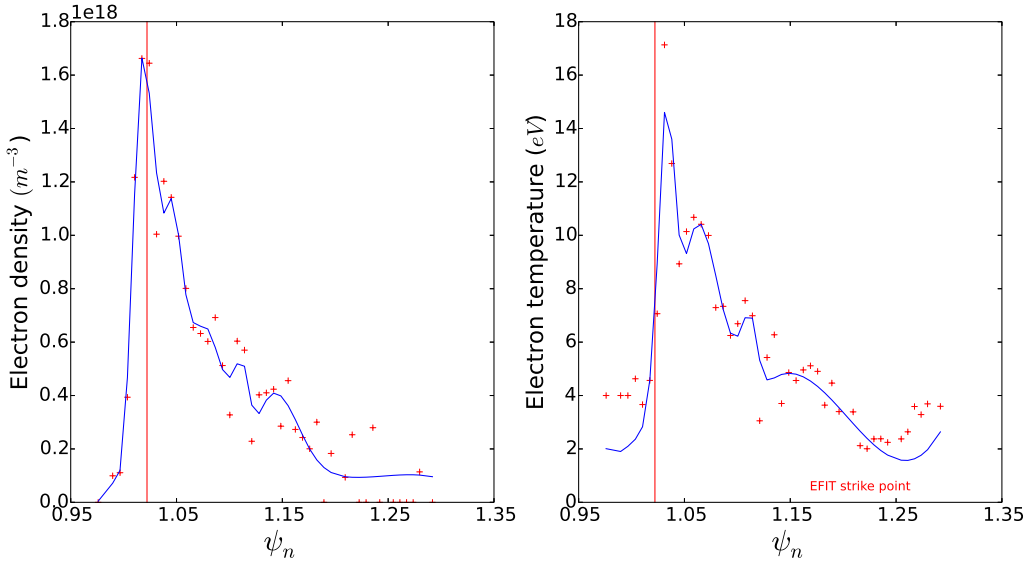

(b) Lower divertor

Figure 3.11: Outer target electron density and temperature data against normalised poloidal flux for L-mode shot 29125. The measured data is represented by crosses and the data used in simulation by the solid line.

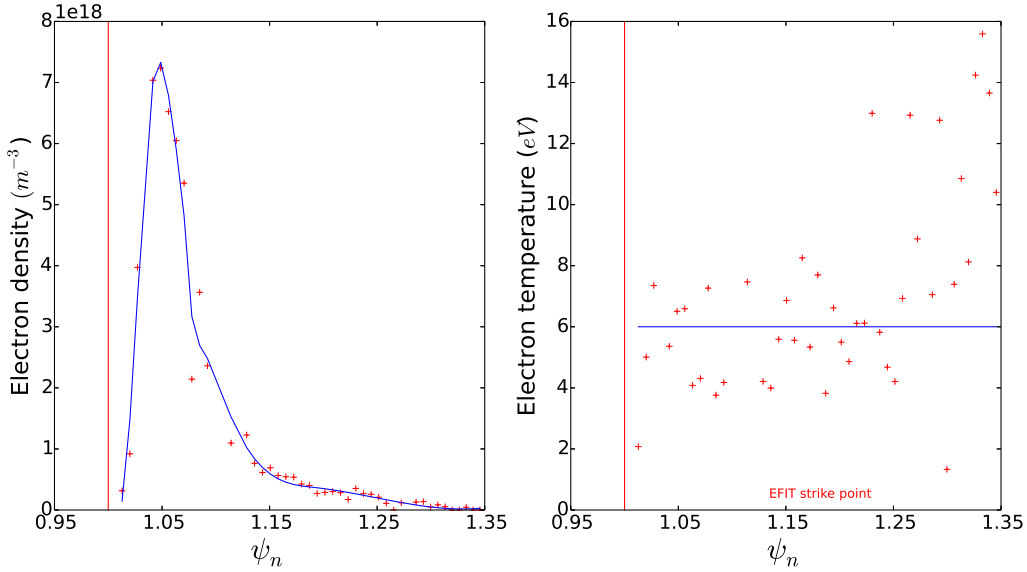

(a) Upper divertor

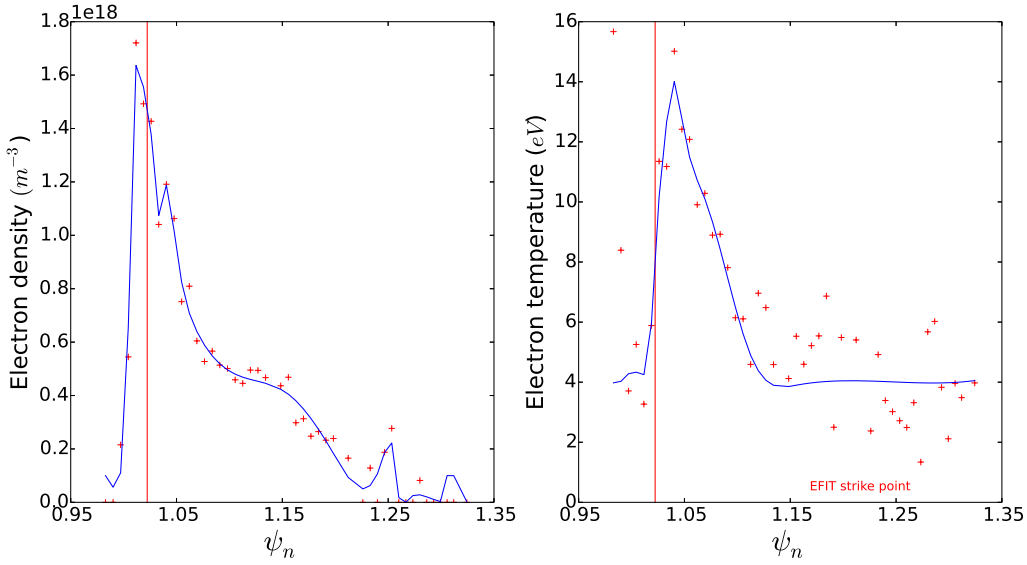

(b) Lower divertor

Figure 3.12: Outer target electron density and temperature data against normalised poloidal flux for L-mode shot 29126.The measured data is represented by crosses and the data used in simulation by the solid line.

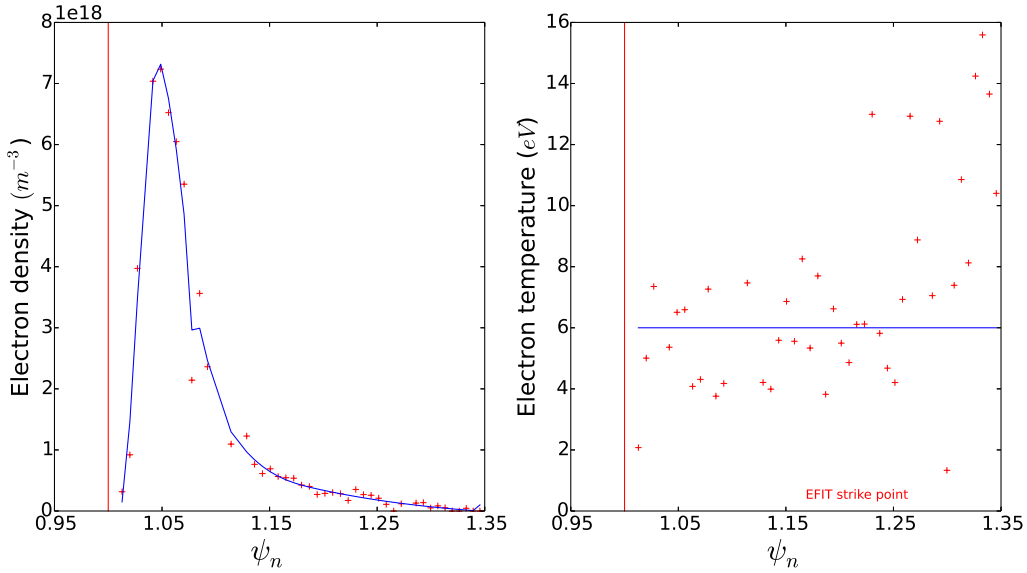

(a) Upper divertor

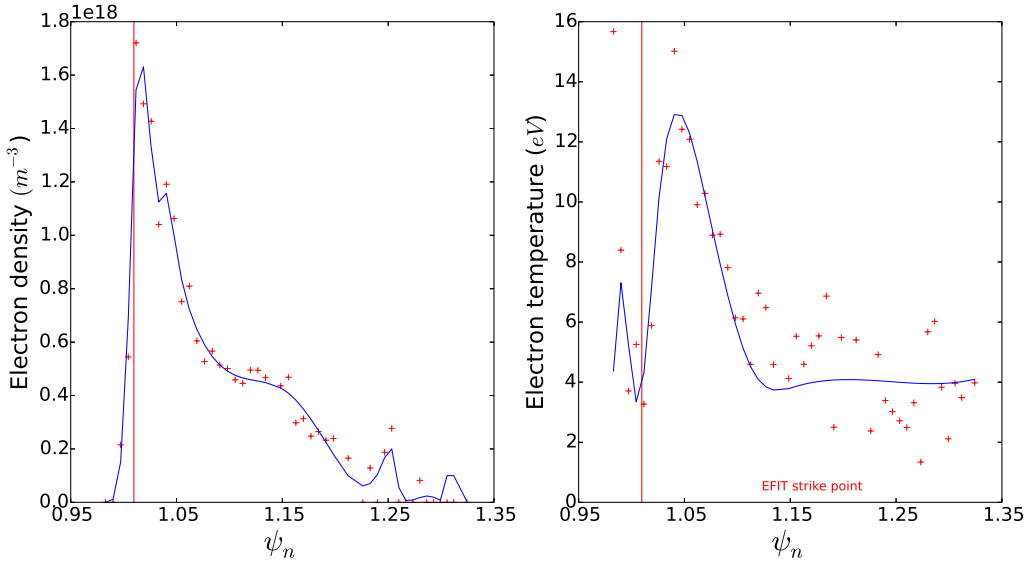

(b) Lower divertor

Figure 3.13: Outer target electron density and temperature data against normalised poloidal flux for H-mode shot 29139. The measured data is represented by crosses and the data used in simulation by the solid line.

Midplane data

The Thomson scattering system on MAST was operated in burst mode, whereby 8 measurements are taken $500\mu s$ apart over a $3.5ms$ interval giving improved diagnostic coverage at the time in question. This also provides a measure of the potential perturbation caused by the injection. No significant difference was observed in the density or temperature signals after the injection, showing that any perturbation caused by the injection was not large enough to propagate upstream as far as the midplane. Figure 3.14 show the density and temperature data for shots 29125, and 29139 averaged over the 5 time slices. Spline fits are included as for the target data. Data from the low field side and high field side were overlayed before averaging. Ideally one would use the respective data from the low and high field sides, however the noise on the low field side data made this data unusable for modelling purposes.

3.2.5 Flow data

Flow data taken from the coherence imaging diagnostic (see section 1.3.1) can be seen for shots 29125, 29126 and 29139 in figure 3.15. The measured flow values are line averaged along the line of sight of the diagnostic. The data seen here is projected from the image plane onto the R,Z plane where the line of sight is tangential to the toroidal magnetic field and do not take into account either the field line angle or the distribution of flow along the line of sight. However the principle contribution to the average flow is from the tangential component of the line of sight, so that the values serve as a useful guide for comparison with simulation. This data will be discussed further in section 5.2.3.

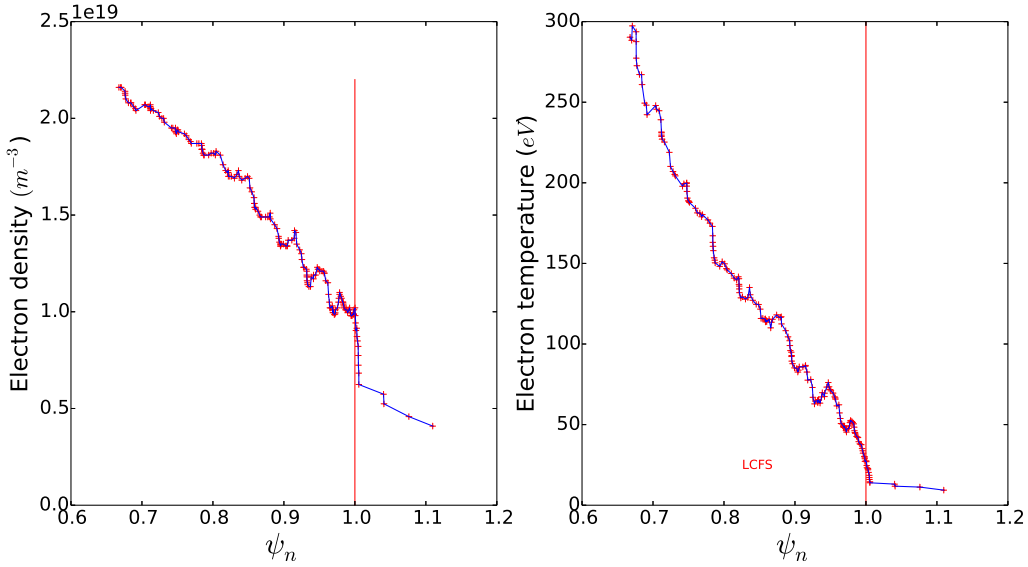

(a) Shot 29125

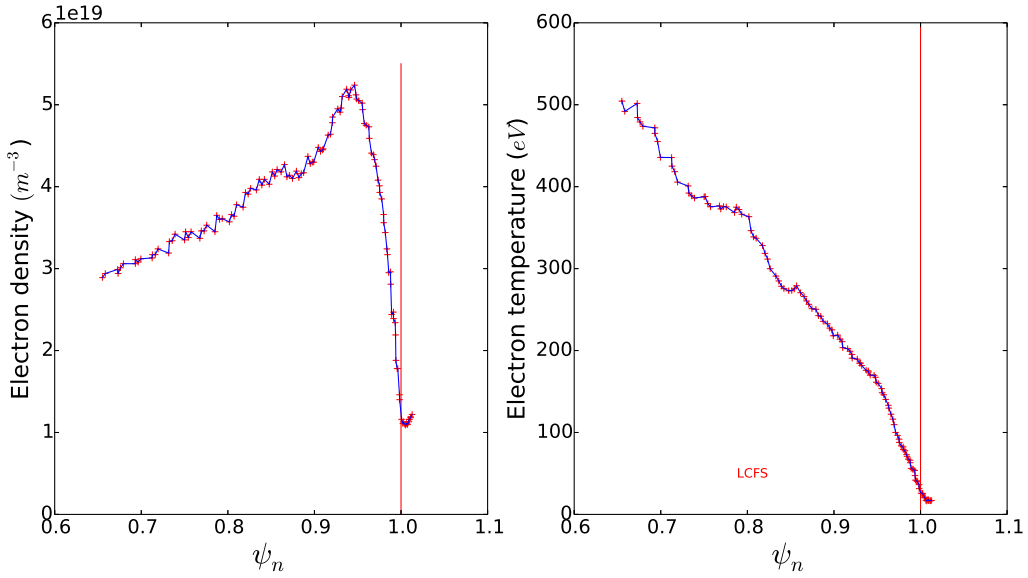

(b) Shot 29139

Figure 3.14: Midplane electron density and temperature data for shot 29125 and 29139 against normalised poloidal flux. Data from the high and low field sides have been combined.

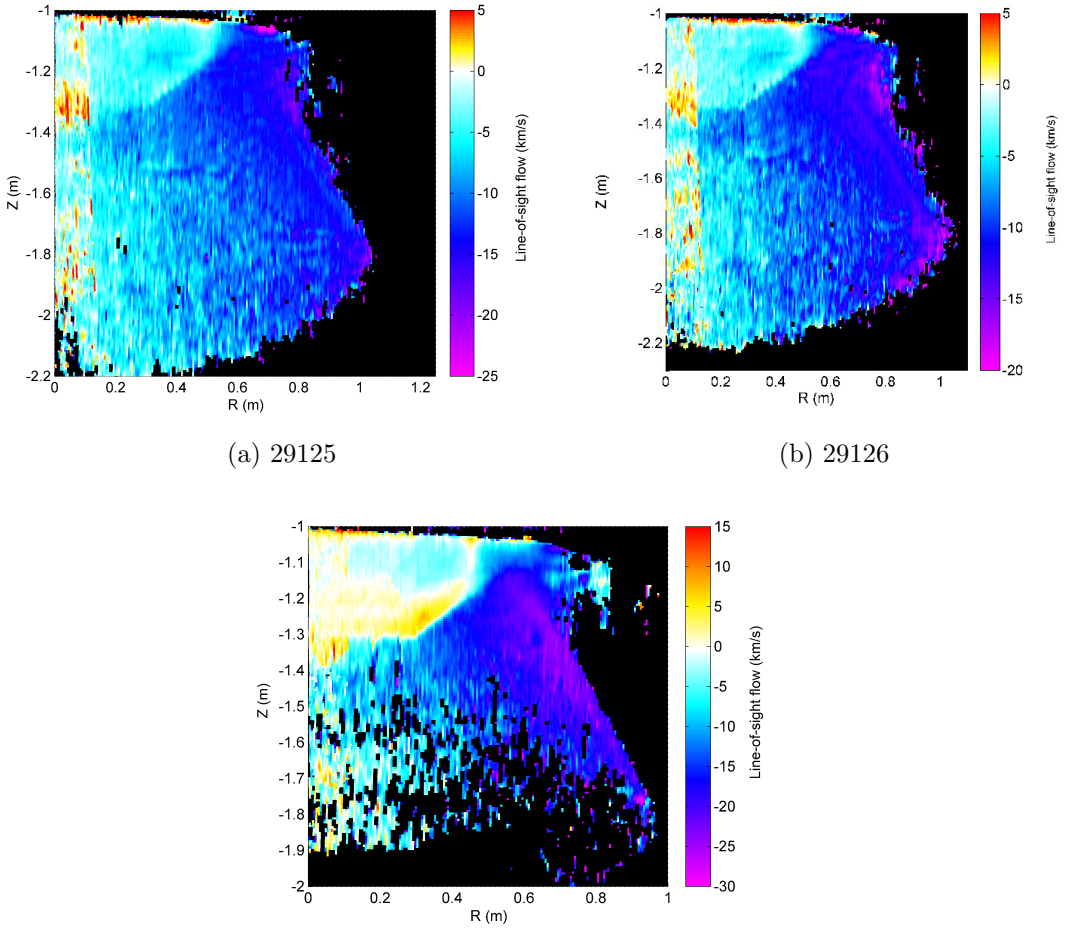

(a) 29125

(b) 29126

(c) 29139

Figure 3.15: Flow data taken using the coherence imaging diagnostic measuring carbon III emission [1].

CHAPTER 4

Image processing and analysis

4.1 Acquired CCD data

The data from the filtered fast cameras is the principle diagnostic data resulting from the injection experiments. Figures 4.1 and 4.2 show unprocessed images from both sectors showing the camera view and an example of injection respectively. Although these shots are from the first set of experimental sessions and will not be discussed further they are useful as an example of the raw data taken by the cameras.

For shots 29125 to 29142 the camera on sector 1 ran with a frame rate of $75kHz$ while the camera on sector 11 ran at $100kHz$. Both cameras integrated over the full duty cycle with integration times $13.3\mu s$ and $10.0\mu s$ respectively. The remainder of this section will discuss the images taken and the processing applied to each image for shots 29125, 29126, 29128, 29129,

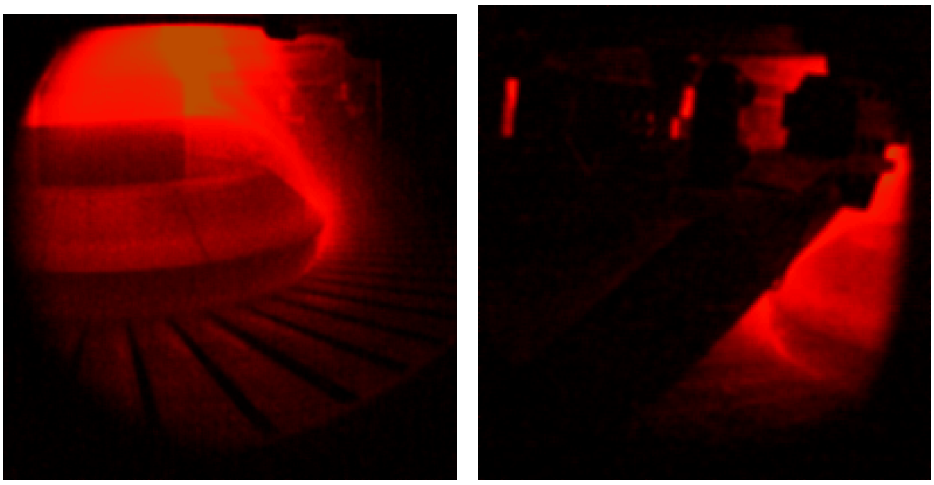

(a) Sector 1 (b) Sector 11

Figure 4.1: Unfiltered images from both sectors showing the actual camera views.

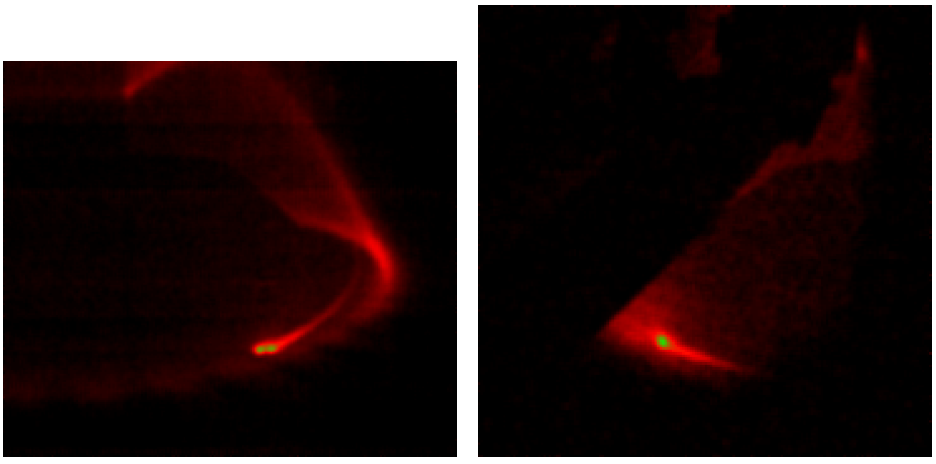

(a) Sector 1 (b) Sector 11

Figure 4.2: Unprocessed images from both sectors showing CII filtered images from shot 27075. Injection location 4cm into the private flux zone with an integration time of $33\mu s$.

29139 and 29142.

4.1.1 Camera Calibration

Only one of the Photron cameras used for the imaging was calibrated in the laboratory, it is assumed that the other camera, of identical make, has the same sensitivity. Although this is unlikely to be strictly true there is a high level of error inherent in the calibration, making this assumption valid within errors. Calibration was performed in a laboratory environment using a light source with a set luminance of $24.723 kcd/m^2$. The calibration images and a horizontal slice of the calibration coefficients for the carbon II, carbon III and D_α filters can be seen in figure 4.3, no calibration data was taken for the carbon I filter.

4.2 Magnetic field projection

The goal of this thesis is to compare the parallel transport of impurities with simulation. This is quantified by projecting the magnetic field onto the images taken and measuring the emission along the projected field line. It is assumed that transport along the field line dominates so that the injected carbon remains bound to the field line and any observed emission originates from that field line. This can then be compared to the emission from the relevant flux tube in the simulation.

4.2.1 Camera registration and field line projection

In order to accurately project the magnetic field onto the captured images it is necessary to accurately know the 2 dimensional magnetic field and the position and optical characteristics of the cameras. The magnetic field is

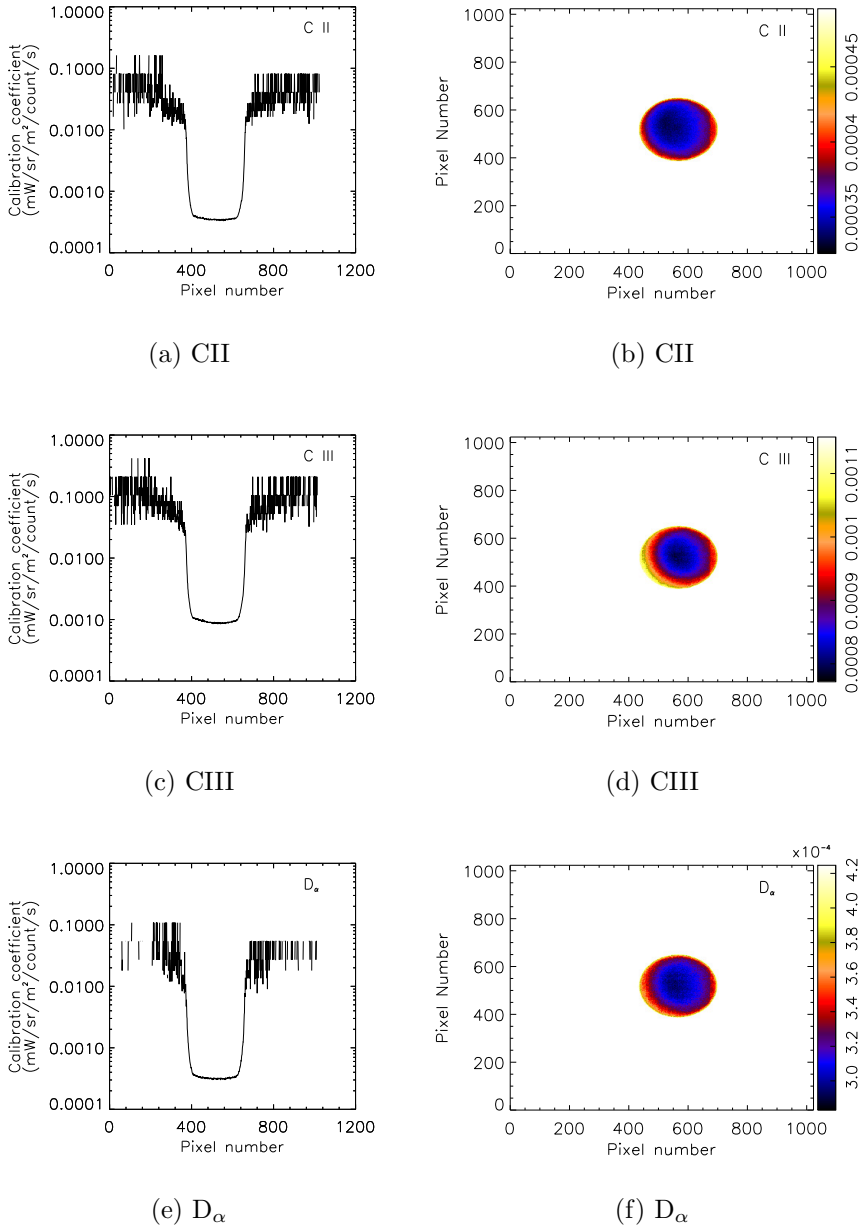

(a) CII (b) CII

(c) CIII (d) CIII

(e) D_α (f) D_α

Figure 4.3: Calibration curves for the carbon II, carbon III and D_α filters.

Parameter	Sector 1	Sector 11
no x pixels	96	128
no y pixels	128	64
x centre	48.5	64
y centre	64.5	128
focal length	5.8mm	5.5mm
x position	0.68m	-1.47m
y position	2.21m	1.50m
z position	-1.18m	-1.34m
pitch	30.6°	-51.45°
roll	-112.5°	-109.0°
yaw	170.9°	-164.0°
pixel size	$17\mu m$	$17\mu m$

Table 4.1: Camera registration

obtained from EFIT, while the camera position must be calculated using software available on MAST. Camera images are compared to wire-frame models of the MAST vessel and matching pixels are manually indicated on the image and the model. The software then performs a minimisation on the variable parameters of the system. The calculated parameters can be seen for both cameras in table 4.1. The locations given in table 4.1 result in a spatial resolution at the point of injection of $5.1mm/pixel$ for the sector 1 camera and $4.5mm/pixel$ for the sector 11 camera. At the furthest visible extent of the plume the resolution becomes $6.2mm/pixel$ for the sector 1 camera and $7.8mm/pixel$ for the sector 11 camera.

In order to project field lines onto the camera images it is necessary to first calculate the path of the field line. This is done using a fourth order

Runge-Kutta method described here.

$$\mathbf{P_0} = (R, Z, \Phi) \tag{4.1}$$

$$\mathbf{k_1} = \mathbf{P_0} + \frac{\delta x \mathbf{B_0}}{2 \times |\mathbf{B}|} \tag{4.2}$$

$$\mathbf{k_2} = \mathbf{k_1} + \frac{\delta x \mathbf{B_1}}{2 \times |\mathbf{B}|} \tag{4.3}$$

$$\mathbf{k_3} = \mathbf{k_2} + \frac{\delta x \mathbf{B_2}}{2 \times |\mathbf{B}|} \tag{4.4}$$

$$\mathbf{P_{i+1}} = \mathbf{P_i} + \frac{1}{6}(\mathbf{k_1} + \mathbf{2k_2} + \mathbf{2k_3} + \mathbf{k_4}) \tag{4.5}$$

The field line is followed in both directions from a given starting point providing a set of points in 3 dimensions. These points are then projected onto the image plane of the camera to give the final projection.

4.3 Image processing

In order to clearly identify the injected plume the plasma background must be subtracted from the images of the injection. This is done using the frame immediately before the injection and results in a clearly defined plumes. A contour map is used to show the relative emission intensity from each plume in successive frames after the injection. Figures 4.4 to 4.15 show these background subtracted images filtered to the carbon II emission line for both sectors. Magnetic field lines have been projected onto the image, the first of these originates at the injection location, while further field lines are added at regular intervals of poloidal angle in order to aid the visual interpretation of the images. In the case of shot 29125 significant emission in the frame taken at the injection time appears at a different location to the centre of the DSF. This appears to be approximately $2cm$ above the top of the injector head and so the projected field line is taken to originate at this point. This is

likely due to neutral carbon being injected upwards until it is ionised by the hot plasma close to the separatrix and provides evidence that the injection location was inside the outer strike point for this shot and, not on the strike point as indicated by EFIT and the divertor Langmuir probes (see 3.2.3). For shots 29126 and 29139 the initial emission appears close to the centre of the DSF so the projected field line is originated at this point.

4.3.1 CII emission

For shots 29125, 29126 and 29139 carbon II filters were used on both cameras. Figures 4.4 to 4.9 show calibrated emission from each of these cameras as well as projections of the magnetic field lines originating at the divertor to aid in visualisation.

4.3.2 CI and CIII emission

For shots 29128, 29128 and 29142 a carbon I filter at 910nm was used on the sector 1 camera and a carbon III filter at 465nm was used on the sector 11 camera. Background subtracted images of these shots can be seen in figures 4.10 to 4.15 along with field line projections as in the previous images. None of the images taken using carbon III filters on sector 11 show significant emission aligned with the magnetic field apart from at the injection location, however the full set of images has been included for completeness. Some emission can be seen in the sector 1 view of H-mode shot 29142 using a CIII filter, however this emission is only just detectable by the camera and only just above the level of noise. It should be noted that for this shot the highest charging voltage of $2.4kV$ was used and as an H-mode plasma conditions are hotter than in the 2 L-mode shots. Similarly no significant CI emission was observed for the sector 1 views using CI filters apart from at the injection

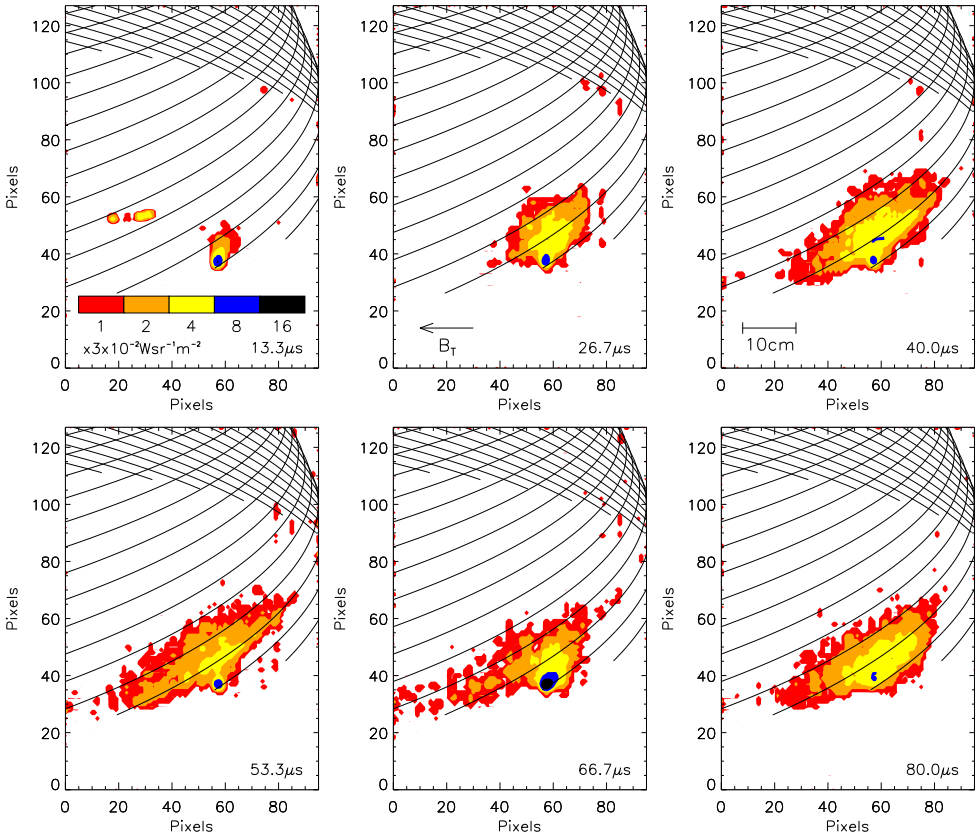

Figure 4.4: Contour plots of the carbon plumes from L-mode pulse 29125 imaged from sector 1 using a CII filter at 515nm. The images are each separated by $13\mu s$. Magnetic field lines originating at the injection radius can be seen projected onto the image.

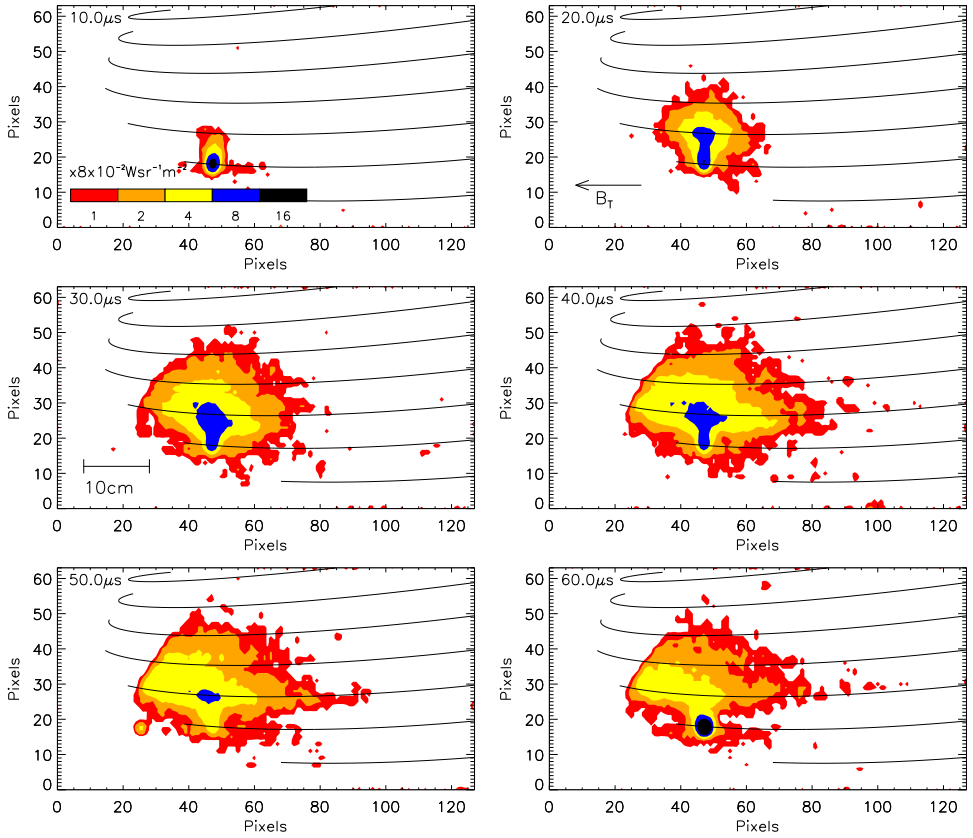

Figure 4.5: Contour plots of the carbon plumes from L-mode pulse 29125 imaged from sector 11 using a CII filter at 515nm. The images are each separated by 13μs. Magnetic field lines originating at the injection radius can be seen projected onto the image.

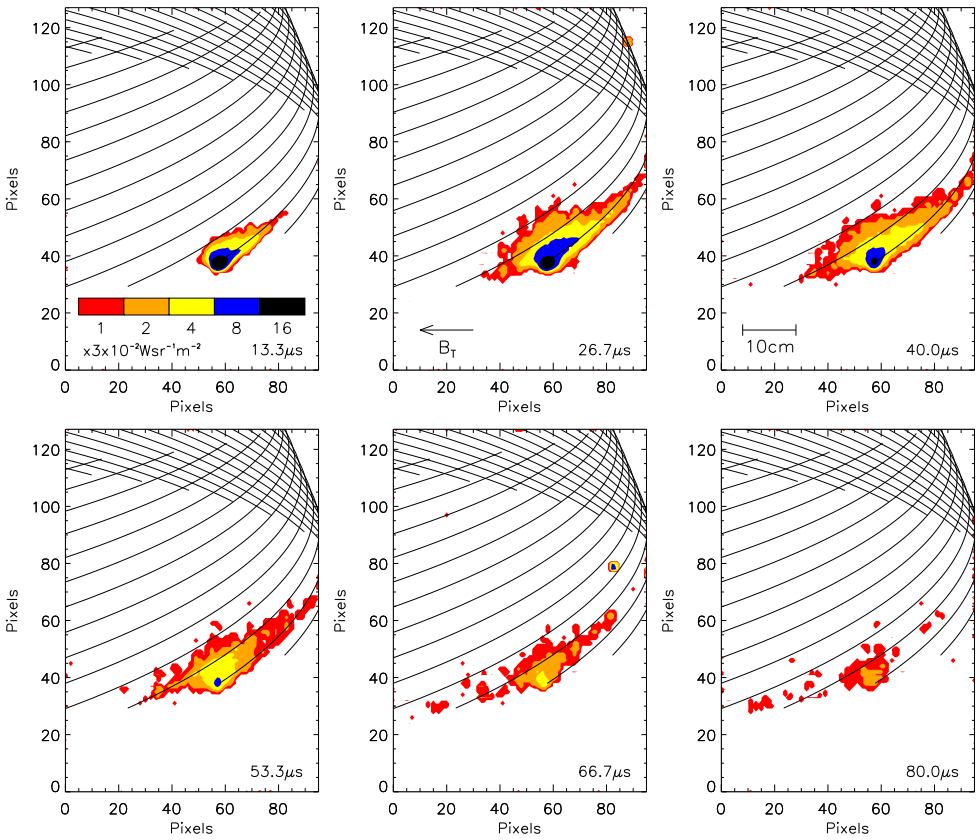

Figure 4.6: Contour plots of the carbon plumes from L-mode pulse 29126 imaged from sector 1 using a CII filter at 515nm. The images are each separated by $13\mu s$. Magnetic field lines originating at the injection radius can be seen projected onto the image.

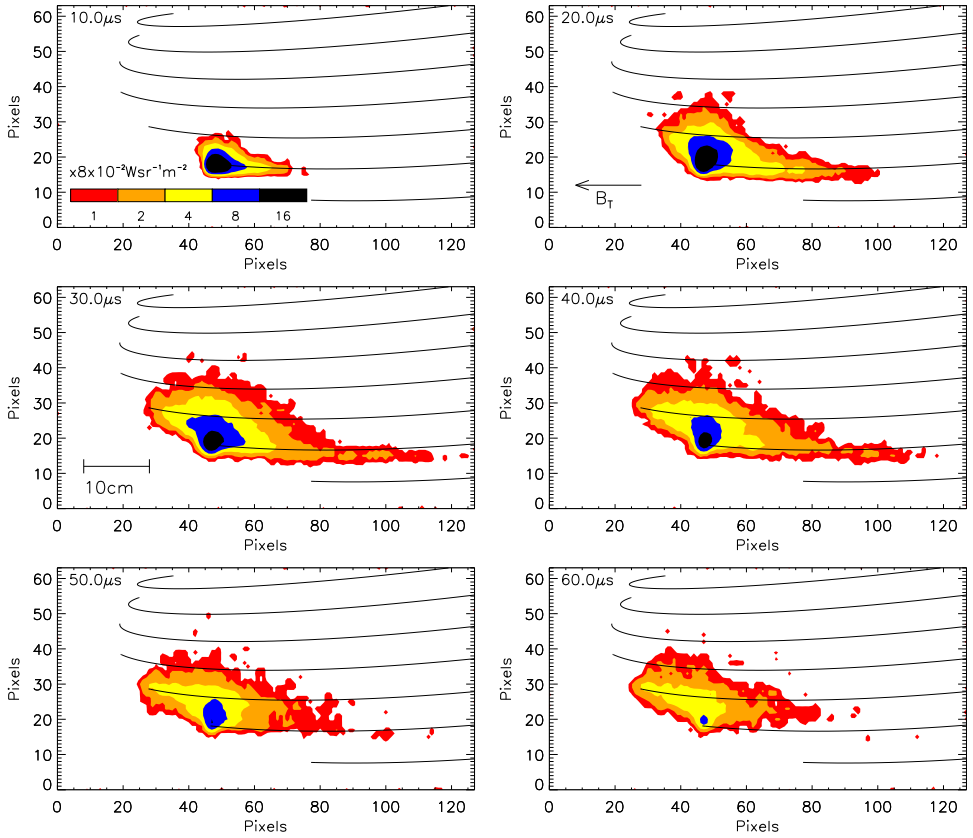

Figure 4.7: Contour plots of the carbon plumes from L-mode pulse 29126 imaged from sector 11 using a CII filter at 515nm. The images are each separated by $10\mu s$. Magnetic field lines originating at the injection radius can be seen projected onto the image.

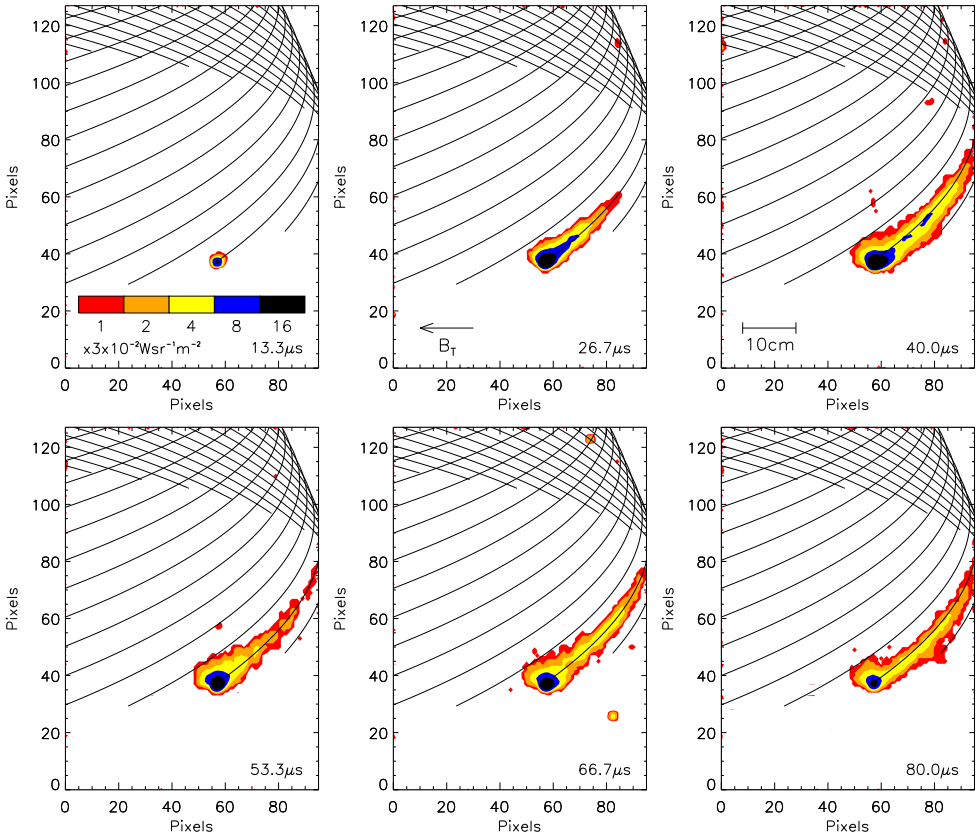

Figure 4.8: Contour plots of the carbon plumes from H-mode pulse 29139 imaged from sector 1 using a CII filter at 515nm. The images are each separated by $13\mu s$. Magnetic field lines originating at the injection radius can be seen projected onto the image.

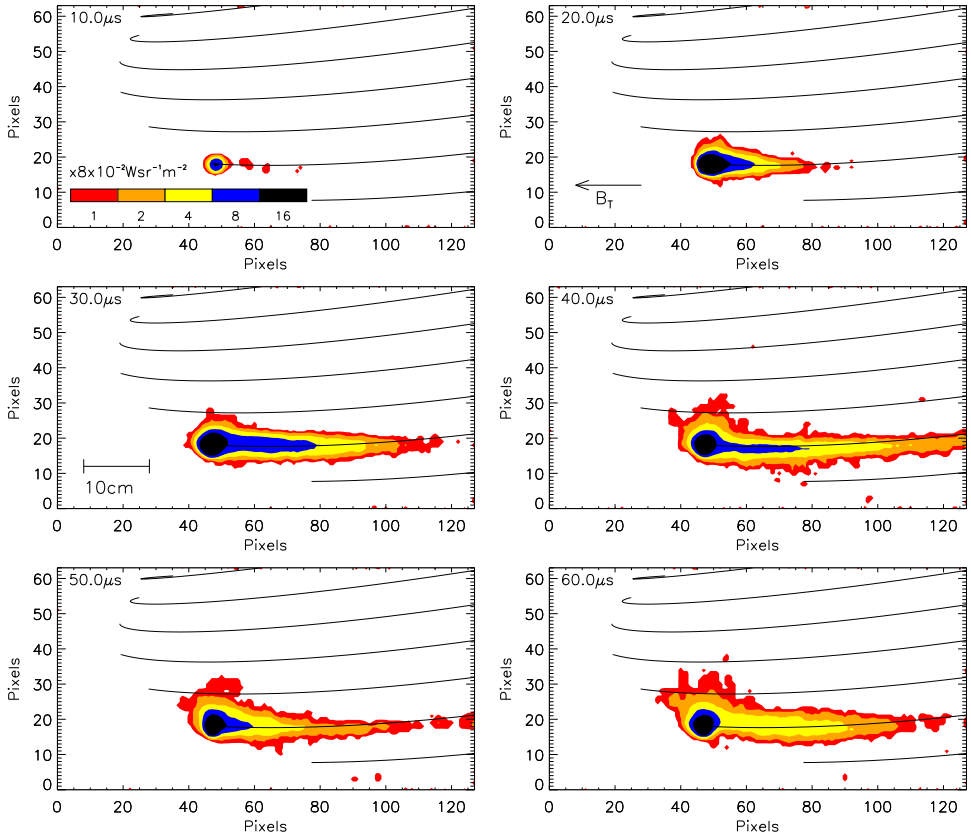

Figure 4.9: Contour plots of the carbon plumes from H-mode pulse 29139 imaged from sector 11 using a CII filter at 515nm. The images are each separated by $10\mu s$. Magnetic field lines originating at the injection radius can be seen projected onto the image.

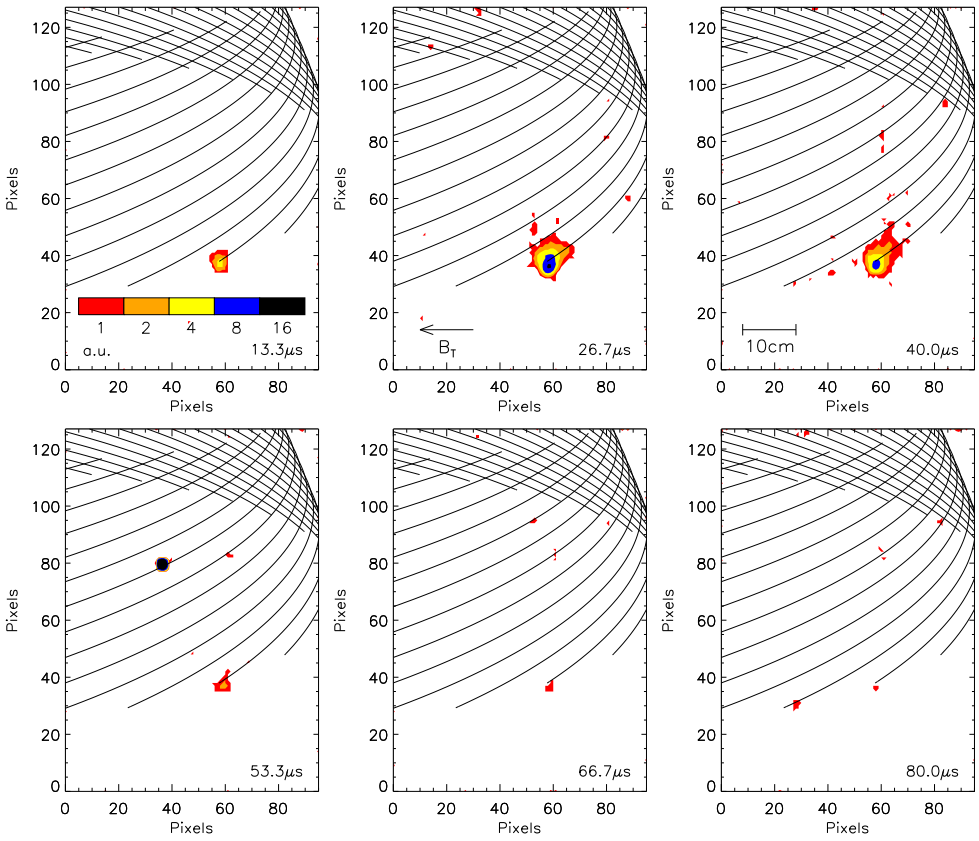

Figure 4.10: Contour plots of the carbon plumes from L-mode pulse 29128 imaged from sector 1 using a CI filter at 910nm. The images are each separated by 13μs. Magnetic field lines originating at the injection radius can be seen projected onto the image.

location. This is likely due to the carbon quickly ionising once in contact with the plasma.

4.4 Emission parallel to the magnetic field

A measure of the parallel transport of the injected carbon is obtained by reading the emission from the images (see 4.3) along the path of the projected

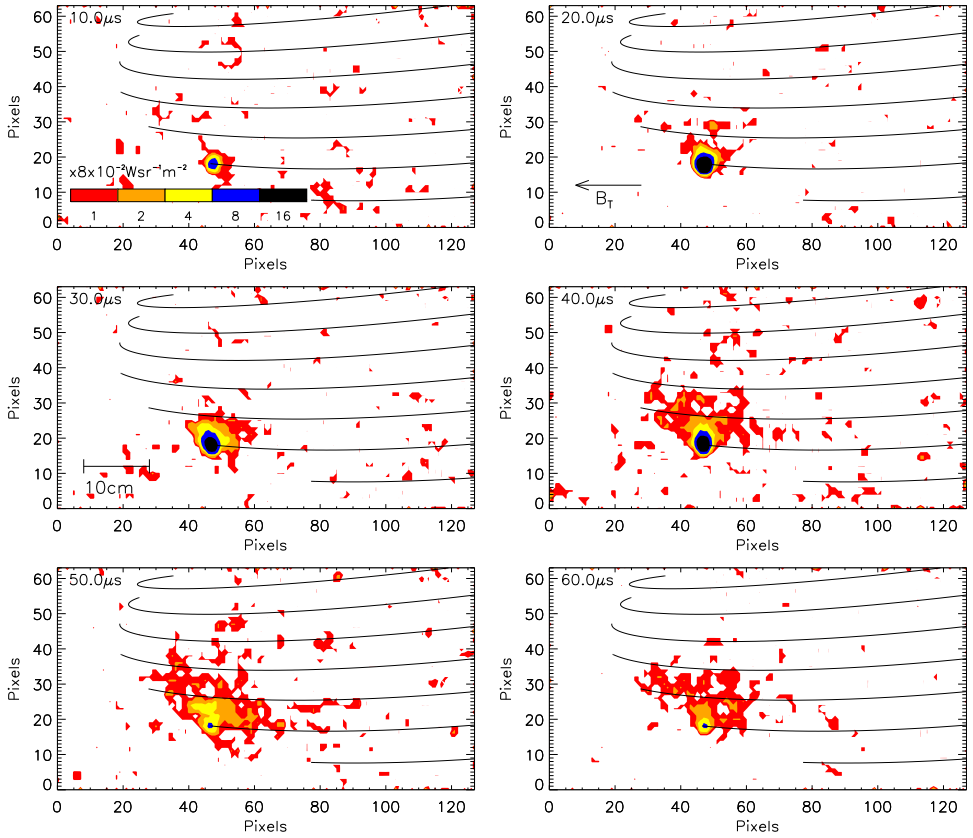

Figure 4.11: Contour plots of the carbon plumes from L-mode pulse 29128 imaged from sector 11 using a CIII filter at 465nm. The images are each separated by $10\mu s$. Magnetic field lines originating at the injection radius can be seen projected onto the image.

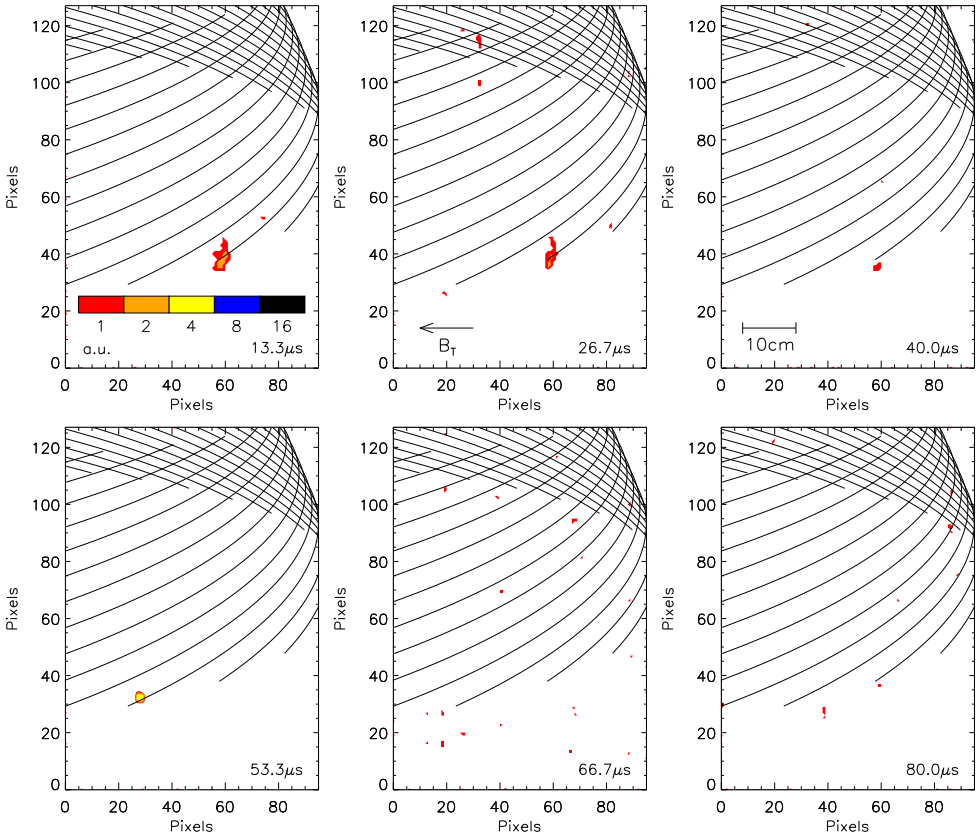

Figure 4.12: Contour plots of the carbon plumes from L-mode pulse 29129 imaged from sector 1 using a CI filter at 910nm. The images are each separated by 13μs. Magnetic field lines originating at the injection radius can be seen projected onto the image.

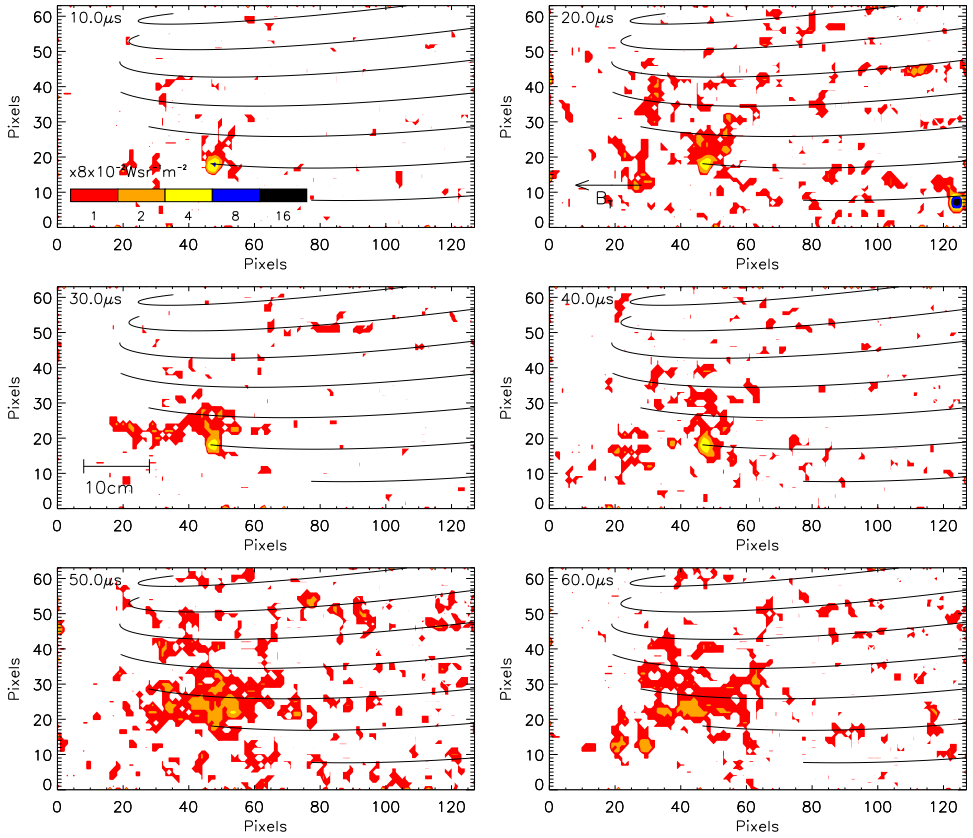

Figure 4.13: Contour plots of the carbon plumes from L-mode pulse 29129 imaged from sector 11 using a CIII filter at 465nm. The images are each separated by $10\mu s$. Magnetic field lines originating at the injection radius can be seen projected onto the image.

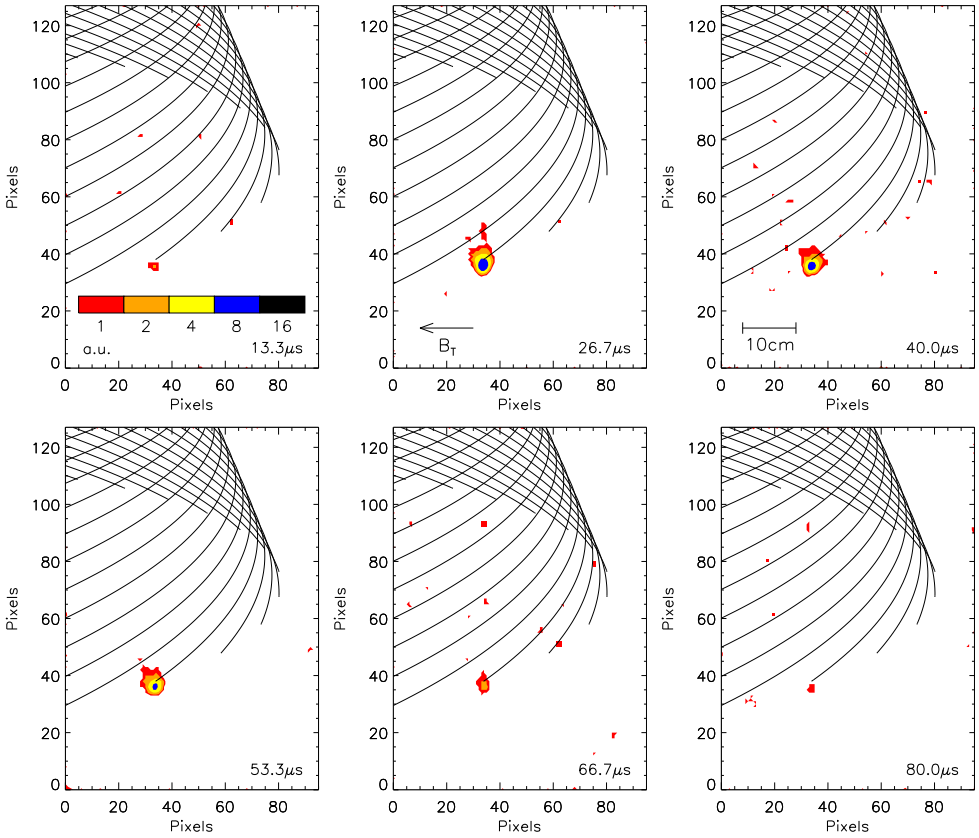

Figure 4.14: Contour plots of the carbon plumes from H-mode pulse 29142 imaged from sector 1 using a CI filter at 910nm. The images are each separated by 13μs. Magnetic field lines originating at the injection radius can be seen projected onto the image.

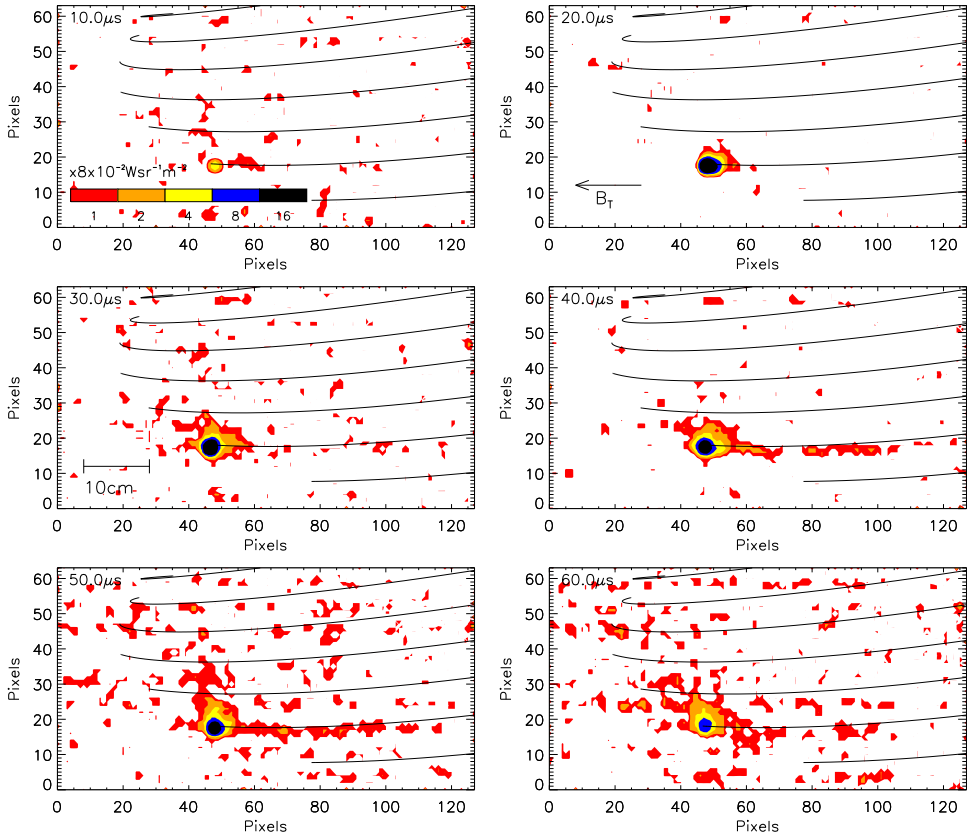

Figure 4.15: Contour plots of the carbon plumes from H-mode pulse 29142 imaged from sector 11 using a CIII filter at 465nm. The images are each separated by $10\mu s$. Magnetic field lines originating at the injection radius can be seen projected onto the image.

field starting at the injection location. The images are first smoothed over 2 pixels using the IDL Gaussian smoothing algorithm. This reduces the noise without significantly affecting the absolute measured emission. This line integrated emission along the projected magnetic field can be seen in figures 4.16, 4.17 and 4.18. This is compared to results obtained from simulation in section 5.4. The data from the H-mode shot 29139 shows a clear expansion along the field line and an estimate of the impurity parallel velocity can be made of $14 \pm 3ms^{-1}$.

4.5 Repeat injection

In several cases a second discharge occurred after $60\mu s$. Examples of this can be seen in figure 4.19. In the frame immediately preceding the second discharge the visible plumes were at the lower limit of sensitivity of the CCDs, indicating that the following frame would not have provided further significant information on transport. Due to this, and considering the added complexity of modelling a second impurity injection while impurities were still present in the plasma data from the injection due to the second discharge will not be used for comparison with simulation. This second discharge did not occur during the initial set of experiments and it is possible that a change to the charge carrying cable in the vacuum system from coaxial to single core increased the inductance of the system and caused a second delayed current pulse. This change was made for reasons of mechanical reliability and could potentially be reversed if suitable coaxial cable were used.

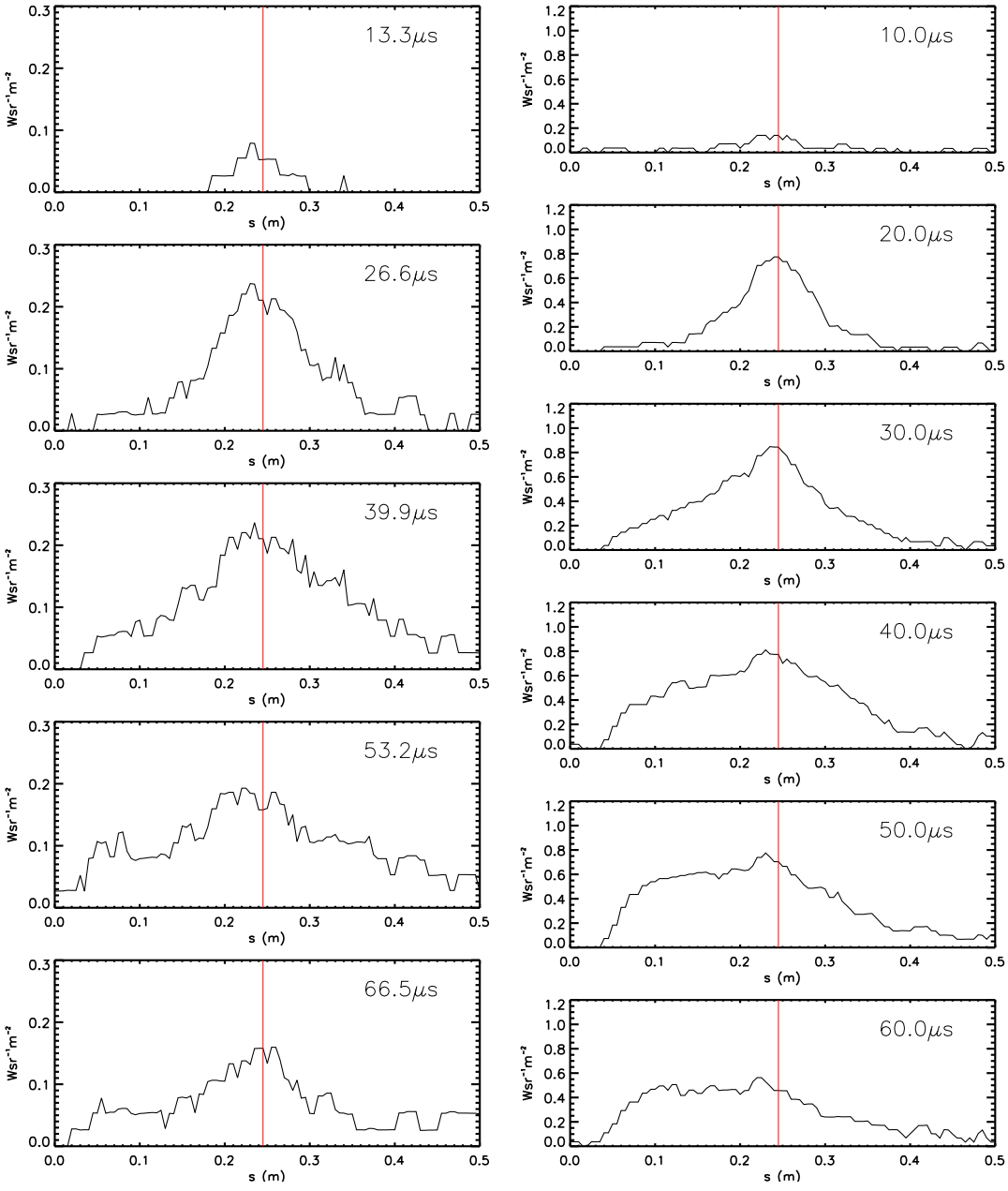

(a) Sector 1 (b) Sector 11

Figure 4.16: CII emission intensity along the field line from sectors 1 (a) and 11 (b) for shot 29125

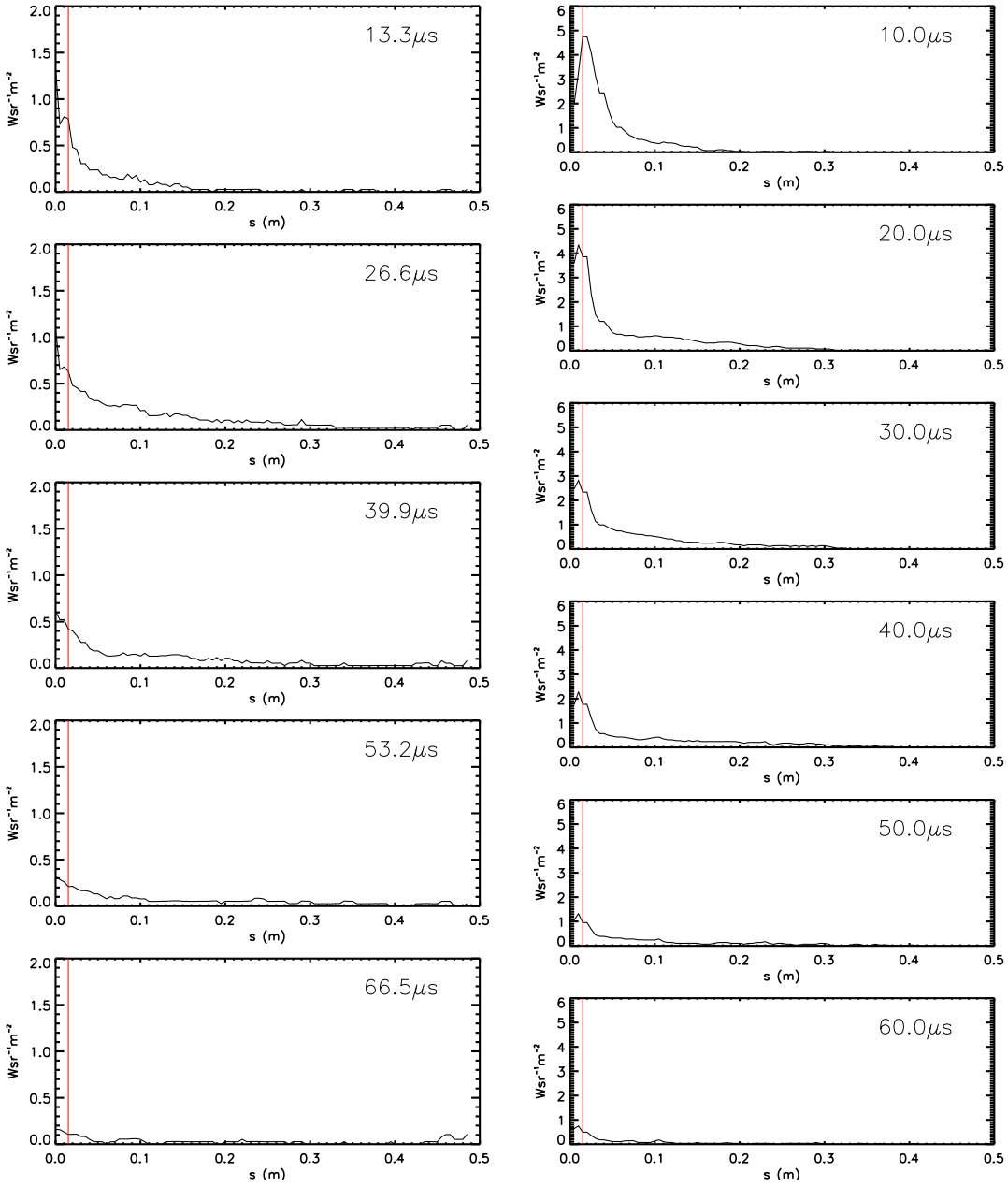

(a) Sector 1 (b) Sector 11

Figure 4.17: CII emission intensity along the field line from sectors 1 (a) and 11 (b) for shot 29126

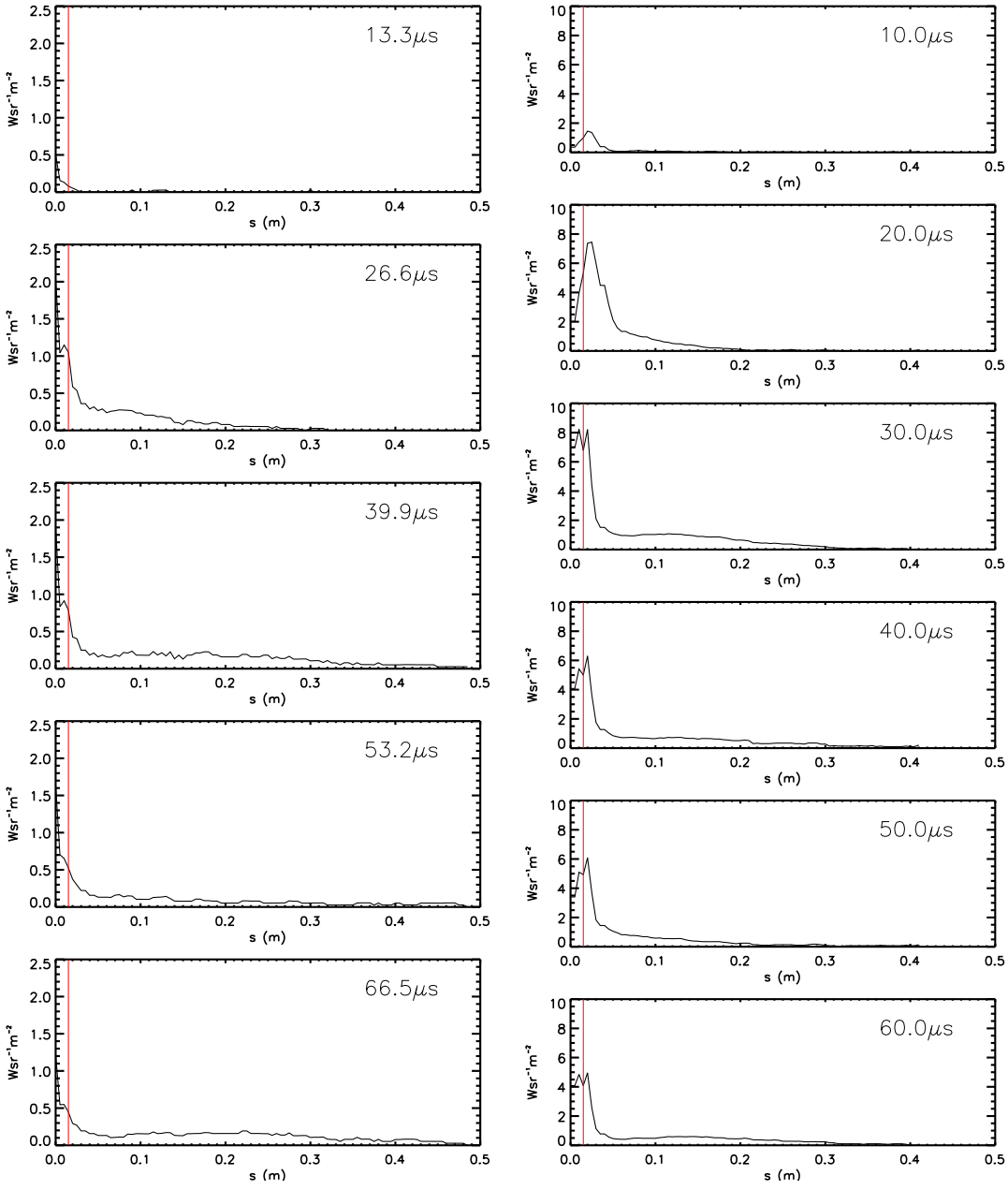

(a) Sector 1 (b) Sector 11

Figure 4.18: CII emission intensity along the field line from sectors 1 (a) and 11 (b) for shot 29139

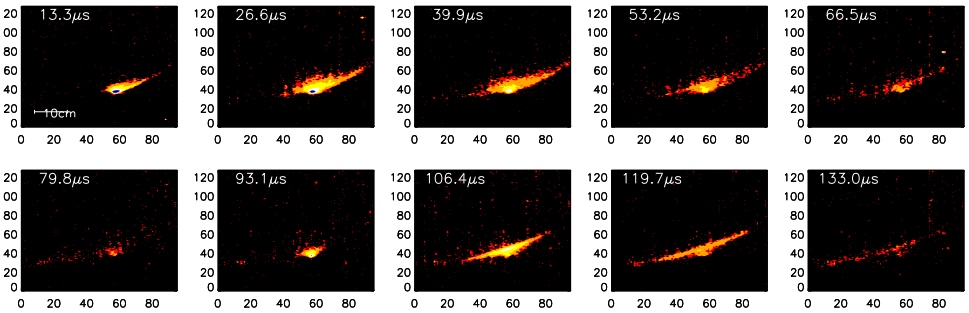

(a) 29126

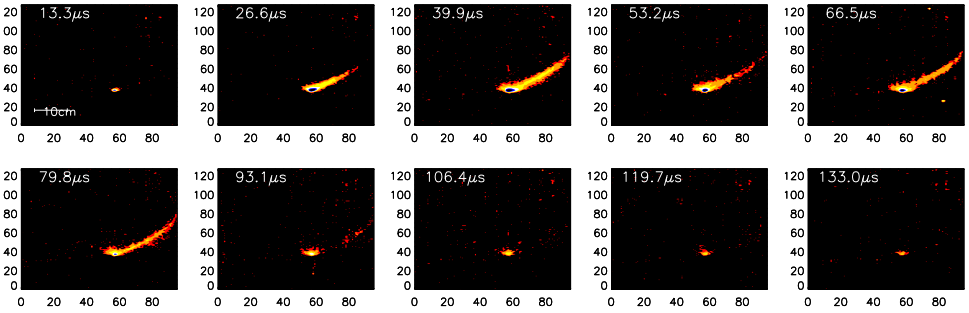

(b) 29139

Figure 4.19: Secondary injection. CII filtered images taken from shot 29126 (a) and shot 29139 (b) showing the initial injection in the first frame and a secondary burst of carbon in frames 7 and 5 respectively.

CHAPTER 5

DIVIMP Simulation

5.1 OSM-EIRENE-DIVIMP

The data obtained from experiment was compared with simulation using the OSM-EIRENE-DIVIMP set of codes see 1.4.7. This package is currently being used in ITER modelling, the results of which are used being used to guide the ITER design. OSM (see 1.4.5) simulates the hydrogenic background plasma by solving a set of 1D fluid equations parallel to the magnetic field, EIRENE provides the neutral dynamics and DIVIMP uses a Monte-Carlo method to follow impurity particles on the plasma background.

5.1.1 OSM

As described in section 1.4.5 OSM performs interpretive modelling of the plasma SOL, in that the goal is to provide as complete a description of

the SOL given the available experimental data. The code provides a number of different methods for creating the independent 1D plasma solutions along each flux tube, all tailored towards certain plasma conditions. The method used here is SOL option 28, also used in current ITER simulations. This method is not currently included in the DIVIMP documentation[161] although has previously been used to simulate DIII-D plasmas[162].

A reconstruction of the magnetic equilibrium from a code such as EFIT is used to create a grid containing a series of tubes of constant flux, see figure 1.2. Each flux tube is then split into an upper and lower section by prescribing a 'symmetry' point approximately halfway between the upper and lower targets. The temperature along each half tube is then prescribed by interpolating from data at the targets to data at the symmetry point and assuming $T_e = T_i$. For this case a 7/2 power law was used, based on the assumption that the parallel transport is conduction dominated. This temperature profile is then used to solve the mass and momentum conservation equations

$$\frac{d}{ds}(n_i v_i) = S_{particle} + A_{particle} \tag{5.1}$$

$$\frac{d}{ds}(T_e + T_i + m_i n_i v_i^2) = S_{momentum} + A_{momentum} \tag{5.2}$$

where s is the distance along the flux tube and the final term in each case is an anomalous source that effectively includes any physics not included in the model used here, such as cross-field transport, particle drifts or turbulence. The anomalous source is defined as a function of s by the user and the coefficients calculated by the OSM solver, in this case it is set to the simplest case of a constant along s. This approach allows each flux tube to be treated independently, there is no perpendicular transport, either diffusive, advective

or turbulent, between two neighbouring tubes.

5.1.2 EIRENE

The EIRENE code is widely used in the fusion community to simulate the behaviour and plasma interaction of neutral particles and radiation in tokamaks. The plasma solution produced by OSM is dependent on the interaction of the plasma with neutrals and conversely the neutral population is dependent on the plasma solution. The neutral particles are not confined by the magnetic fields present in the tokamak and therefore interact with all regions of the SOL. This results in particle, energy and momentum sources over a large extent of the plasma. EIRENE uses the plasma solution calculated by OSM to calculate the neutral solution and returns this to OSM. This process is then repeated until a steady state solution is reached, although in practice this is often achieved after just a few iterations. Although EIRENE has 3D capability only a 2D solution is required when used with OSM.

5.1.3 DIVIMP

Although DIVIMP is essentially a stand alone code the version used here controls the running of OSM and EIRENE and the creation of the background plasma solution. The process of obtaining simulations of impurity behaviour begins with the simulation of the background plasma, which is usually first calculated without impurities. This solution is then saved to file and used by DIVIMP when simulating the impurity behaviour. Impurities are injected at a location defined by the user, the impurities are then followed using a Monte-Carlo method until a steady state is reached. It is possible to set a maximum dwell time for the particles launched by DIVIMP so that after a set time they are not followed and remain in the position they occupied after

the dwell time is reached. This allows a time dependent process, such as the injection of impurities, to be simulated up to the time that the injection ceases. DIVIMP uses the the ADAS atomic and molecular database [163] for all atomic processes.

Parallel transport is modelled by calculating the forces on the impurity particles from equation 1.11 as well as parallel diffusion. DIVIMP includes several different options for applying these forces, the setup used in this case is now described.

The first term in equation 1.11, the force due to the electric field does not need elaboration. The stopping time (τ_s) in the friction term is given by

$$\tau_s = m_i T_b \sqrt{\frac{T_b}{m_b}} \times \frac{1.0}{\left(6.8 \times 10^4 \left(1.0 + \frac{m_b}{m_i}\right) N_b Z_b^2 Z_i^2 \lambda\right)} \tag{5.3}$$

where the subscript b refers to values for the background plasma and λ is the mean free path for the impurity ions. The electron and ion temperature gradient force coefficients α_e and β_i are given by

$$\alpha_e = 0.71 Z_i^2, \beta_i = -3\frac{\left(1 - \mu - 5Z_i^2 \mu\sqrt{2\mu}\,(1.1\mu - 0.35)\right)}{(2.6 - 2\mu + 5.4\mu^2)} \tag{5.4}$$

where

$$\mu = \frac{m_i}{m_i + m_b} \tag{5.5}$$

the calculation of collisional diffusive transport uses a parallel time constant ($\tau_\parallel$) given by

$$\tau_\parallel = m_i \sqrt{\frac{T_b}{m_b}} \times \frac{T_i}{\left(6.8 \times 10^4 \left(1.0 + \frac{m_b}{m_i}\right) N_b Z_b^2 Z_i^2 \lambda\right)} \tag{5.6}$$

Perpendicular transport is included by setting a perpendicular diffusion coefficient $D_\perp$ to an empirical value, in this case the commonly adopted value

of $1m^2s^{-1}$ [164]. No terms for advective transport exist in DIVIMP. Particle drifts that can result in cross field transport are also not present, as stated in section 1.4.7.

5.2 Plasma solution

Obtaining a reliable plasma solution from OSM relies heavily on having detailed diagnostic data for the plasma to be simulated. The solution is based on 2 sets of observations, those from plasma diagnostics providing temperature, density and other kinetic information and observations that provide the magnetic grid on which the simulation is run. As has been noted in section 1.5 the MAST tokamak has a comprehensive array of diagnostics that make it very suitable for simulation using OSM. The plasma diagnostic data used as input to these simulations is detailed in chapter 3. DIVIMP allows the plasma solution to be stored so that ions can be injected into the simulation without having to recalculate. For these cases a total of 4 OSM-EIRENE iterations were required to achieve a steady state, at which point no significant change is seen with further iterations.

5.2.1 Simulation Equilibrium

The grids that define the geometry of the simulations were initially obtained from eqdsk files produced by the EFIT code, the lower divertor sections of these grids can be seen in figure 5.1.

A simple check on the validity of the calculated equilibrium can be made by comparing the strike point location given by the reconstruction with kinetic data from the divertor Langmuir probes. Figures 3.7, 3.8 and 3.9 show the EFIT calculated strike point position, divertor Langmuir probe density

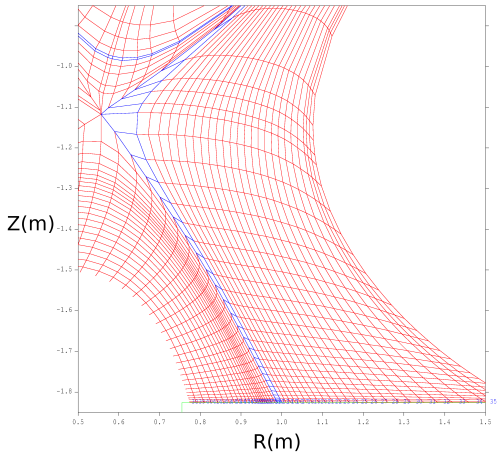

(a) 29125

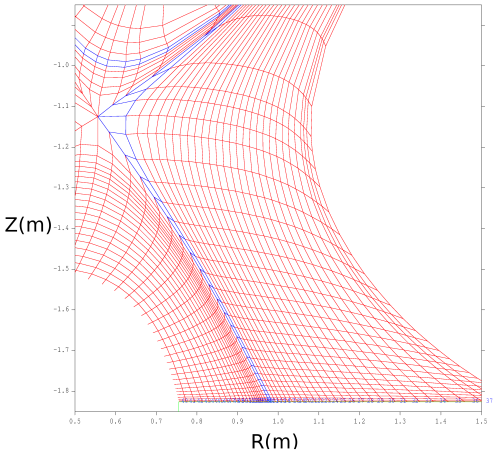

(b) 29126

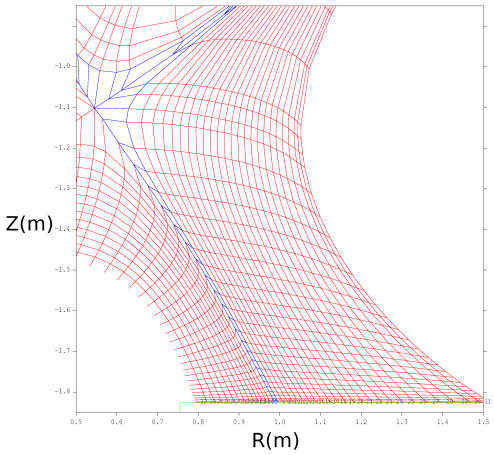

(c) 29139

Figure 5.1: Grids used for the impurity injection simulation. These are produced using EFIT magnetic equilibrium reconstruction.

data and injector Langmuir probe data for shots 29125, 29126 and 29139. It is expected that the density maximum be close to the strike point location, which is the case for the shots 29125 and 29126, however for shot 29125 this data is contradicted by the injector mounted Langmuir probe, which suggests that the the strike point may have already passed over the injector. This is consistent with the imaging of injection for 29125, which suggests that the injection took place inside the outer strikepoint. For shot 29139 the Langmuir probe data suggests that the strike point location calculated by EFIT is inboard of the actual location, the density peak is significantly inside the calculated strikepoint and there is no increase in saturation current seen on the injector Langmuir probe at the time of the shot, which would be expected as the strike point passes over the probe. In order to account for the clear discrepancy in the strike point position identified by EFIT the injection location used in the simulation was altered to account for this: this is described in sections 5.3.1 and 5.5.2.

5.2.2 Background plasma simulation

The plasma solutions for the lower divertor used for the simulations of impurity injection can be seen in figures 5.2, 5.3 and 5.4. As described in section 1.4.5 these simulations are base on the magnetic equilibrium reconstruction and experimental data. The standard approach is to use measured data at the targets and midplane. In this case this data is provided by divertor Langmuir probes (see section 3.2.4) and the MAST Thomson scattering system (see section 3.2.4).

Uncertainties in data location

As stated in the previous section there is significant uncertainty in the magnetic equilibrium used, which translates into an error in the radial location of the target and midplane data used in the simulation. A sensitivity scan was carried out to address this issue, background plasma simulations were carried out while independently shifting the location of the midplane and target data by 0.01 and 0.02 in normalised poloidal flux (ψ_n) in each direction, equivalent to approximately $7mm$ and $14mm$ at the outer divertor target and $3mm$ and $6mm$ at the midplane. This results in 8 further plasma solutions with either the midplane or target data shifted. Simulations of impurity injection were then carried out using a dwell time of $50\mu s$ and the result compared for the 5 background plasmas. The results of this scan can be in figures 5.5 and 5.6.

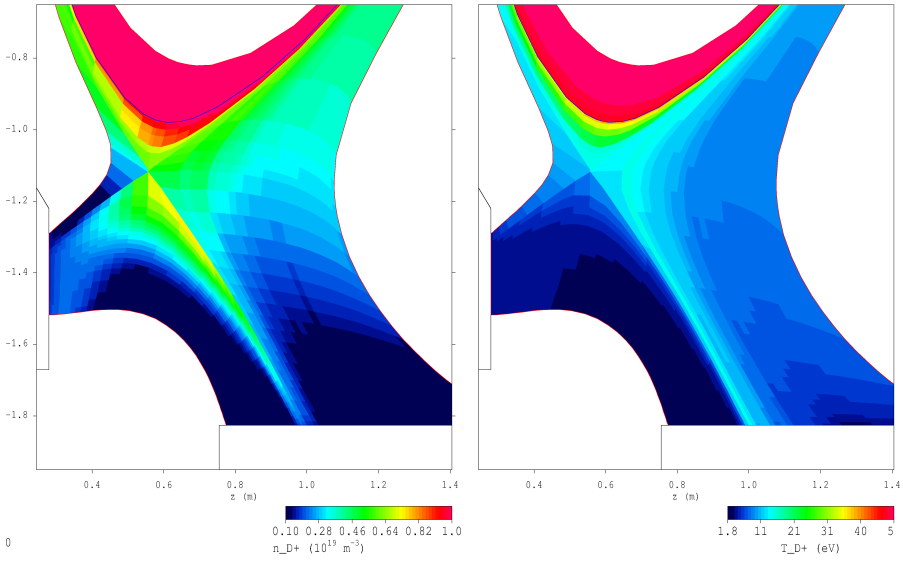

Figure 5.2: Simulated deuterium density and temperature for shot 29125 at 250ms

A shift of $\psi_n = 0.01$ has only a small effect on the carbon II emission. The effect on the carbon III emission is significant for changes in the target data

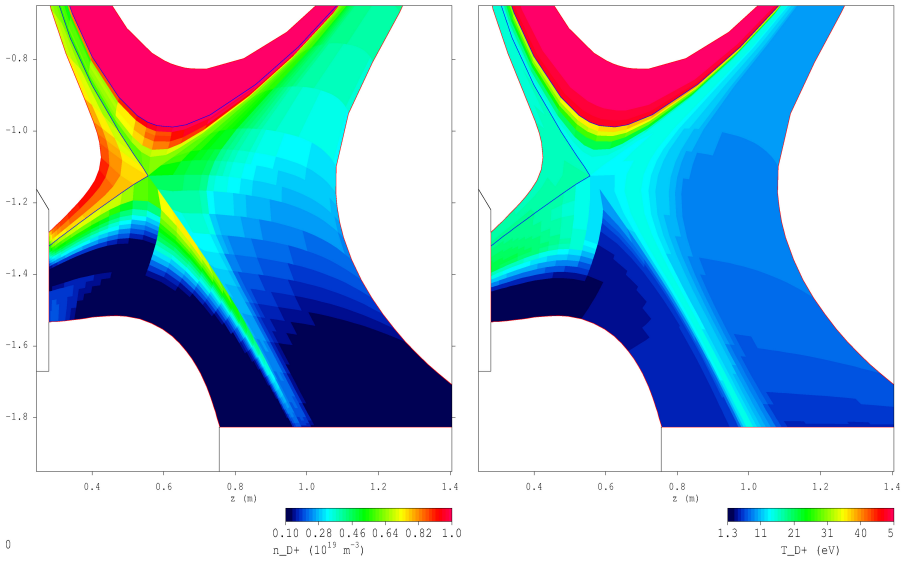

Figure 5.3: Simulated deuterium density and temperature for shot 29126 at 240ms

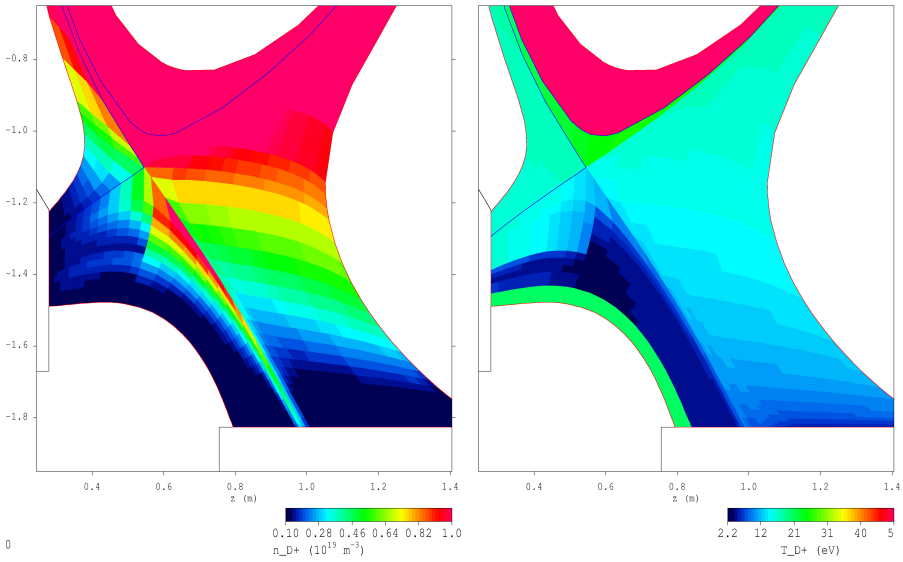

Figure 5.4: Simulated deuterium density and temperature for shot 29139 at 320ms

for the L-mode cases and the midplane data in the H-mode case. For the L-mode cases this is likely due to the change in temperature caused by the shift, resulting in less carbon reaching the second ionisation state. In the case of the H-mode data this reflects the large gradient in midplane temperature and density.

A shift of $\psi_n = 0.02$ has a relatively small effect on the L-mode shot 29125, probably because the injection point is well above the targets. For L-mode shot 29126 and H-mode shot 29139 this level of shift has a dramatic effect on the simulation result, in particular for midplane data.

The effect on the parallel density of shifting the input data can be seen in figure 5.7. It can be seen that the density profile changes significantly with shifts in the input data, and helps to explain the differences seen in emission from simulation.

Similarity between the L-mode shots

Shots 29125 and 29126 are naturally very similar, the only systematic difference being the strike point position. This is born out by a comparison of the parallel density for the tubes just outside the strikepoint, in this case 12 and 13, which can be seen in figure 5.8. The data for tube 13 can be taken as identical as expected, there is however a difference in the gradient for tube 12, which is closer to the strikepoint. This is due to differences in the midplane data, and is small enough to be unlikely to have a significant effect on the impurity simulations.

5.2.3 Flow comparisons

The coherence imaging data allowed direct comparison of the simulated background plasma to the data. Figure 5.9 shows the measured flow compared

against the simulated flow along one of the simulation flux tubes. It can be seen that the measured flow profiles are largely flat in the lower divertor and are unlike the simulated profiles which show almost zero flow along most of the flux tube and large increase in flow towards the divertor close to the outer target. The measured flow velocities are also significantly different from simulation. It should be noted that the lack of carbon III emission close to the targets increases the error on this measurement and in the case of shot 29139 the measured flow close to $0ms^{-1}$ near the targets is not reliable. This casts some doubt on the validity of the OSM background plasma simulation and further work is required to account for this difference.

5.3 Simulated impurity injection initial conditions

There are several uncertainties associated with the injection conditions used in the DIVIMP simulations. the principle of these are listed below.

- Initial radial position of ions relative to the outer strike point
- Initial Z position of ions
- Duration of injection
- Energy distribution of injected ions
- Number of injected ions

For each uncertainty an estimate was made from the available data. These values were then used for the baseline simulations. Scans of these values were then performed to identify the possible effect of the uncertainties.

5.3.1 Initial radial position of injected impurity

The absolute radial position of the injected ions is known due to the fixed location of the DSF at 0.985m. There is some uncertainty in this position due to the possibility of the spark forming at a particular location on the ring shaped gap of the injector head (see 2.4.1) instead of uniformly around the ring. However, as the inner diameter of the outer electrode is only 2mm any error introduced by this possibility is small. The radial position of the injection relative to the outer strike point is harder to identify, largely due to uncertainties in the magnetic reconstruction. Assuming the true location of the injector then this distance is set by the simulation grid that is based on the magnetic equilibrium. Unfortunately there is a large discrepancy between the EFIT strike point data and that inferred from Langmuir probe measurements (see section 3.2.3). This discrepancy can be somewhat accounted for by moving the injection location radially in the simulation. Simulations with injection performed at different radial locations are discussed in section 5.5.2

5.3.2 Initial Z position

Identifying the vertical or Z location of the injected ions relies on the interpretation of the filtered images (see section 4.3. This uncertainty arises as the carbon injector launches carbon neutrals and ions vertically into the tokamak. This can result in a vertical displacement of the carbon before interaction with the plasma dominates their motion. This is made more difficult by the 2D projection of the 3D plume and by the mix of ions, atoms and fine dust particles launched by the injector. Ablated ions will be confined by the toroidal magnetic field so one can be confident that the injection location for ions is close to the centre of the DSF. The images and field line

projections for shots 29126 and 29139 support this with the most significant emission in the first frame after injection coming from close to the DSF location, although in shot 29126 there is significant spread in the image. Neutral carbon particles can however travel away from the injection location until they are ionised by the background plasma. The image from 29125 suggests that this does occur as the emission peak appears some centimetres above the DSF location. For the purposes of simulation the baseline injection location for shots 29126 and 29139 was taken to be 1mm above the DSF while for shot 29125 it was taken to be 4.5cm above the DSF.

5.3.3 Injection duration

Measurements of the discharge current and the peak in visible emission give injection durations of approximately $40\mu s$ for the L-mode cases and $60\mu s$ for the H-mode cases, see section 3.2.2. Although there is significant uncertainty in these values it is reasonable to assume that the injection does in fact take place over the duration of the imaging for purposes of comparison with simulation.

5.3.4 Initial energy distribution

DIVIMP assigns the same energy to all injected ions, there is no possibility of assigning an energy distribution function in a single simulation, although this can be approximated by performing multiple simulations with different energies and total number of injected ions and then combining the results, this was not done here. No measurements of ion energy were made during the development of the injector, and even if this was the case the markedly different conditions present on MAST would cast doubt on the applicability

of the measurements. It is therefore necessary to make an estimate of the initial ion energy based on the available information.

The transit time of a carbon ion between the electrodes is of the order of nanoseconds, significantly longer than the microsecond timescale of the discharge itself. This means that individual carbon ions will gain a large proportion of the energy available from the electric field, potentially hundreds of electron-volts. However these ions will then impact on the positive electrode, knocking further atoms and ions from the electrodes, losing energy to the wall and ablated products in the process. Further ionisation of the ion is also likely to occur at these energies, further reducing the kinetic energy of the ion. These processes are extremely complex and a detailed analysis is beyond the scope of this thesis. However this process is very similar to the sputtering of atoms from the first wall of fusion devices. Much research has gone into this process and a brief discussion is available from Stangeby [5]. This works approximates the energy distribution of physically sputtered neutrals as

$$\frac{dY}{dE_Z} = \frac{E_Z}{(E_Z + E_B)^3} \tag{5.7}$$

where Y is the sputtering yield, E_Z the energy of the emitted neutral and E_B the binding energy of carbon. This distribution has a maximum at $E_Z = 1/2E_B$, for carbon $E_B = 7.4eV$. Although this treatment applies to neutrals it is not unreasonable to expect carbon ions to have similar energies in the $1eV$ to $10eV$ range.

The operation of the carbon injector can also be compared to the recent developments in vacuum arc plasmas, on which a significant body of work exists [165–167]. As part of this work measurements have been made of the ion energy distribution produced by these devices. Byon 2003 [168] produced

energy distribution functions for carbon plasmas, the result being a peaked distribution with a high energy tail centred around $50eV$ - although higher than values estimated from sputtering arguments, this is consistent with ion energies in the $10eV$ range.

Although there is still large uncertainty in the initial energy of the injected ions these arguments suggest $10eV$ as an appropriate initial condition and this is used in the basic comparison with experiment.

Effect of injected energy

In order to understand the effect of ion energy on transport a scan in injected energy was performed for the three shots of interest. Ions were injected into the plasma with energies of 0.1eV, 1eV, 10eV and 100eV. The rate of transport parallel to the field for the carbon II and carbon III states was then compared for each energy. The results can be seen in figures 5.10, 5.11 and 5.12. The solid, dashed and dotted lines represent injection at 1eV, 0.1eV and 10eV while the triangles represent injection at 100eV. It can be seen that the initial energy has a very significant impact on the impurity transport. This is not surprising as the background plasma temperature is approximately 10eV, once the initial energy is comparable to this value then the pressure term in equation 1.11 becomes increasingly important.

5.3.5 Number of injected ions

The Monte Carlo method used by DIVIMP does not affect the background plasma solution, the number of injected ions is therefore only relevant when considering the statistical fluctuations in the solution. A higher number of injected ions gives a result with lower statistical error at the expense of computational resources. For the simulations described here 10000 particles

were injected, giving run times of the order of minutes.

5.4 Parallel transport simulations for comparison with experiment

In order to compare simulation with experiment DIVIMP was set up to output the carbon II and carbon III emission along the flux tubes near to the injection location. For the three shots 29125, 29126 and 29139, figures 5.13, 5.15 and 5.15 show the simulated carbon II and carbon III emission along 3 flux tubes, 1 inside the outer strike point and 2 outside. 6 successive times separated by $13.3\mu s$ are shown in each frame, the radial location of the centre of the flux tube at the divertor target is shown above each frame. The injection location is at the DSF location of $0.985m$ and the initial ion energy is $10eV$. The height of injection for shot 29125 is 4.5cm above the target and for 29126 and 29139 it is 1mm above the target.

5.5 Comparison between experiment and simulation

Presented here are comparisons between the simulated impurity emission along a field line corresponding to the experimentally measured emission taken from the projection of the field lines onto the images taken by the fast filtered cameras. An immediately obvious problem is the 3 dimensional nature of the emission compared to the 2 dimensional images, which takes a line of sight integrated measurement at each pixel. This problem is somewhat alleviated by the preferential transport along the field lines. For the H-mode

shot 29139 the emission can clearly be seen to follow the field line with little cross-field transport occurring over the period of the images. This is not the case for the 2 L-mode shots 29125 and 29126 where clear cross field transport is observed. However strong parallel transport is still present with the plume extending significantly along the field lines, particularly for shot 29126. The diffuse nature of the emission in shot 29125 is likely due to the injection location, which appears to have occurred radially inside the outer strike point. The diffuse nature may then be partly due to neutral particles being injected upwards in an expanding cloud and ionising once they reach the hotter denser region close to the separatrix, in a manner more akin to gas injection.

Figures 5.16, 5.17 and 5.18 show the experimentally measured carbon II emission plotted against the simulated carbon II emission for the flux tube with the highest emission in each case for the 2 L-mode and 1 H-mode shot. The initial conditions are the same as the plots presented in section 5.4 and an arbitrary normalisation factor has been applied to the simulated emission of 16 in the case of comparison with sector 1 data and 128 in the case of comparison with sector 11 data. No comparison is made with carbon III data due to the lack of observed emission.

5.5.1 Lack of observed CIII emission

As has been noted in section 4.3.2 very little or no extended emission was seen when using carbon III filters. Looking at the ratio of carbon II to carbon III emission from simulation one can see that the carbon III emission is at least a factor 10 below the carbon II emission. The maximum observed carbon III emission is approximately $5Wsr^{-1}m{-}2$ from sector 11 shot 29142, while the maximum observed carbon II emission is approximately $10Wsr^{-1}m{-}2$.

However this is found at the injection location and the large peak in emission seen in experiment is not seen in simulation, suggesting that this level of emission is at least partly due to the arc discharge itself. Looking at the carbon II images (figure 4.8) one can see that the intensity in the plume away from the injection location is typically $0.5Wsr^{-1}m{-}2$, assuming a ratio of 10:1 between the carbon II and carbon III emission the carbon II emission would be of the order $5 \times 10^{-2}Wsr^{-1}m{-}2$, only just above the noise level of $3 \times 10^{-2}Wsr^{-1}m{-}2$. The most likely reason for a lack of observed emission is therefore a lack of sensitivity of the filtered cameras.

5.5.2 Effect of radial location on emission

In order to account for the errors in strike point location calculated by EFIT runs were performed for shots 29125 and 29139 with the injection location moved by $1cm$ and $2cm$. This changes the tube within which the highest emission occurs and so changes the tube used for comparison. For shot 29125 the adjustment was made inwards towards the high field side, increasing the distance of the injection inside the outer strike point, this can be seen in figure 5.19. For shot 29139 the calculated strike point was clearly outside the true location, $1cm$ and $2cm$ adjustments were therefore made towards the low field side and can be seen in figure 5.20. Only plots for sector 1 are shown.

5.5.3 Relative contribution of the transport mechanisms

As described in sections 1.2.3 and 5.1.3 there are several mechanisms responsible for the transport of impurities, either corresponding to a term in

equation 1.11 or added to account for unknown physics as in the case of the cross-field diffusion coefficient. To better understand the importance of each mechanism in these simulations a series of simulations were carried out with the relevant term suppressed. The simulations were run with a dwell time of $50\mu s$ and the results can be seen in figure 5.21.

In each case the left panel shows the suppression of forces due to the temperature gradient, friction and electric field, it can be seen that for 29125 these do not have a significant effect on the result. For 29126 the temperature gradient has little effect although the forces due to the electric field and friction do have a small but noticeable effect, this is likely due to the high flow and electric fields close to the target. For the H-mode 29139 only the frictional force has a significant effect. The middle panel shows simulations run without collisions and with the cross-field diffusion set to 0. Switching off collisions, which has the effect of suppressing diffusion, has the effect of increasing the parallel transport. Switching off the cross-field diffusion increases the emission for this tube, this is expected as more particles remain in the tube into which the injection occurred. The right panel shows impurities injected with 0 energy, this appears to be the most significant factor in determining transport, and also explains why turning off collisions increases the parallel transport by such an extent.

5.6 Role of drift terms in simulation results

It has previously been stated that neither DIVIMP or OSM simulations include drift terms arising from electric field and magnetic field gradients. Recent research has focused on the impact of particle drifts on impurity transport[133] and divertor plasma conditions[96, 112, 169] and has shown

these terms to be important in accurately representing carbon deposition and target power loads. How important these terms are with regards to the parallel impurity transport, which governs the influx of impurities sputtered from the target into the bulk plasma is less clear.

5.6.1 Effect of drift terms on background plasma solution

Particle drifts can have a variety of effects on the background plasma conditions, which will then affect the transport of impurities. It has been shown[112, 170] that $\mathbf{E} \times \mathbf{B}$ and diamagnetic drifts cause a broadening of the outer target radial profile and a reduction in peak density and power reaching the target. However this effect is implicitly included in the OSM modelling approach through the anomalous source terms and the prescription of target profiles from experimental data. Effects of drifts on the plasma profiles along $\mathbf{B}$ are however not included using this method. In particular the parallel flow appears to be significantly affected by drifts [112, 171], with simulations on JT-60[169] showing mid-plane flow velocities increasing from $2.5kms^{-1}$ to $8.3kms^{-1}$ when drift velocities are included. This is strongly supported by data from the coherence imaging diagnostic used in these experiments (section 5.2.3), which shows a significantly higher flow velocity than seen from simulation along most of the flux tube. The effect of increased flow is to increase the force on the impurity ions due to friction and for the 2 cases with injection close to the target, L-mode shot 29126 and H-mode shot 29139, this term is seen to be significant (section 5.5.3). The simulated flow close to the targets is actually larger than the measured flow, so that the significance of the friction term may be doubted, while further away from the targets as in shot 29125, where the frictional force appears less significant,

the opposite is true. It can therefore be inferred that the simulated flow has a significant impact on the validity of the impurity transport simulations.

5.6.2 Direct impact of drift terms on plume evolution

The effect of $\mathbf{E} \times \mathbf{B}$ drifts on injected impurity plumes has previously been observed by imaging of the plume distortion[51] and also by measuring the location of deposited carbon-13[133] from post-mortem analysis of divertor tiles. For standard magnetic field direction ($\nabla\mathbf{B}$ drift towards the lower divertor) radial electric fields in the divertor SOL caused by radial temperature gradients result in a poloidal drift towards the outer target, while electric fields parallel to the magnetic field caused by parallel temperature gradients cause an inward radial drift towards the private flux region. Electric fields in the magnetic presheath to the sheath can also cause radial drifts, however identification of this effect in the plumes studied here is not possible as it occurs within approximately $1mm$ of the targets and can only be inferred using post-mortem analysis techniques and detailed modelling[133].

The extremely diffuse nature of the plume in shot 29125 means that any distortion is obscured, however for shots 29126 and 29139 the plume closely follows the field lines towards the X-point. The orientation of the sector 1 camera means that the radial and poloidal drifts work in approximately opposite directions in the image plane and partially cancel out the observed distortion. The sector 11 camera suffers less from this problem as the radial drifts are largely normal to the image plane, while the poloidal drifts are largely vertical, the approximate directions are seen in figure 5.22. Comparing figure 5.22 a and b one can see an apparent distortion in the plume in the poloidal direction towards the targets that is more pronounced in the sector 11 image. This could be interpreted as the effect of a poloidal drift,

however errors in the magnetic equilibrium reconstruction and magnetic field projection due to the camera registration could cause a similar effect.

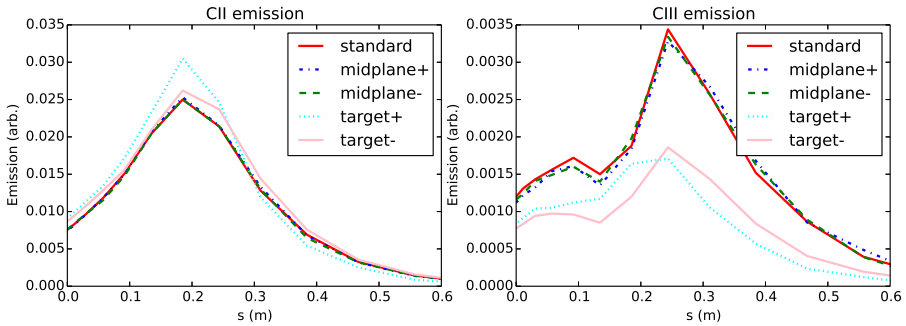

(a) 29125

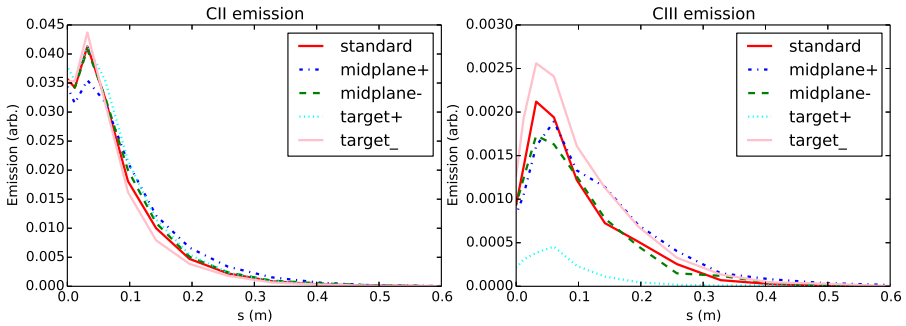

(b) 29126

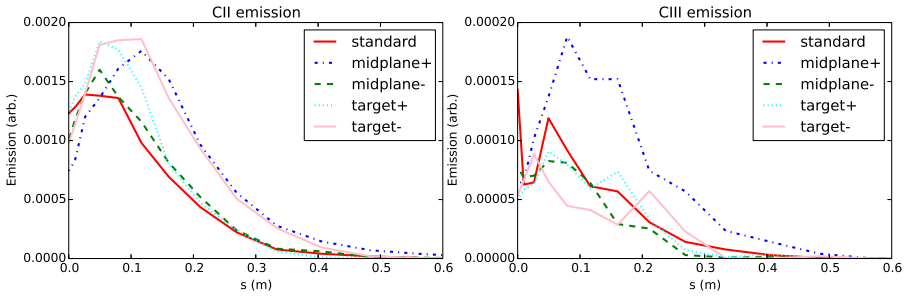

(c) 29139

Figure 5.5: Sensitivity scan using background plasma solutions with the target or midplane data shifted by $\psi_n \pm 0.01$. Each plot shows simulated carbon II and carbon III emission parallel to the magnetic field from the injection location. s is the parallel distance along the flux tube.

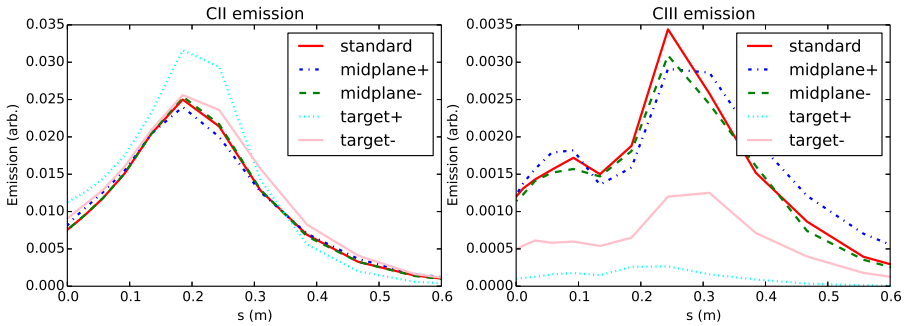

(a) 29125

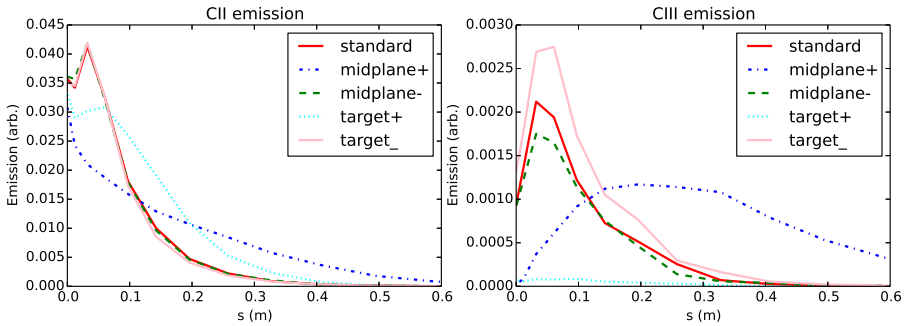

(b) 29126

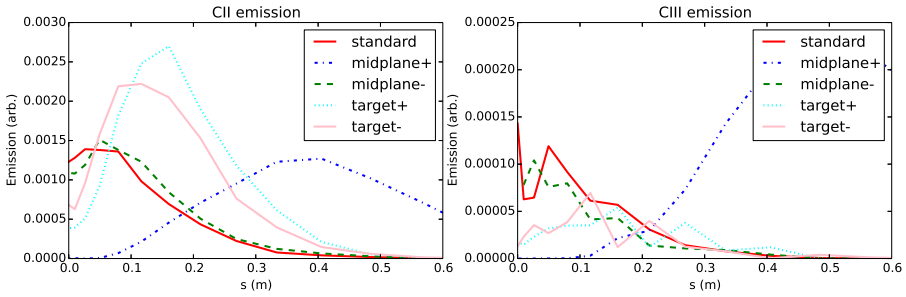

(c) 29139

Figure 5.6: Sensitivity scan using background plasma solutions with the target or midplane data shifted by $\psi_n \pm 0.02$. Each plot shows simulated carbon II and carbon III emission parallel to the magnetic field from the injection location. s is the parallel distance along the flux tube.

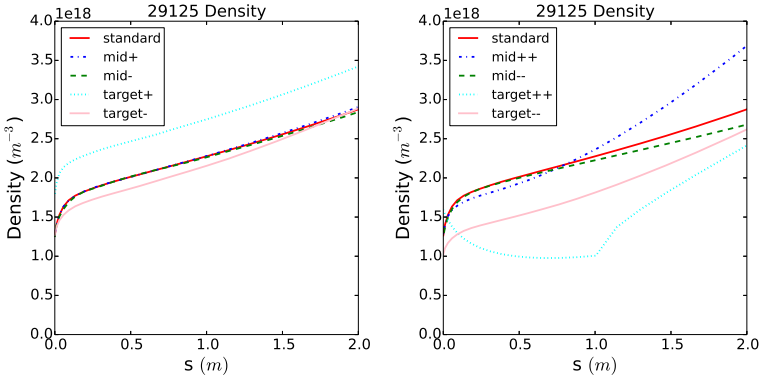

(a) 29125

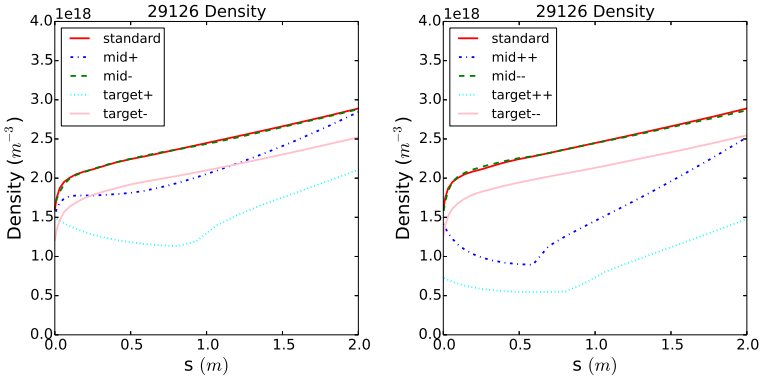

(b) 29126

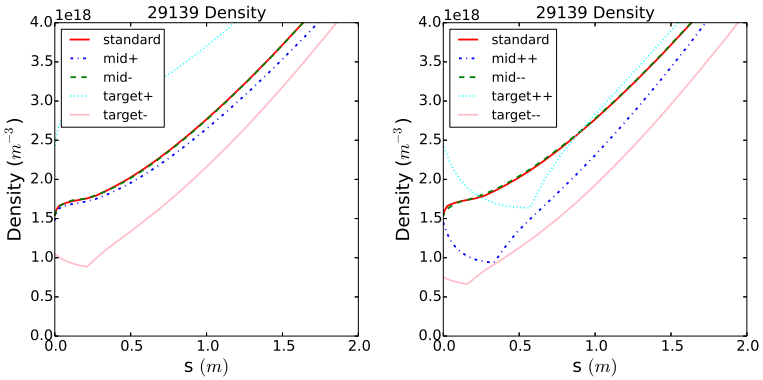

(c) 29139

Figure 5.7: Density along the magnetic field for the simulation tube where the injection takes place.

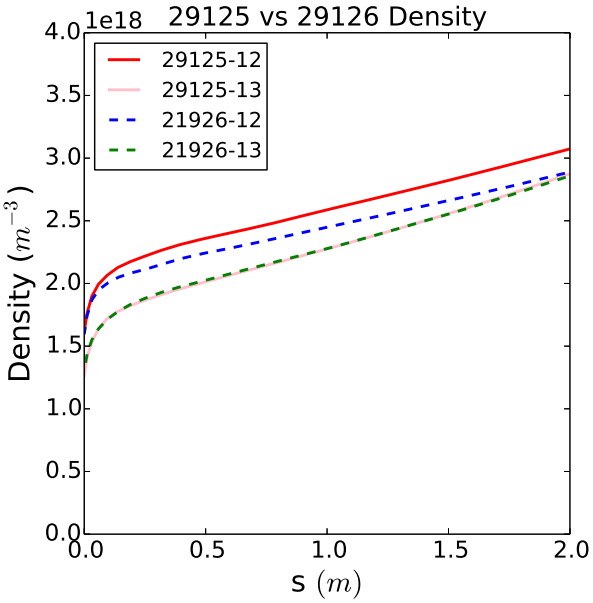

Figure 5.8: Density along the magnetic field for simulation tubes just outside the strike points for shots 29125 and 29126. The data for tube 13 can be taken as identical as expected, there is however a difference in the gradient for tube 12, which is closer to the strikepoint. This is due to differences in the midplane data, and is small enough to be unlikely to have a significant effect on the impurity simulations.

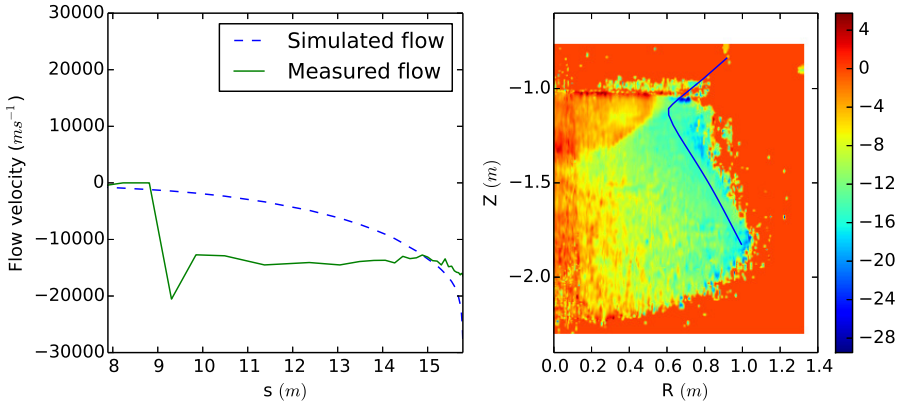

(a) 29125

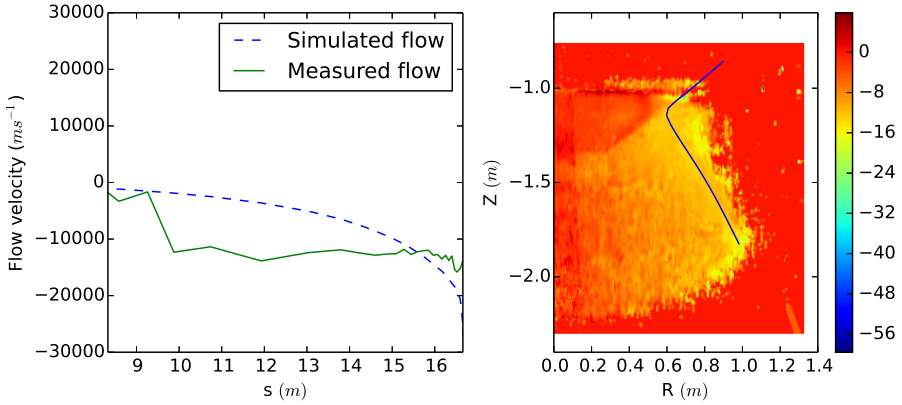

(b) 29126

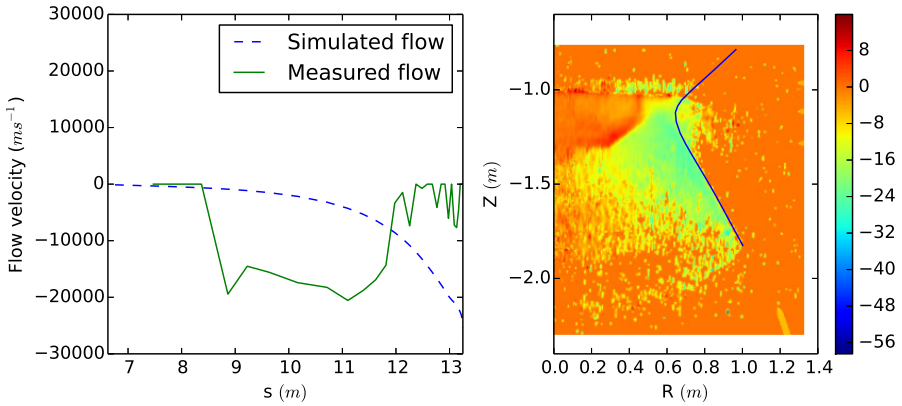

(c) 29139

Figure 5.9: Comparison of measured and simulated parallel flow using the coherence imaging diagnostic and carbon III emission lines, see section 1.3.1.

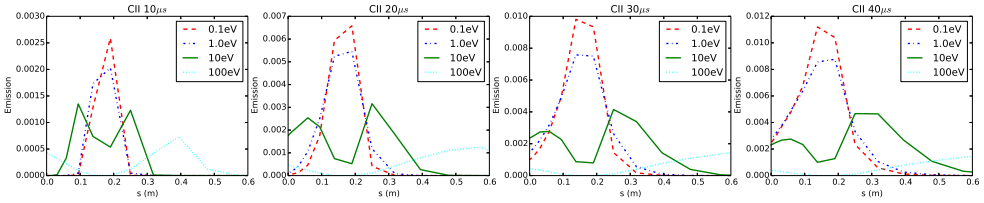

(a) CII emission

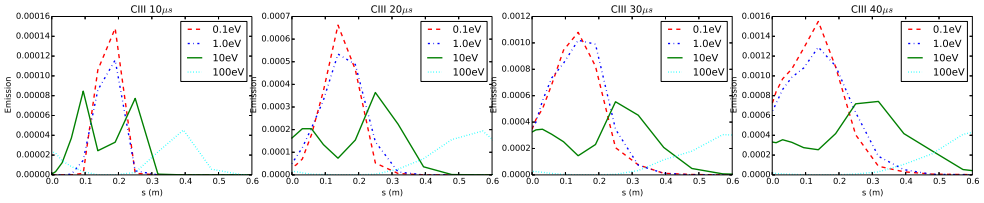

(b) CIII emission

Figure 5.10: Comparison of transport parallel to the magnetic field for CII and CIII ions injected at $0.1eV, 1eV$, $10eV$ and $100eV$ at $10\mu s, 20\mu s, 30\mu s$ and $40\mu s$ after injection for shot 29125. s is the distance along the magnetic field from the lower target.

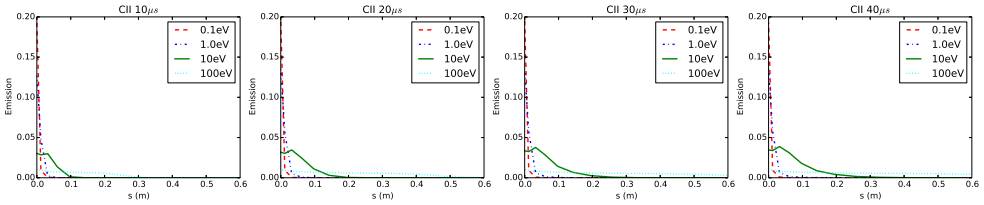

(a) CII emission

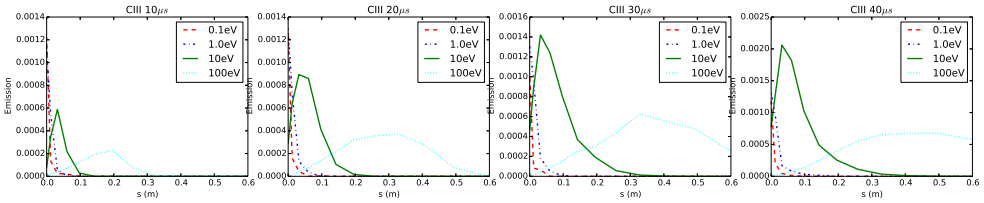

(b) CIII emission

Figure 5.11: Comparison of transport parallel to the magnetic field for CII and CIII ions injected at $0.1eV, 1eV$, $10eV$ and $100eV$ at $10\mu s, 20\mu s, 30\mu s$ and $40\mu s$ after injection for shot 29126. s is the distance along the magnetic field from the lower target.

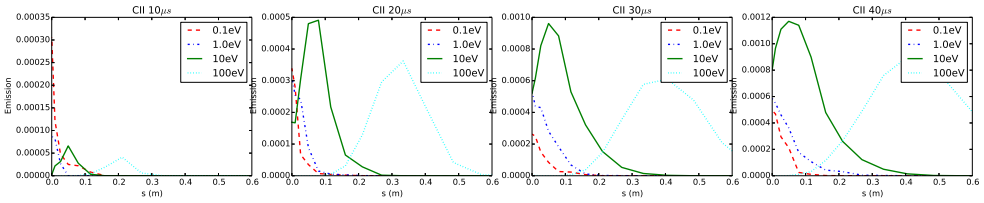

(a) CII emission

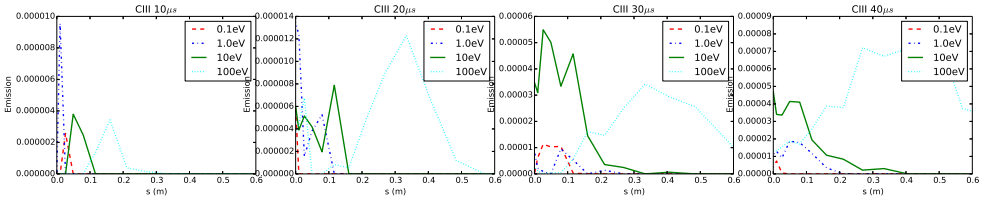

(b) CIII emission

Figure 5.12: Comparison of transport parallel to the magnetic field for CII and CIII ions injected at $0.1eV, 1eV$, $10eV$ and $100eV$ at $10\mu s, 20\mu s, 30\mu s$ and $40\mu s$ after injection for shot 29139. s is the distance along the magnetic field from the lower target.

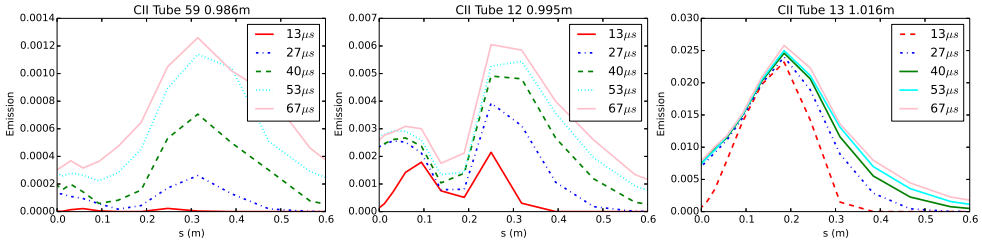

(a) CII emission

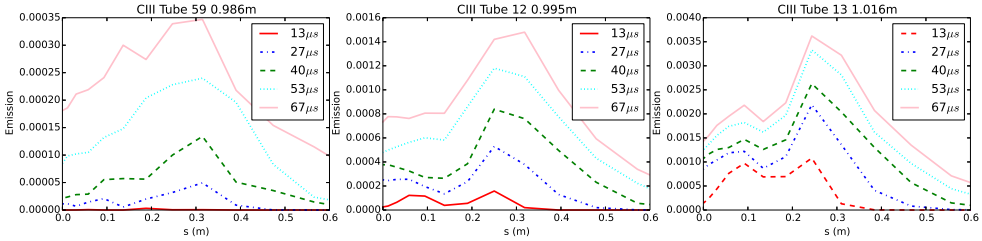

(b) CIII emission

Figure 5.13: Comparison of transport parallel to the magnetic field for CII (a) and CIII (b) ions injected into shot 29125. Each frame shows emission along a different flux tube starting at radial locations $0.986m$, $0.995m$ and $1.016m$. s is the distance along the magnetic field from the lower target.

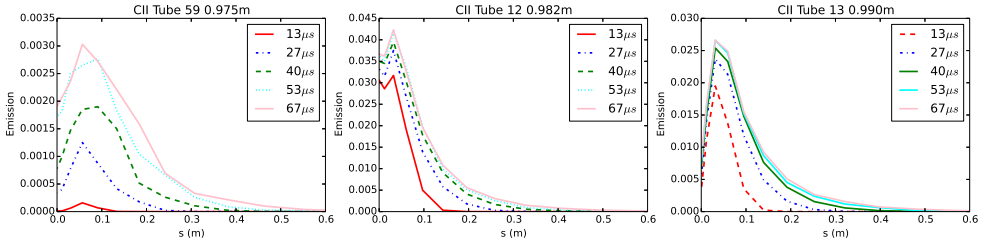

(a) CII emission

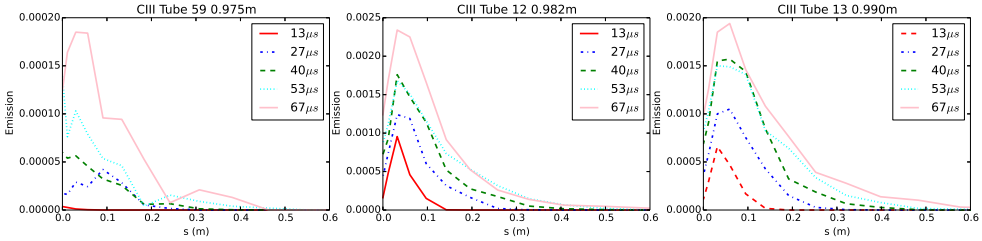

(b) CIII emission

Figure 5.14: Comparison of transport parallel to the magnetic field for CII (a) and CIII (b) ions injected into shot 29126. Each frame shows emission along a different flux tube starting at radial locations $0.975m$, $0.982m$ and $0.990m$. s is the distance along the magnetic field from the lower target.

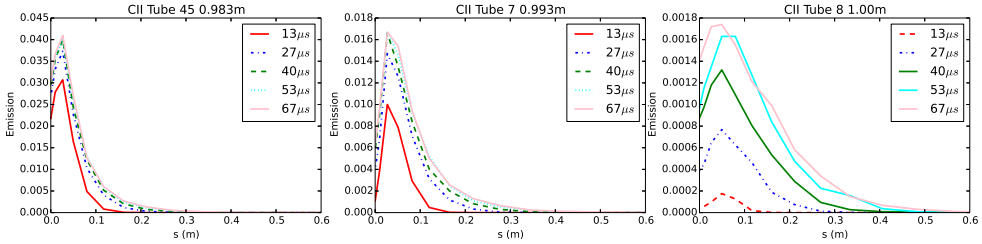

(a) CII emission

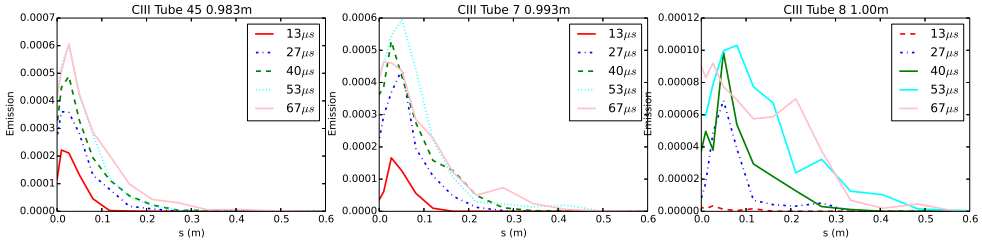

(b) CIII emission

Figure 5.15: Comparison of transport parallel to the magnetic field for CII (a) and CIII (b) ions injected into shot 29139. Each frame shows emission along a different flux tube starting at radial locations $0.983m$, $0.993m$ and $1.00m$. s is the distance along the magnetic field from the lower target.

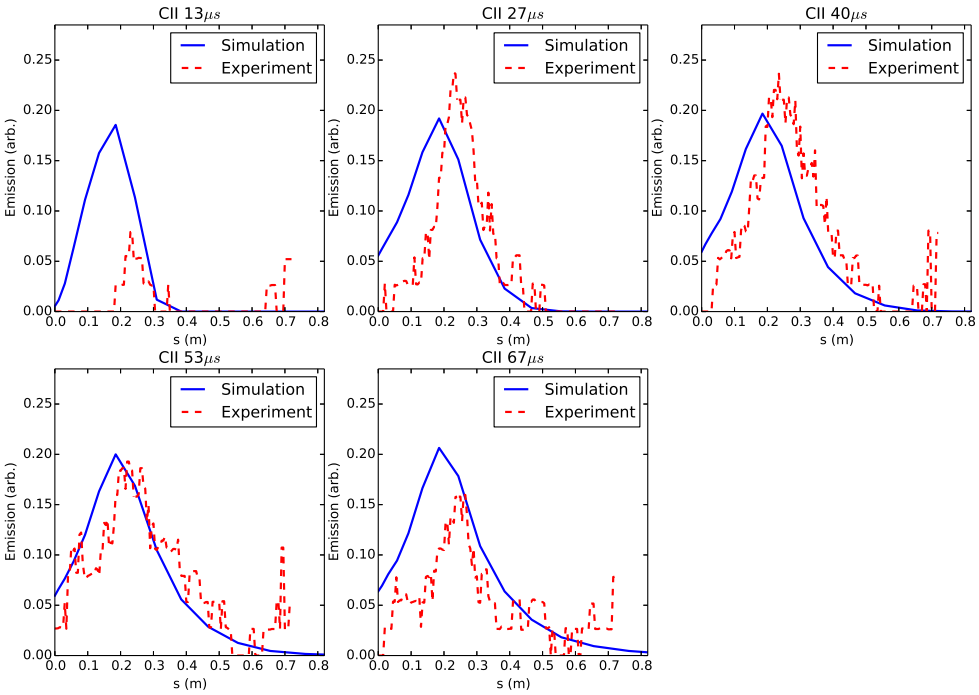

(a) Sector 1 emission

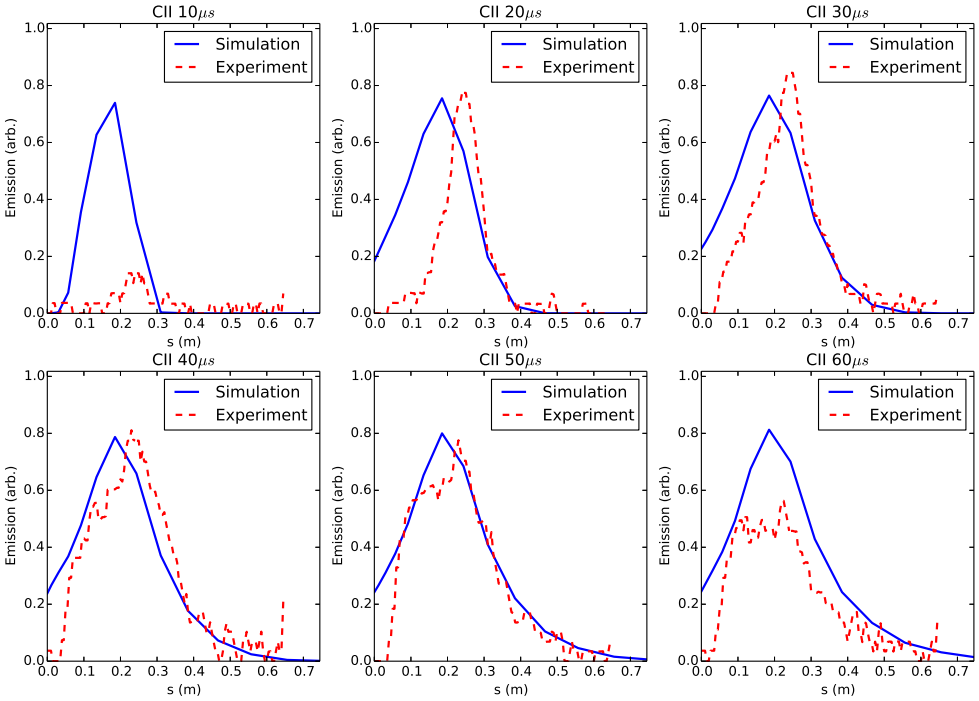

(b) Sector 11 emission

Figure 5.16: Comparison with experiment of transport parallel to the magnetic field for CII ions for L-mode shot 29125. s is the distance along the magnetic field from the lower target.

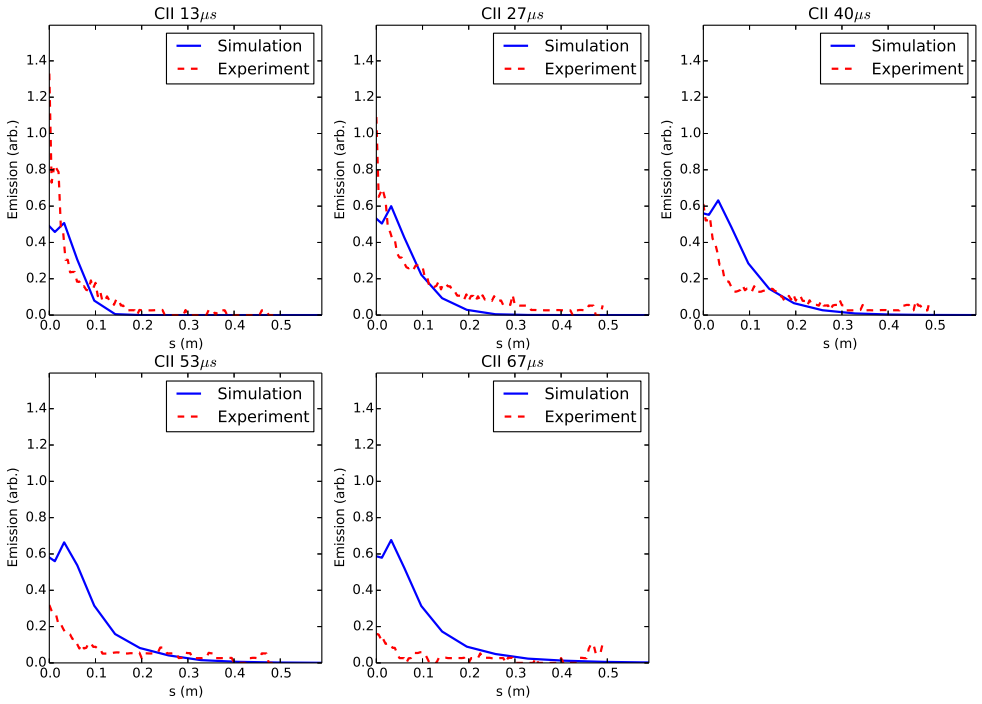

(a) Sector 1 emission

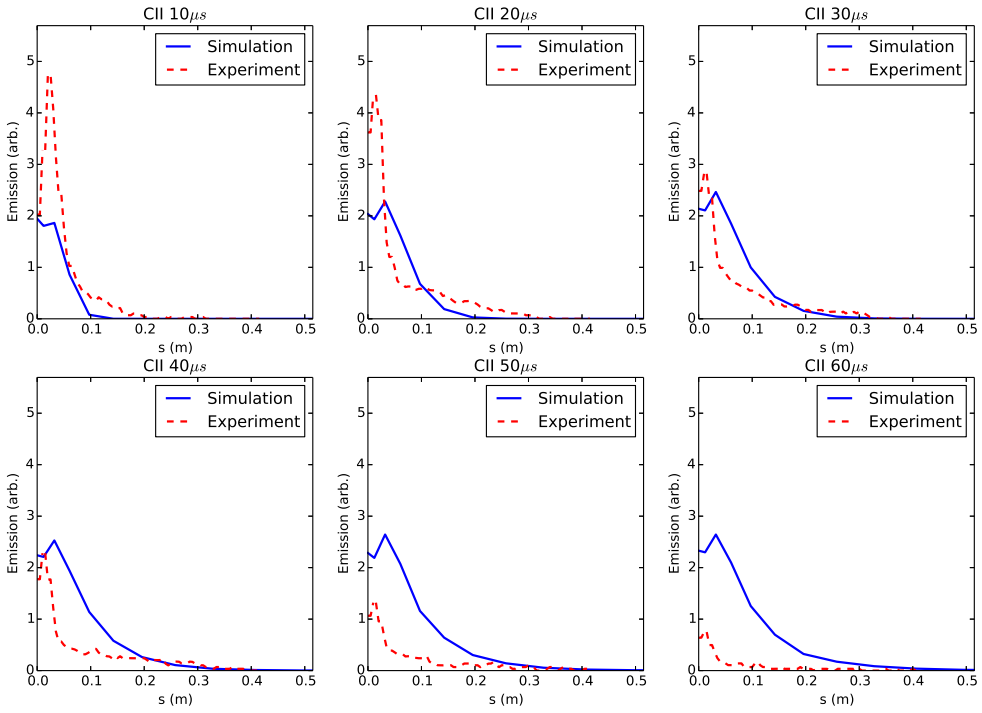

(b) Sector 11 emission

Figure 5.17: Comparison with experiment of transport parallel to the magnetic field for CII ions for L-mode shot 29126. s is the distance along the magnetic field from the lower target.

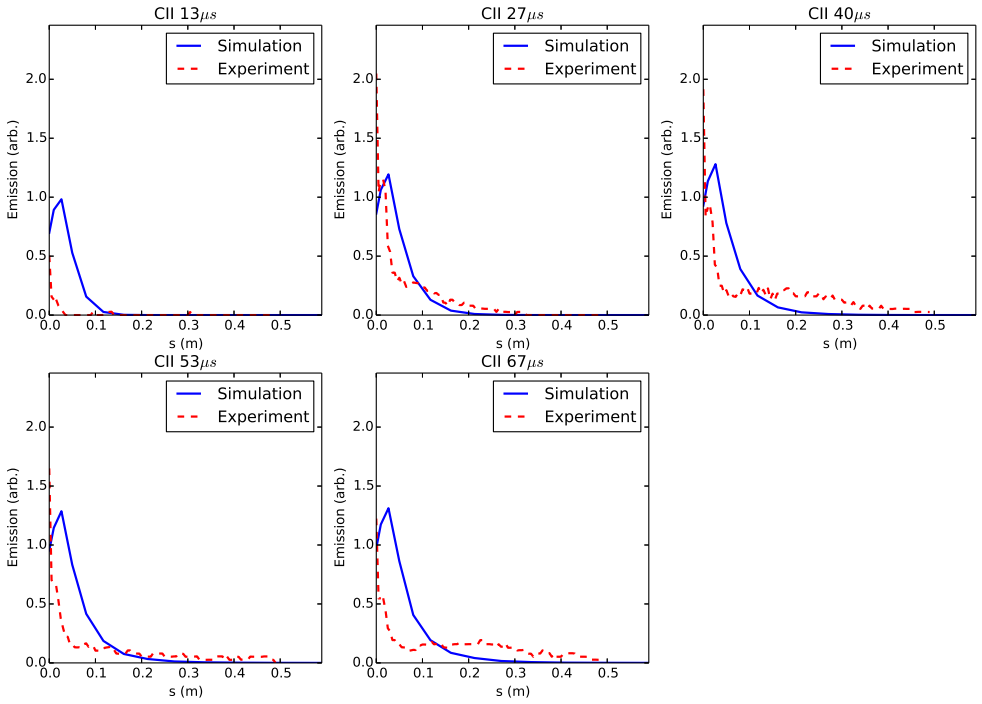

(a) Sector 1 emission

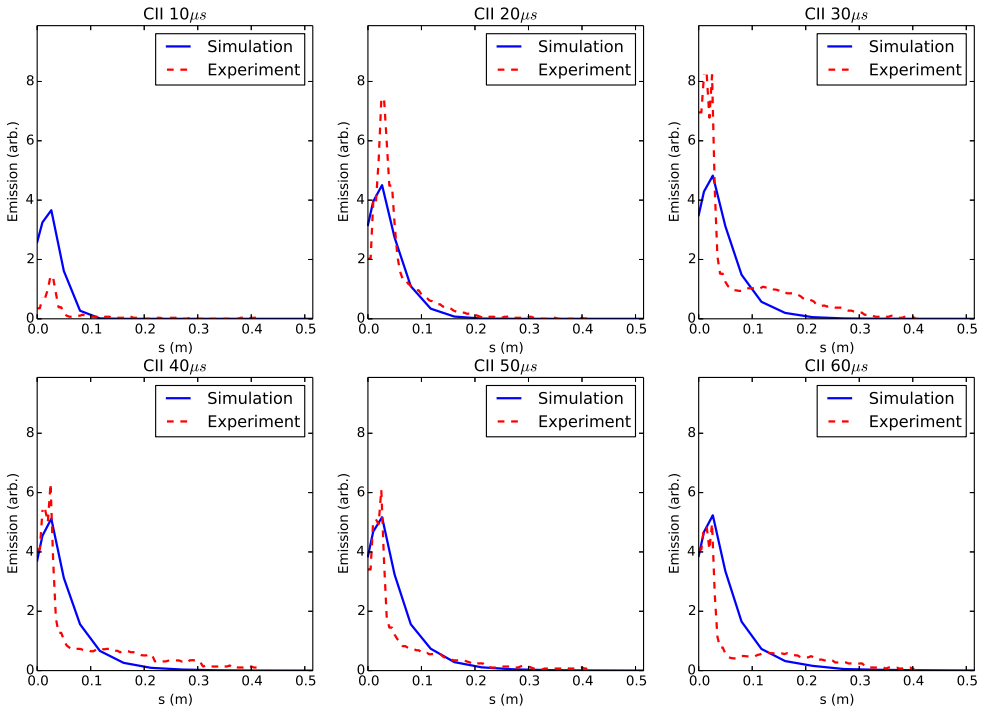

(b) Sector 11 emission

Figure 5.18: Comparison with experiment of transport parallel to the magnetic field for CII ions for H-mode shot 29139. s is the distance along the magnetic field from the lower target.

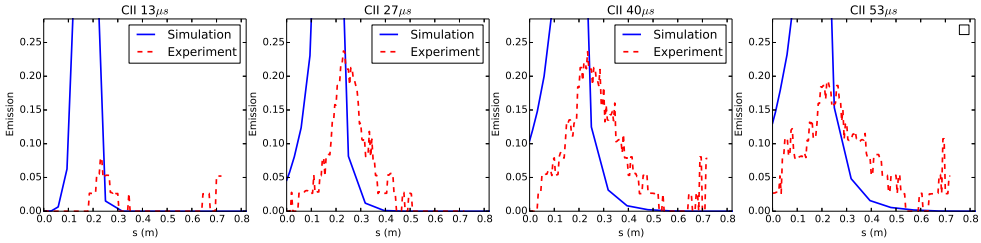

(a) 1cm shift

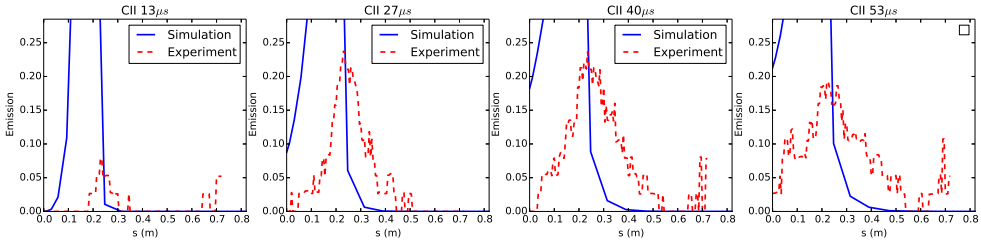

(b) 2cm shift

Figure 5.19: Comparison with experiment of transport parallel to the magnetic field for CII ions for L-mode shot 29125. s is the distance along the magnetic field from the lower target.

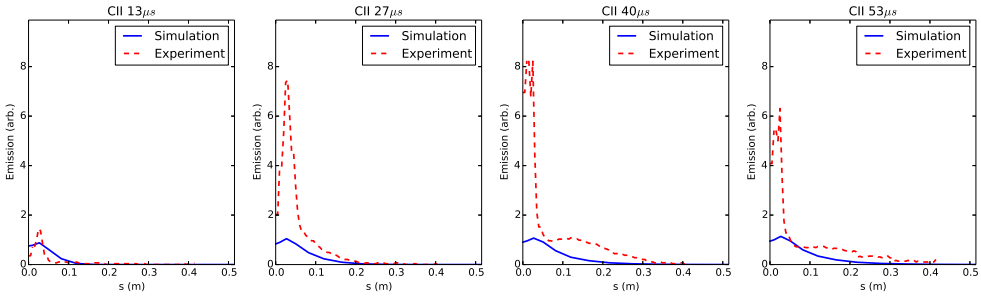

(a) 1cm shift

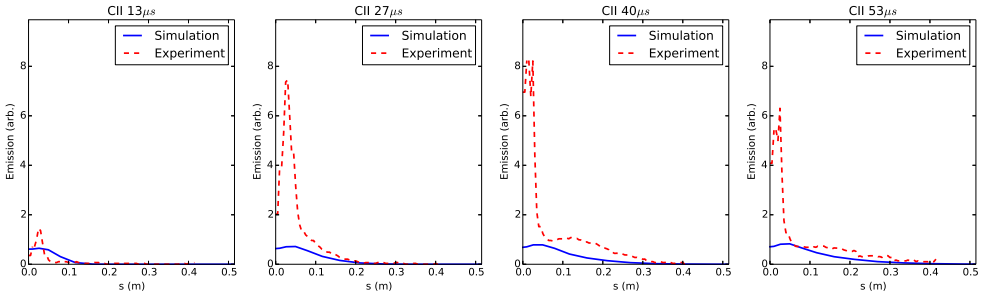

(b) 2cm shift

Figure 5.20: Comparison with experiment of transport parallel to the magnetic field for CII ions for H-mode shot 29139 with (a) 1cm and and (b) 2cm shift applied to the injection location. s is the distance along the magnetic field from the lower target.

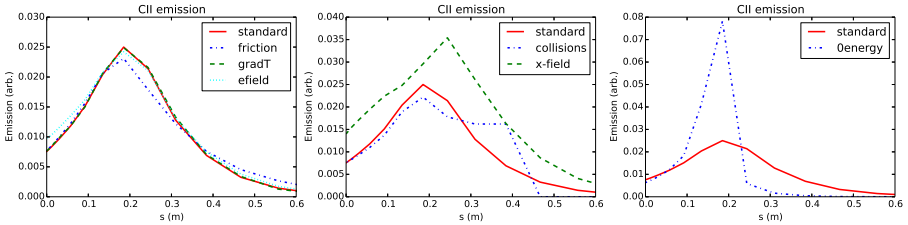

(a) 29125

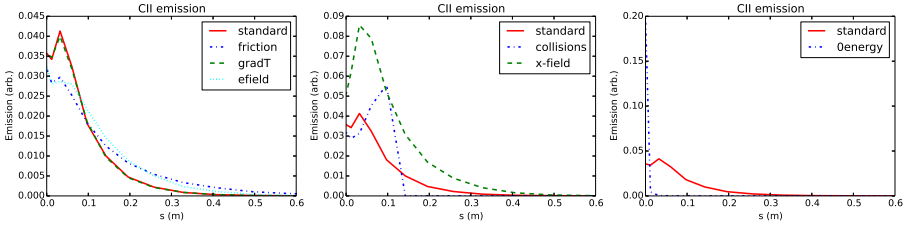

(b) 29126

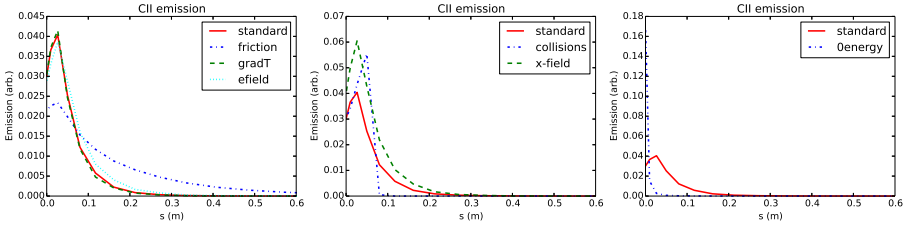

(c) 29139

Figure 5.21: Simulations with terms affecting impurity transport suppressed for shots 29125, 29126 ad 29139. The legend indicates the force term that has been suppressed. In each case the left panel shows the suppression of forces due to the temperature gradient, friction and electric field, these do not have a significant effect on the result. The middle panel shows simulations run without collisions and with the cross-field diffusion set to $0m^2s^{-1}$. The right panel shows impurities injected with energy of $0eV$, this appears to be the most significant factor in determining transport. s is the distance along the magnetic field from the lower target.

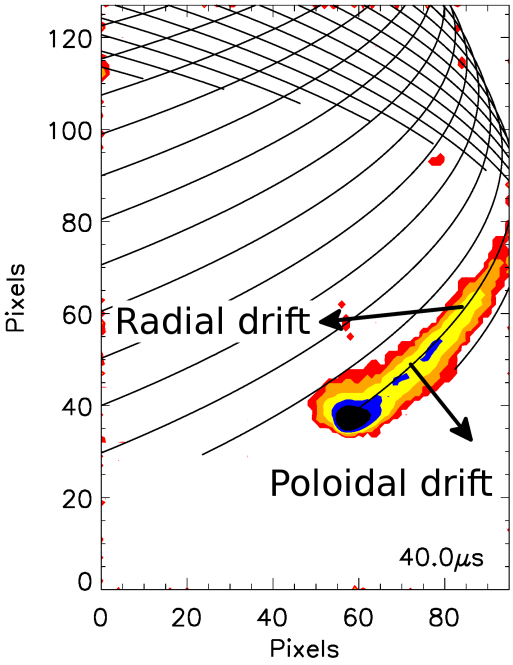

(a) Sector 1

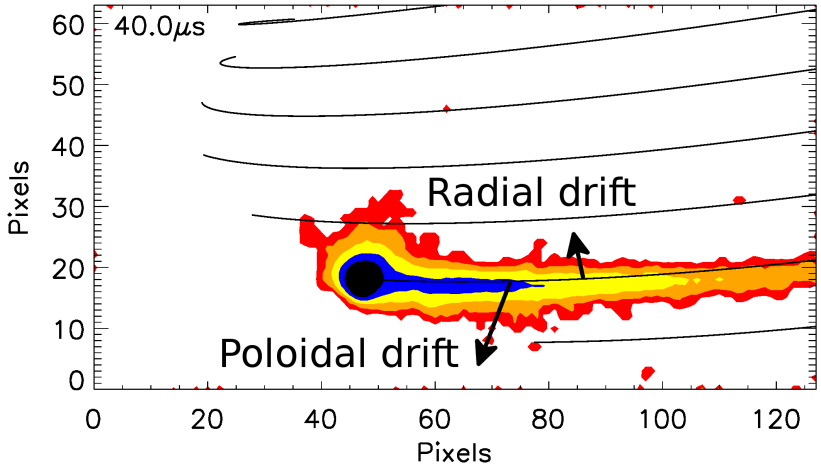

(b) Sector 11

Figure 5.22: Approximate direction of the radial and poloidal drifts in the image plane for for sectors 1(a) and 11(b) for H-mode shot 29139 40μs after injection. The plume appears to drift poloidally away from the magnetic field with the effect being more pronounced in the sector 11 image. Care must be taken in the interpretation of this due to errors in the magnetic equilibrium and magnetic field projection.

CHAPTER 6

Conclusions and further work

6.1 Conclusions

6.1.1 Injection system

It has been demonstrated that the carbon injector has successfully injected carbon atoms and ions into the MAST plasma. Diagnostic measurements suggest that the injection does not significantly perturb the plasma and yet is visible to cameras operating at frame rates up to $100kHz$. The capacitor discharge did not affect other systems present on the machine, including diagnostic and control systems. The simplicity of the design allows the equipment to be installed within a day, although testing of the associated systems is also required. The light weight of the injector head and limited number of wired connections means that this device is suitable for installation in various locations on the plasma vessel including the possibility of mounting on

reciprocating probes to allow injection into the SOL mid-plane. The financial cost of the system is also low when compared with other injection systems such as laser blow off.

The initialisation of the injection can be specified to within $1\mu s$ although there is a degree of variability of the quantity of injected carbon over the following $50\mu s$ to $100\mu s$. There is also significant uncertainty in the number of atoms and ions injected during the discharge. The ability to alter the discharge voltage allows injection into different plasma conditions while still keeping perturbation low. The final version of the system was shown to be extremely reliable and discharged with a success rate of 100% during the final set of experiments. The uncertainty in the energy of the injected carbon caused significant difficulties in comparison with simulation and would need to be addressed on future systems. The small quantity of carbon injected keeps the perturbation of the background plasma low so that modelling need not address the cooling associated with gas injection systems[172].

6.1.2 Modelling

The OSM approach is well suited for producing background plasma solutions for DIVIMP simulations. The use of experimental data to constrain the solution gives confidence in its accuracy close to the targets and avoids some of the the problems with target profiles associated with full 2D plasma codes[112, 170]. Conversely, the limited experimental constraints used in this study limit the validity of the solution away from the targets, this is highlighted by the disagreement between the simulated flow and that measured by the coherence imaging diagnostic for all shots studied. Using this data as a constraint is a natural next step in improving the background plasma solution. The simulation of flow is an issue for full 2D codes [169, 171] as

well as OSM and highlights the value of new diagnostic techniques such as this. The lack of drift terms in OSM is likely to play a role in the incorrect simulation of parallel flow, although development of the code is required to confirm this.

The errors introduced by the EFIT magnetic equilibrium reconstruction are significant and this work highlights the importance of accurate equilibrium reconstruction as conditions in the edge plasma varying significantly with location, as shown by the different behaviour of the carbon plume between shots 29125 and 29126, where the difference between the injection locations relative to the outer strike point is approximately 1cm. This effect is likely to be more pronounced in H-mode shots, which typically have a much reduced scrape off layer width, however only one H-mode shot was imaged while using carbon II filters. Despite this, sensitivity scans show that the solution is robust to errors up to approximately 1cm, however beyond this the solutions are altered significantly. The solution can be further improved using other experimental constraints such as spectroscopic imaging of D_α and D_γ emission[162].

The DIVIMP simulations of carbon transport based on the OSM plasma solutions show reasonable qualitative agreement with experimental data, in particular showing the diffuse nature of the parallel transport in L-mode shot 29125 and the low level of parallel transport seen in the H-mode shot 29139. The results are not sensitive to small changes in the background plasma resulting from shifting the target and target data, although shifts of approximately $1.5cm$ do have a significant impact on the simulated carbon distribution. The effect of plasma flow on carbon transport through friction is small but significant, increasing the importance of accurately modelling flow in the background plasma.

The simulation scan in the energy of injected ions and the study of the principle mechanisms affecting the simulated plume evolution show that energy of the injected carbon is likely to have a significant impact on the impurity transport, so that although the injection does not appear to significantly perturb the plasma the dynamics of the injected carbon are dominated by the injection energy and not by interactions with the background plasma. A scan in injection energy where injections are performed into the same plasma conditions with different charging voltages would help in understanding this issue, as would further study of the injection itself in a laboratory environment.

No attempt was made to compare the cross-field transport with experiment. Cross-field transport was included by setting the cross-field diffusion to an empirical value of $1m^2s^{-1}$. Disabling this transport had a significant effect on the parallel transport but did not qualitatively alter the result. Ideally the cross field transport would be set using cross-field transport coefficients obtained from the OSM solution, however the absence of drift terms in OSM reduces the reliability of these coefficients.

No drift terms are included in the DIVIMP simulations, however the effect of these terms on the parallel transport is likely to be dominated by the energy of the injected particles. The effects of cross-field drifts seen in previous work [51, 133] can potentially be seen, particularly in the case of H-mode shot 29139 where a deviation from the magnetic field can be seen. However uncertainties in both the magnetic equilibrium reconstruction and the registration of the camera images mean that no firm conclusions can be made from this.

The dominance of the energy of injected particles on the carbon transport complicates the desire to understand the transport of impurities arising from

sputtering of the first wall and from impurity seeding, however the effect of particle drifts can potentially be seen. The ability to vary the injected energy also provide a way of studying the transport of high energy sputtered products that may arise in the high power conditions expected in future devices such as ITER.

6.2 Further work

The first and most obvious improvement to this work is the use of a more tightly constrained EFIT equilibrium reconstruction. Although constrained EFIT cases were run that improved the strike point location, problems with generating grids suitable for use with DIVIMP-OSM-EIRENE meant that this data was not used in the simulations presented here. Using this reconstruction would reduce the uncertainties in the background plasma solution as well as more tightly constraining the injection location relative to the strike points. With the present data it appears that the impurities may not simply follow the field lines and actually deviate from the field, an effect that may well be caused by particle drifts. However as the magnetic data is error prone this may well be due to a combination of errors in the field used for the projection onto the image and in the registration of the cameras used in the projections.

Using an improved equilibrium may allow this effect to be studied with the potential to include $E \times B$ drifts present in the SOL. Including the measured flow as a constraint in the background plasma solution would further reduce uncertainties associated with the background plasma and allow a more detailed study of the effect of each of the terms governing impurity transport.

To really gain the most from this data 3D image reconstruction could be

attempted for the shots where carbon II filters were used on both cameras. Although full Abel inversion of the emission profile is likely to be problematic due to there only being 2 viewing angles a reconstruction of the emission surface should be possible. If this were to be done then comparisons could then be made with modelling in 3D and again it may be possible to infer information on drifts present in the SOL. Such 3D reconstructions could also help understand the cross field turbulent transport that is the subject of many current modelling efforts. Further to this the inclusion of drift effects in DIVIMP would allow their impact on the injected plume to be better studied.

The possibility to inject impurities into other regions of the plasma could provide further data on edge impurity transport. The method also has the potential to inject other conducting materials such as tungsten: this could provide useful data for the latest devices that use tungsten as a plasma facing material. However before this type of work is considered the difficulties associated with this technique must be addressed, in particular the apparent dominance of the energy of injected carbon on transport.

Bibliography

[1] S. A. Silburn, J. R. Harrison, J. Howard, K. J. Gibson, H. Meyer, C. A. Michael, and R. M. Sharples. Coherence imaging of scrape-off-layer and divertor impurity flows in the mega amp spherical tokamak. *Review of Scientific Instruments*, 85:11D703, 2014.

[2] ITER Physics Basis Editors, ITER Physics Expert Group Chairs and Co-Chairs and ITER Joint Central Team and Physics Integration Unit. ITER Physics Basis. *Nuclear Fusion*, 39(12):2137–2627, 1999.

[3] R. J. Hayward et al. Design, construction and operation of the dite divertor field system (divertor injection tokamak experiment). In *Symposium on Fusion Technology, 9th, Garmisch-Partenkirchen, West Germany*, pages 157–162, June 1976.

[4] F. Wagner et al. Regime of improved confinement and high beta in neutral-beam-heated divertor discharges of the ASDEX tokamak. *Physical Review Letters*, 49:1408–1412, 1982.

[5] P. Stangeby. *The Plasma Boundary of Magnetic Fusion Devices*. Bristol: Institute of Physics Publishing, 2000.

[6] J. Wesson. *Tokamaks*. OUP, 2000.

[7]

[8] S. J. Zweben, B. D. Scott, J. L. Terry, B. LaBombard, J. W. Hughes, and D. P. Stotler. Comparison of scrape-off layer turbulence in alcator c-mod with three dimensional gyrofluid computations. *Physics of Plasmas*, 16:082505, 2009.

[9] D. K. Owens et al. Pdx divertor operation. *Journal of Nuclear Materials*, 93-94:213, 1980.

[10] C. S. Pitcher and P. C. Stangeby. Experimental divertor physics. *Plasma Physics and Controlled Fusion*, 39:779–930, 1997.

[11] D.N. Hill et al. Measurement and modeling of the DIII-D divertor plasma. *Journal of Nuclear Materials*, 176-177:158–164, 1990.

[12] M. Keilhacker et al. Plasma boundary layer in limiter and divertor tokamaks. *Physica Scripta*, T2/2:443–453, 1982.

[13] S. K. Erents et al A. V. Chankin, S. Clements. The effect of b_t reversal on the asymmetries between the strike zones in single null divertor discharges: experiment and theories. *Plasma Physics and Controlled Fusion*, 36:2853, 1994.

[14] I. H. Hutchinson et al. The effects of field reversal on the Alcator C-Mod divertor. *Plasma Physics and Controlled Fusion*, 37(12):1389–1406, 1995.

[15] R Maingi et al. Effect of low density h-mode operation on edge and divertor plasma parameters. *Journal of Nuclear Materials*, 220-222: 320–324, 1995.

[16] P. H. Rutherfod R. J. Goldston. *Introduction to Plasma Physics*. Institute of Physics Publishing Bristol and Philadelphia, 2003. ISBN 07503 0183 X.

[17] A. V. Chankin. Classical drifts in the tokamak sol and divertor: models and experiment. *Journal of Nuclear Materials*, 241-243:199–213, 1997.

[18] S. I. Krasheninnikov. Reverse flow and parameter profiles in a dense tokamak divertor plasma. *Nuclear Fusion*, 32:1927, 1992.

[19] J. A. Boedo et al. Flow reversal, convection, and modeling in the DIII-D divertor. *Physics of Plasmas*, 5(12):4305–4310, 1998.

[20] N. Asakura et al. Measurement of natural plasma flow along the field lines in the scrape-off layer on the jt-60u divertor tokamak. *Physical Review Letters*, 84(14):3093–3096, 2000.

[21] G. F. Matthews S. K. Erents, A. V. Chankin and P. C. Stangeby. Parallel flow in the JET scrape-off layer. *Plasma Physics and Controlled Fusion*, 42:905–915, 2000.

[22] O. E. Garcia, R. A. Pitts, J. Horacek, J. Madsen, V. Naulin, A. H. Nielsen, and J. Juul Rasmussen. Collisionality dependent transport in tcv sol plasmas. *Plasma Physics and Controlled Fusion*, 49:B47–B57, 2007.

[23] B. A. Carreras. Plasma edge cross field transport: experiment and theory. *Journal of Nuclear Materials*, 337-339:315–321, 2005.

[24] A. Loarte. Understanding the edge physics of divertor experiments by comparison of 2D edge code calculations and experimental measurements. *Journal of Nuclear Materials*, 241-243:118–134, 1997.

[25] A. Kendl and B. D. Scott. Flux-surface shaping effects on tokamak edge turbulence and flows. *Physics of Plasmas*, 13:012504, 2006.

[26] V. Naulin. Shear flow generation and energetics in electromagnetic turbulence. *Physics of Plasmas*, 12:052515, 2005.

[27] T. T. Ribeiro and B. D. Scott. Tokamak turbulence computations on closed and open magnetic flux surfaces. *Plasma Physics and Controlled Fusion*, 47:1657–1679, 2005.

[28] S.I. Krasheninnikov. On scrape off layer plasma transport. *Physics Letters A*, 283:368–370, 2001.

[29] R. Jha et al. Intermittency in tokamak edge turbulence. *Physical Review Letters*, 69(9):1375–1378, 1992.

[30] J. A. Boedo et al. Transport by intermittent convection in the boundary of DIII-D. *Physics of Plasmas*, 8(11):4826–4833, 2001.

[31] V. Naulin. Turbulent transport and the plasma edge. *Journal of Nuclear Materials*, 363-365:24–31, 2007.

[32] J. A. Boedo et al. Intermittent convection in the boundary of DIII-D. *Journal of Nuclear Materials*, 313-316:813–819, 2003.

[33] S. J. Zwebwn et al. Edge turbulence imaging in the Alcator C-Mod tokamak. *Physics of Plasmas*, 9(5):1981–1989, 2002.

[34] G. R. McKee et al. Experimental characterization of coherent, radially-sheared zonal flows in the DIII-D tokamak. *Physics of Plasmas*, 10(5): 1712–1719, 2003.

[35] P. W. Terry. Suppression of turbulence and transport by sheared flow. *Reviews of Modern Physics*, 71(1):190–165, 2000.

[36] B. LaBombard et al. Transport-driven scrape-off layer flows and the x-point dependence of the l-h power threshold in Alcator C-Mod. *Physics of Plasmas*, 12:056111, 2005.

[37] R. A. Moyer et al. The role of turbulent transport in DIII-D edge and divertor plasmas. *Journal of Nuclear Materials*, 241-243:633–638, 1997.

[38] R. F. Post. Impurity radiation losses from a high temperature plasma. *Journal of Nuclear Energy, Part C PLasma Physics*, 3:273–286, 1961.

[39] Y Corre et al. Hybrid h-mode scenario with nitrogen seeding and type III ELMs in JET. *Plasma Physics and Controlled Fusion*, 50(11): 115012, 2008.

[40] S. Brezinsek et al. Chemical erosion measurements in tokamaks by spectroscopy. *Physica Scripta*, 111:42–48, 2004.

[41] L. Spitzer. *Physics of fully ionized gases*. Wiley, 1962.

[42] D. Reiter D. Reiser and M. Z. Tokar. Improved kinetic test particle model for impurity transport in tokamaks. *Nuclear Fusion*, 38(2):165, 1998.

[43] W. Fundamenski S. K. Erents, R. A. Pitts, J. P. Gunn, and G. F. Matthews. A comparison of experimental measurements and code re-

sults to determine flows in the JET SOL. *Plasma Physics and Controlled Fusion*, 46:1757–1780, 2004.

[44] R. Scannell et al. Design of a new nd:yag thomson scattering system for mast. *Review of Scientific Instruments*, 79(10):730, 2008.

[45] R. Pasqualotto et al. High resolution thomson scattering for Joint European Torus (JET). *Review of Scientific Instruments*, 75(10):3891, 2004.

[46] J Howard, C Michael, F Glass, and A Danielsson. Time-resolved two-dimensional plasma spectroscopy using coherence-imaging techniques. *Plasma Physics and Controlled Fusion*, 45:1143–1166, 2003.

[47] J. Howard, A. Diallo, M. Creese, B. D. Blackwell, S. L. Allen, R. M. Ellis, G. D. Porter, W. Meyer, M. E. Fenstermacher, N. H. Brooks, M. E. Van Zeeland, and R. L. Boivin. Doppler coherence imaging and tomography of flows in tokamak plasmas. *Review of Scientific Instruments*, 81:10E528, 2010.

[48] M. A. Van Zeeland, J. H. Yu, N. H. Brooks, W. W. Heidbrink, K. H. Burrell, R. J. Groebner, A. W. Hyatt, T. C. Luce, N. Pablant, W. M. Solomon, and M. R. Wade. Active and passive spectroscopic imaging in the diii-d tokamak. *Plasma Physics and Controlled Fusion*, 52:045006, 2010.

[49] S.J. Davies et al. Parallel electron temperature and density gradients measured in the JET MkI divertor using thermal helium beams. *Journal of Nuclear Materials*, 241-243:426–432, 1997.

[50] Jablonksi et al. Local impurity puffing as a scrape-off layer diagnostic

on the Alcator C-Mod tokamak. *Journal of Nuclear Materials*, 241-243: 782–787, 1997.

[51] S. Gangadhara and B. LaBombard. Impurity plume experiments in the edge plasma of the Alcator C-mod tokamak. *Plasma Physics and Controlled Fusion*, 46(10):1617–1646, 2004.

[52] L. Aho-Mantila, M. Wischmeier c, K. Krieger, V. Rohde, H.W. Mller, D.P. Coster, M. Groth, A. Kirschner, R. Neu c, S. Potzel c, B. Sieglin, E. Wolfrum, and The ASDEX Upgrade Team. Effect of e x b driven transport on the deposition of carbon in the outer divertor of asdex upgrade. *Journal of Nuclear Materials*, 415:S231–S234, 2011.

[53] G. M. McCracken et al. Screening of recycling and non-recycling impurities in the Alcator C-Mod tokamak. *Journal of Nuclear Materials*, 241-243:777–781, 1997.

[54] C.S. Pitcher et al. Carbon impurity transport around limiters in the DITE tokamak. *Journal of Nuclear Materials*, 162-164:337–342, 1989.

[55] W. Horton and W. Rowan. Impurity transport studies in the texas experimental tokamak (text). *Physics of Plasmas*, 1(4):901–908, 1994.

[56] A. G. McLean, J. W. Davis, P. C. Stangeby, N. H. Brooks, R. M. Ellis, A. A. Haasz, D. L. Rudakov, W. P. West, D. G. Whyte, and C. P. Wong. Porous plug gas injection systems for studies of hydrocarbon dissociation and transport in the DIII-D tokamak. *Review of Scientific Instruments*, 80(4):043501, 2009.

[57] K. Behringer. Measurement of ch^4/cd^4 fluxes and of chemical carbon erosion from ch/cd band emission. *Journal of Nuclear Materials*, 176-177:606–610, 1990.

[58] R. Pugno, K. Krieger, M. Airila, L. Aho-Mantila, A. Kreter, S. Brezinsek, V. Rohde, D. Coster, A. Chankin, M. Wischmeier, and the ASDEX Upgrade Team. Investigation of local carbon transport in the asdex upgrade divertor using $^{1}3ch_4$ puffing. *Journal of Nuclear Materials*, 390-391:68–71, 2009.

[59] J.D. Strachan et al. JET carbon screening experiments using methane gas puffing and its relation to intrinsic carbon impurities. *Nuclear Fusion*, 43:922–941, 2003.

[60] G.M. McCracken1990. A study of impurity transport in the plasma boundary of textor using gas puffing. *Journal of Nuclear Materials*, 176-177:191–196, 1990.

[61] B. LaBombard et al. A novel tracer-gas injection system for scrape-off layer impurity transport and screening experiments. *Journal of Nuclear Materials*, 266-269:571–576, 1999.

[62] A. G. McLean, P. C. Stangeby, B. D. Bray, S. Brezinsek, N. H. Brooks, J. W. Davis, R. C. Isler, A. Kirschner, R. Laengner, C. J. Lasnier, Y. Mub, J. Munoz, D. L. Rudakov, O. Schmitz, E. A. Unterberg, J. G. Watkins, D. G. Whyte, and C. P. C. Wong. Quantification of chemical erosion in the diii-d divertor and implications for iter. *Journal of Nuclear Materials*, 415:S141–S144, 2011.

[63] A. Hakola, J. Likonen, L. Aho-Mantila, M. Groth1, S. Koivuranta, K. Krieger, T. Kurki-Suonio, T. Makkonen, M. Mayer, H. W. Müller, R. Neu, V. Rohde, and the ASDEX Upgrade Team. Migration and deposition of 13c in the full-tungsten asdex upgrade tokamak. *Plasma Physics and Controlled Fusion*, 52:065006, 2010.

[64] R. Pugno, , K. Krieger, A. Kirschner, A. Kallenbach, D. P. Coster, R. Dux, U. Fantz, J. Likonen, H. W. Muüller, J. Neuhauser, V. Rohde, E. Vainonen-Ahlgren, and the ASDEX Upgrade Team. Carbon chemical erosion in H-mode discharges in ASDEX Upgrade divertor IIb:flux dependence and local redeposition. *Journal of Nuclear Materials*, 337-339:985–989, 2005.

[65] S. Brezinsek, A. Pospieszczyk, D. Borodin, M. F. Stamp, R. Pugno, , A. G. McLean, U. Fantz, A. Manhard, A. Kallenbach, N. H. Brooks, M. Groth, Ph. Mertens, V. Philipps, U. Samm, DIII-D Teams the TEXTOR, ASDEX Upgrade, and JET-EFDA Contributors. Hydrocarbon injection for quantification of chemical erosion yields in tokamaks. *Journal of Nuclear Materials*, 363-365:1119–1128, 2007.

[66] P. C. Stangeby, A. G. McLean, J. D. Elder, N. H. Brooks, , W.P. West, and D. Reiter. Measurements of the average energy of carbon atoms released from breakup of methane in the main sol of diii-d compared with divimp code modeling. *Journal of Nuclear Materials*, 363-365: 201–205, 2007.

[67] M.F. Stamp et al. Experimental determination of the contribution of chemical sputtering of carbon on carbon core concentrations. *Journal of Nuclear Materials*, 266-269:685, 1999.

[68] C. Giroud, R. Barnsley, P. Buratti, I. H. Coffey, M. von Hellermann, C. Jupén, K. D. Lawson, A. Meigs, M. O'Mullane, A. D. Whiteford, K-D. Zastrow, and the JET EFDA contributors. Method for experimental determination of Z dependence of impurity transport on JET. *Nuclear Fusion*, 47:313–330, 2007.

[69] V. A. Soukhanovskii, H. W. Kugel, R. Kaita, R. Majeski, and A. L. Roquemore. Supersonic gas injector for fueling and diagnostic applications on the national spherical torus experiment. *Review of Scientific Instruments*, 75(10):4320, 2004.

[70] J.E. Menard, S. Gerhardt, M. Bell, J. Bialek, A. Brooks, J. Canik, J. Chrzanowski, M. Denault, L. Dudek, D.A.Gates, N. Gorelenkov, W. Guttenfelder, R. Hatcher, J. Hosea, R. Kaita, S. Kaye, C. Kessel, E. Kolemen, H.Kugel, R. Maingi, M. Mardenfeld, D. Mueller, B. Nelson, C. Neumeyer, M. Ono, E. Perry, R. Ramakrishnan, R.Raman, Y. Ren, S. Sabbagh, M. Smith, V. Soukhanovskii, T. Stevenson, R. Strykowsky, D. Stutman, G. Taylor, P.Titus, K. Tresemer, K. Tritz, M. Viola, M. Williams, R. Woolley, H. Yuh, H. Zhang, Y. Zhai, A. Zolfaghari, and the NSTX Team. Overview of the physics and engineering design of nstx upgrade. *Nuclear Fusion*, 52(8):083015, 2012. URL `http://stacks.iop.org/0029-5515/52/i=8/a=083015`.

[71] M.G. O'Mullane et al. Diagnostic exploitation of complex heavy elements in tokamak plasmas. *Review of Scientific Instruments*, 74(3): 2080–2083, 2003.

[72] D. Pasini et al. Measurements of impurity transport in JET. *Plasma Physics and Controlled Fusion*, 34(5):677–685, 1992.

[73] Galli et al. Transient heat transport studies using laser ablated impurity injection in JET. *Nuclear Fusion*, 38(9):1355, 1998.

[74] R. Dux et al. Influence of the heating profile on impurity transport in ASDEX Upgrade. *Plasma Physics and Controlled Fusion*, 45(45): 1815–1825, 2003.

[75] R. Dux E. Scavino, J. S. Bakos and H. Weisen. Effects of plasma shape on laser blow-off injected impurity transport in TCV. *Plasma Physics and Controlled Fusion*, 45:1961–1974, 2003.

[76] A. Geier, K. Asmussen, A. Bard, R. Neu, and K. Krieger. A sublimation probe for the injection of High-Z impurities into fusion devices. *Review of Scientific Instruments*, 70(1):63–67, 1999.

[77] R. Schneider, X. Bonnin, K. Borrass, D. P. Coster, H. Kastelewicz, D. Reiter, V. A. Rozhansky, , and B. J. Braams. Plasma edge physics with b2-eirene. *Contributions to Plasma Physics*, 46(1-2):3–191, 2006.

[78] P. C. Stangeby, C. Farrell, S. Hoskins, and L. Wood. Monte carlo modelling of impurity ion transport for a limiter source/sink. *Nuclear Fusion*, 28(11):1945, 1988.

[79] M. Ali Mahdavi et al. Particle exhaust from plasma discharges with an expanded-boundary divertor. *Physical Review Letters*, 47(22):1602–1605, 1981.

[80] G. F. Counsell, J. W. Connor, S. K. Erents, A. R. Field, S. J. Fielding, B. La Bombard, and K. M. Morel. Sol width scaling from consideration of edge transport in tokamaks. *Journal of Nuclear Materials*, 266-269: 91–98, 1999.

[81] Farrokh Najmabadi Emad Zawaideh and Robert W. Conn. Generalized fluid equations for parallel transport in collisional to weakly collisional plasma. *Physics of Fluids*, 29(2):463, 1986.

[82] L. Tonks and I. Langmuir. A general theory of the plasma arc. *Physical Review*, 34:876–922, 1929.

[83] D. Reiter. Progress in two-dimensional plasma edge modelling. *Journal of Nuclear Materials*, 196-198:80–89, 1992.

[84] P.C. Stangeby and J.D. Elder. Impurity retention by divertors part i: One dimensional models. *Nuclear Fusion*, 35(11):1391–1412, 1995.

[85] B.J. Braams. *Computational studies in tokamak equilibrium and transport*. PhD thesis, University of Utrecht, 1986.

[86] A. Taroni, G. Corrigan, G. Radford, R. Simonini, J. Spence, and S. Weber. The multi-fluid codes edgeid and edge2d: Models and results. *Contributions to Plasma Physics*, 32:438–443, 1992.

[87] R. Simonini, G. Corrigan, G. Radford, J. Spence, and A. Taroni. Models and numerics in the Multi-Fluid 2-D edge plasma code EDGE2D/U. *Contributions to Plasma Physics*, 34:368–373, 1994.

[88] T. D. Rognlien, P. N. Brown, R. B. Campbell, T. B. Kaiser, D. A. Knoll, P. R. McHugh, G. D. Porter, M. E. Rensink, and G. R. Smith. 2-d fluid transport simulations of gaseous/radiative divertors. *Contributions to Plasma Physics*, 34:362–367, 1994.

[89] T.D. Rognlien et al. Advances in understanding tokamak edge/scrape-off layer transport. In *23rd IAEA Fusion Energy Conference, 11-16 October 2010, Daejeon, Republic of Korea*, pages P3–05, October 2010.

[90] P. Börne D. Reiter, M. Baelmans. The eirene and b2-eirene codes. *Fusion Science and Technology*, 47(2):172–186, 2005.

[91] A. V. Chankin, D. P. Coster, R. Dux, Ch. Fuchs, G. Haas, A. Herrmann, L. D. Horton, A. Kallenbach, M. Kaufmann, Ch. Konz,

K. Lackner, C. Maggi, H. W. Müller, J. Neuhauser, R. Pugno, M. Reich, and W. Schneider. SOLPS modelling of ASDEX upgrade H-mode plasma. *Plasma Physics and Controlled Fusion*, 48:839–868, 2006.

[92] Y. Chen, G. Xu, J. Hu, and D. P. Coster. Edge plasma modelling for HT-7 superconducting tokamak experiments. *Journal of Nuclear Materials*, 363-365:54–549, 2007.

[93] E. Havlíčková, M. Wischmeier, and G. Fishpool. Modelling the effect of the super-x divertor in mast upgrade on transition to detachment and distribution of volumetric power losses. *Contributions to Plasma Physics*, 54(4-6):448–453, 2014.

[94] L. W. Owen, J. M. Canik, R. J. Groebner, J. D. Callen, X. Bonnin, and T. H. Osborne. Comparing 1.5D ONETWO and 2D SOLPS analyses of inter-ELM H-mode plasma in DIII-D. *Nuclear Fusion*, 50(6):064017, 2010.

[95] P. C. Stangeby, J. M. Canik, and D. G. Whyte. The relation between upstream density and temperature widths in the scrape-off layer and the power width in an attached divertor. *Nuclear Fusion*, 50(12): 125003, 2010.

[96] L. Aho-Mantila, M. Wischmeier, H. W. Müller, D. P. Coster S. Potzel, X. Bonnin, G. D. Conway, and the ASDEX Upgrade Team. Outer divertor of asdex upgrade in low-density l-mode discharges in forward and reversed magnetic field: I. comparison between measured plasma conditions and solps5.0 code calculations. *Nuclear Fusion*, 52:103006, 2012.

[97] M. Wischmeier, M. Groth, A. Kallenbach, A. V. Chankin, D. P. Coster, R. Dux, A. Herrmann, H. W. Müller, R. Pugno, D. Reiter, A. Scarabosio, J. G. Watkins, DIII-D team, and ASDEX Upgrade team. Current understanding of divertor detachment: Experiments and modelling. *Journal of Nuclear Materials*, 390-391:250–254, 2009.

[98] B. Viola, G. Calabró, F. Crisanti, G. Maddaluno, V. Pericoli Ridolfini, R. Albanese, G. Artaserse, R. Zag/'orski, A. Kallenbach, W. Treutterer, and ASDEX Upgrade Team. Divertor plasma shaping and modeling of ASDEX upgrade. page P5.069, 2011.

[99] S. K. Erents, W. Fundamenski, G. Corrigan, G. F. Matthews, R. Zagorski, and EFDA-JET Contributors. EDGE2D modelling of JET and ITER including the combined effect of guiding centre drifts and an edge transport barrier. *Journal of Nuclear Materials*, 363-367: 565–569, 2007.

[100] B. Viola, G. Corrigan, D. Harting, G. Maddaluno, M. Mattia, V. Pericoli Ridolfini, and R. Zagórski. Preliminary comparison of the conventional and quasi-snowflake divertor configurations with the 2d code edge2d/eirene in the fast tokamak. *Contributions to Plasma Physics*, 54:459–463, 2014.

[101] A. Kallenbach, Y. Andrew, M. Beurskens, G. Corrigan, T. Eich, S. Jachmich, M. Kempenaars, A. Korotkov, A. Loarte, G. Matthew, P. Monier-Garbet, G. Saibene, J. Spence, W. Suttrop, and JET EFDA Contributors. EDGE2D modelling of edge profiles obtained in jet diagnostic optimized configuration. *Plasma Physics and Controlled Fusion*, 46:431, 2004.

[102] J. D. Strachan, J. Likonen, P. Coad, M. Rubel, A. Widdowson, M. Airila, P. Andrew, S. Brezinsek, G. Corrigan, H. G. Esser, S. Jachmich, A. Kallenbach, A. Kirschner, A. Kreter, G. F. Matthews, V. Philipps, R. A. Pitts, J. Spence, M. Stamp, S. Wiesen, and JET-EFDA contributors. Modelling of carbon migration during JET ^{13}C injection experiments. *Nuclear Fusion*, 48:105002, 2008.

[103] C. Guillemaut, R. A. Pitts, A. S. Kukushkin, J. P. Gunn, J. Bucalossi, G. Arnoux, P. Belo, S. Brezinsek, M. Brix, G. Corrigan, S. Devaux, J. Flanagan, M. Groth, D. Harting, A. Huber, S. Jachmich, U. Kruezi, M. Lehnen, C. Marchetto, S. Marse, A. G. Meigs, O. Meyer, M. Stamp, J. D. Strachan, S. Wiesen, M. Wischmeier, and JET EFDA Contributors. Influence of atomic physics on EDGE2D-EIRENE simulations of jet divertor detachment with carbon and beryllium/tungsten plasma-facing components. *Nuclear Fusion*, 54:093012, 2014.

[104] G. S. Kirnev, G. Corrigan, D. Coster, S. K. Erents, W. Fundamenski, G. F. Matthews, and R. A. Pitts. Edge2d code simulations of sol flows and inout divertor asymmetries in jet. *Journal of Nuclear Materials*, 337-339:271–275, 2005.

[105] .P. Coster, , X. Bonnin, G. Corrigan, G. S. Kirnev, G. Matthews, J. Spence, and Contributors to the EFDA-JET work programme. Benchmarking tokamak edge modelling codes. *Journal of Nuclear Materials*, 337-339:366–370, 2005.

[106] S.L. Allen, J. A. Boedo, A. S. Bozek, N. H. Brooks, T. N. Carlstrom, T. A. Casper, R. J. Colchin, T. E. Evans, M. E. Fenstermacher, M. E. Friend, R. C. Islera, R. Jayakumar, C. J. Lasnier, A. W. Leonard, M. A. Mahdavi, R. Maingi, G. R. McKee, R. A. Moyer, M. Murakami, T. H.

Osborne, R. C. O'Neill, T. W. Petrie, G. D. Porter, A. T. Ramsey, M. J. Schaffer, P. C. Stangeby, R. D. Stambaugh, M. R. Wade, J. G. Watking, W. P. West, D. G. Whyte, and N. S. Wolf. Experiments and computational modeling focused on divertor and sol optimization for advanced tokamak operation on DIII-D. *Journal of Nuclear Materials*, 290-293:995–1001, 2001.

[107] J.M. Munoz Burgos, A. W. Leonard, S. D. Loch, and C. P. Ballance. Evaluation of an improved atomic data basis for carbon in uedge emission modeling for l-mode plasmas in diii-d. *Journal of Nuclear Materials*, 438:S406–S409, 2013.

[108] T. W. Petrie, N. H. Brooks, M. E. Fenstermacher, M. Groth, A. W. Hyatt, C. J. Lasnier, A. W. Leonard, G. D. Porter, M. J. Schaffer, M. R. Wade, J. G. Watkins, and W. P. West. Sensitivity of injected argon behavior to changes in magnetic balance in double-null plasmas in diii-d. *Journal of Nuclear Materials*, 390-391:242–245, 2009.

[109] A. Yu. Pigarov, S. I. Krasheninnikov, T. D. Rognlien, C. J. Lasnier, and E. Unterberg. Dynamic plasma-wall modeling of elmy h-mode with uedge-mb-w. *Journal of Nuclear Materials*, 463:705–708, 2015.

[110] G. D. Porter, T. W. Petrie, T. D. Rognlien, and M. E. Rensink. UEDGE simulation of edge plasmas in DIII-D double null configurations. *Physics of Plasmas*, 17:112501, 2010.

[111] W. P. West, G. D. Porter, T. E. Evans, P. Stangeby, N. H. Brooks, M. E. Fenstermacher, R. C. Isler, T. D. Rognlien, M. R. Wade, D. G. Whyte, and N. S. Wolf. Modeling of carbon transport in the divertor

and SOL of DIII-D during high performance plasma operation. *Journal of Nuclear Materials*, 290-293:783–787, 2001.

[112] M. Groth, G. D. Porter, M. E. Rensink, T. D. Rognlien, S. Wiesen, M. Wischmeier, T. Eich, A. Herrmann, S. Jachmich, C. J. Lasnier, H. W. Müller, J. G. Watkins, M. N. A. Beurskens, B. D. Bray, S. Brezinsek, N. H. Brooks, M. E. Fenstermacher, C. Fuchs, A. Huber, A. Kallenbach, A. W. Leonard, A. Meigs, D. L. Rudakov, ASDEX Upgrade Teams The DIII-D, and JET EFDA Contributors. Influence of cross-field drifts and chemical sputtering on simulations of divertor particle and heat loads in ohmic and l-mode plasmas in diii-d, aug, and jet using uedge. *Journal of Nuclear Materials*, 415:S530–S534, 2011.

[113] E. T. Meier, V. A. Soukhanovskii, R. E. Bell, A. Diallo, R. Kaita, B. P. LeBlanc, A. G. McLean, M. Podestà, and F. Scott T.D. Rognlien and. Modeling detachment physics in the nstx snowflake divertor. *Journal of Nuclear Materials*, 463:1200–1204, 2015.

[114] T. D. Rognlien, R. H. Bulmer, M. E. Rensink, and J. N. Brooks. Scrape-off layer plasmas for iter with 2nd x-point and convective transport effects. *Journal of Nuclear Materials*, 363-365:658–663, 2007.

[115] S.K. Erents and P.C. Stangeby. Heat transport in the JET scrape-off layer. *Nuclear Fusion*, 38:1637, 1998.

[116] P.C. Stangeby W. Fundamenski and J.D. Elder. A cfd onion-skin model for the interpretation of edge experiments. *Journal of Nuclear Materials*, 266-269:1045–1050, 1999.

[117] S. Lisgo et al. OSM-EIRENE modeling of neutral pressures in the

Alcator C-Mod divertor. *Journal of Nuclear Materials*, 337-339:139–145, 2005.

[118] W. Fundamenski, S.K. Erents, G.F. Matthews, A.V. Chankin, V. Riccardo, P.C. Stangeby, and J.D. Elder. Analysis of SOL behaviour in JET MkIIGB using an advanced onion-skin solver (OSM2). *jnuclmater*, 290-293:593, 2001.

[119] J. Harrison, S. Lisgo, G. F. Counsell, K. Gibson, J. Dowling, L. Trojan, and D. Reiter. Interpretive modelling of scrape-off plasmas on the mast tokamak. *Journal of Nuclear Materials*, 390-391:392–394, 2009.

[120] A. Kirk, W. Fundamenski, J-W. Ahn, and G. Counsell. Parallel SOL transport in MAST and JET: the impact of the mirror force. *Plasma Physics and Controlled Fusion*, 45:1445–1463, 2003.

[121] D. Harting et al. 3D Edge Transport Studies with EMC3-EIRENE for the Dynamic Ergodic Divertor (DED) at TEXTOR. *Contributions to Plasma Physics*, 48(1-3):99–105, 2008.

[122] M. Kobayashi et al. 3D edge transport analysis of ITER start-up configuration for limiter power load assessment. *Nuclear Fusion*, 47(2): 61–73, 2007.

[123] B. D. Dudson, A. Allen, G. Breyiannis, E. Brugger, J. Buchanan, L. Easy, S. Farley, I. Joseph, M. Kim, A. D. McGann, J. T. Omotani, M. V. Umansky, N. R. Walkden, T. Xia, and X. Q. Xu. Bout++: Recent and current developments. *Journal of Plasma Physics*, 81: 365810104, 2014.

[124] S. Ku et al. Gyrokinetic particle simulation of neoclassical transport in

the pedestal/scrape-off region of a tokamak plasma. *Journal of Physics: Conference Series*, 46:87–91, 2006.

[125] K. Bodi R.H. Cohen X.Q. Xu1, S. Krasheninnikov, and T.D. Rognlien. Tempest simulations of the plasma transport in a single-null tokamak geometry. *Nuclear Fusion*, 50:064003, 2010.

[126] F. Jenko and W. Dorland. Nonlinear electromagnetic gyrokinetic simulations of tokamak plasmas. *Plasma Physics and Controlled Fusion*, 43:A141–A150, 2001.

[127] M. Kotschenreuther W. Dorland, F. Jenko and B. N. Rogers. Electron temperature gradient turbulence. *Physical Review Letters*, 85:5579–5582, 2000.

[128] Y. Chen and S. E. Parker. Electromagnetic gyrokinetic f particle-in-cell turbulence simulation with realistic equilibrium profiles and geometry. *Journal of Computational Physics*, 220:839–855, 2007.

[129] R.H. Cohen et al. Testing and plans for the cogent edge kinetic code, 2010.

[130] J. Cummings et al. Plasma Edge Kinetic-MHD Modeling in Tokamaks Using KeplerWorkflow for Code Coupling, Data Management and Visualization. *Communications in Computational Physics*, 4(3):675–702, 2008.

[131] J. Winterb A. Kirschnera, V. Philippsa and U. Köglera. Simulation of the plasma-wall interaction in a tokamak with the monte carlo code ero-textor. *Nuclear Fusion*, 40:989, 2000.

[132] K. Shimizu, H. Kubo, T. Takizuka, M. Azumi, M. Shimada, S. Tsuji, N. Hosogane, T. Sugie, A. Sakasai, N. Asakura, and S. Higashijim. Impurity transport modelling and simulation analysis of impurity behavior in JT-60U. *Journal of Nuclear Materials*, 220-222:410–414, 1995.

[133] L. Aho-Mantila, M. Wischmeier, K. Krieger, V. Rohde, A. Hakola, S. Potzel, A. Kirschner, and D. Borodin the ASDEX Upgrade Team. Outer divertor of asdex upgrade in low-density l-mode discharges in forward and reversed magnetic field: Ii. analysis of local impurity migration. *Nuclear Fusion*, 52:103007, 2012.

[134] T. Makkonen, M. Groth, T. Kurki-Suonio, K. Krieger, L. Aho-Mantila, A. Hakola, J. Likonen, H. W. Müller, and the ASDEX Upgrade Team. Divimp simulations of 13c puffing experiments in asdex upgrade l-mode plasma. *Journal of Nuclear Materials*, 415:S479–S482, 2011.

[135] K. Ohya, K. Inai, T. Tanabe, and H. Takenaga. Modeling of asymmetric redeposition distribution between inner and outer regions of the w-shaped divertor in jt-60u. *Journal of Nuclear Materials*, 363-365: 78–85, 2007.

[136] D. Naujoks, R. Behrisch, J. P. Coad, and L. C. J. M. De Kock. Carbon chemical erosion in H-mode discharges in ASDEX Upgrade divertor IIb:flux dependence and local redeposition. *Journal of Nuclear Materials*, 337-339:985–989, 2005.

[137] H. Kawashima, K. Shimizu, and T. Takizuka. Development of integrated sol/divertor code and simulation study of the jt-60u/jt-60sa tokamaks. *Plasma Physics and Controlled Fusion*, 49:S77–S85, 2007.

[138] K. Shimizu, T. Takizuka, S. Sakurai, H. Tamai, H. Takenaga, H. Kubo, and Y. Miura. Simulation of divertor detachment characteristics in jt-60 with superconducting coils. *Journal of Nuclear Materials*, 313-316: 1277–1281, 2003.

[139] K. Shimizu, T. Takizuka, K. Ohya, K. Inai, T. Nakano, A. Takayama, H. Kawashima, and K. Hoshino. Kinetic modelling of impurity transport in detached plasma for integrated divertor simulation with SONIC (SOLDOR/NEUT2D/IMPMC/EDDY). *Nuclear Fusion*, 49:065028, 2009.

[140] K. Hoshino, , K. Shimizu, T. Takizuka, N. Asakura, and T. Nakano. Improvement of the detachment modelling in the SONIC simulation. *Journal of Nuclear Materials*, 415:S549–S552, 2011.

[141] H. Kawashima, K. Hoshino, K. Shimizu, T. Takizuka, S. Ide, S. Sakurai, and N. Asakura. Evaluation of heat and particle controllability on the jt-60sa divertor. *Journal of Nuclear Materials*, 415:S948–S951, 2011.

[142] K. Shimizu, T. Takizuka, and H. Kawashima. Kinetic effect of thermal force on impurity transport: Simulation of JT-60SA divertor with integrated divertor code SONIC. *Journal of Nuclear Materials*, 49:065028, 2009.

[143] S. Ishida, P. Barabaschi, Y. Kamada, and the JT-60SA Team. Status and prospect of the JT-60SA project. *Fusion Engineering and Design*, 85:2070–2079, 2010.

[144] A. G. McLean, J. D. Elder, P. C. Stangeby, S. L. Allen, J. A. Boedo, N. H. Brooks, M. E. Fenstermacher, M. Groth, S. Lisgoand A. Nagy,

D. L. Rudakov, W. R. Wampler, J. G. Watkins, W. P. West, and D. G. Whyte. Divimp modeling of the toroidally symmetrical injection of 13ch4 into the upper sol of diii-d. *Journal of Nuclear Materials*, 337-339:124–128, 2005.

[145] Y. Mu, J. D. Elder, P. C. Stangeby, and A. G. McLean. 3D-DIVIMP(HC) code modeling of DIII-D DiMES porous plug injector experiments. *Journal of Nuclear Materials*, 415:S145–S148, 2011.

[146] A. Järvinen, C. Giroud, M. Groth, K. Krieger, D. Moulton, S. Wiesen, S. Brezinsek, and JET-EFDA contributors. Divimp simulation of W transport in the SOL of JET H-mode plasmas. T145:014013, 2011.

[147] A. Xuereb, M. Groth, K. Krieger, , O. Asunta, T. Kurki-Suonio, J. Likonen, D. P. Coster, and the ASDEX Upgrade Team. DIVIMP-B2-EIRENE modelling of ^{13}c migration and deposition in ASDEX Upgrade L-mode plasmas. *Journal of Nuclear Materials*, 396:228–233, 2010.

[148] K. Schmid, K. Krieger, A. Kukushkin, and A. Loarte. DIVIMP modeling of tungsten impurity transport in ITER. *Journal of Nuclear Materials*, 363-365:674–679, 2007.

[149] M. Cox. The mega ampere spherical tokamak. *Fusion Engineering and Design*, 46:397–404, 1999.

[150] G. de Temmerman, M. Bacharis, J. Dowling, and S. Lisgo. Dust creation and transport in mast. *Nuclear Fusion*, 50:105012, 2010.

[151] S. Elmore, S. Y. Allan, A. Kirk, G. Fishpool, J. Harrison, P. Tamain, M. Kočan, R. Gaffka, R. Stephen, J. W. Bradley, and the MAST Team.

Upstream and divertor ion temperature measurements on mast by retarding field energy analyser. *Plasma Physics and Controlled Fusion*, 54:065001, 2012.

[152] V. Rozhansky, P. Molchanov, S. Voskoboynikov, G. Counsell, A. Kirk, D. Coster, and R. Schneider. Modeling of the parametric dependence of the edge toroidal rotation for mast and asdex upgrade. *Journal of Nuclear Materials*, 363-365:664–668, 2007.

[153] J. Marshall. Performance of a hydromagnetic plasma gun. *Physics of Fluids*, 3:134–135, 1960.

[154] John F O'Hanlon. *A User's Guide to Vacuum Technology*. Wiley, 2003.

[155] Günter Sauerbrey. Verwendung von schwingquarzen zur wägung dünner schichten und zur mikrowägung. *Zeitschrift für Physik*, 155 (2):206–222, 1959.

[156] C.P.C. Wong et al. Divertor materials evaluation system (dimes). *Journal of Nuclear Materials*, 258-263:433–439, 1998.

[157] S.J.Fielding G.F. Counsell, J-W. Ahna and G.P.Maddison. Divertor power loading studies in the mast tokamak. In *27th EPS Conference on Contr. Fusion and Plasma Phys. Budapest, Hungary*, volume 24B, pages 1577–1580, 2000.

[158] K. J. Gibson et al. New physics capabilities from the upgraded thomson scattering diagnostic on mast. *Plasma Physics and Controlled Fusion*, 52:124041, 2010.

[159] R. Scannell et al. A 130 point nd:yag thomson scattering diagnostic on mast. *Review of Scientific Instruments*, 81:10D520, 2010.

[160] L.L. Lao, H. St. John, R.D. Stambaugh, A.G. Kellman, and W. Pfeiffer. Reconstruction of current profile parameters and plasma shapes in tokamaks. *Nuclear Fusion*, 25:1611, 1985.

[161] J. D. Elder. Divimp options. `http://starfire.utias.utoronto.ca/divimp/docs/divdocs.html`.

[162] S. Lisgo, P. C. Stangeby, J. D. Elder, J. A. Boedo, B. D. Bray, N. H. Brooks, M. E. Fenstermacher, M. Groth, D. Reiter, D. L. Rudakov, J. G. Watkins, W. P. West, and D. G. Whyte. Re-construction of detached divertor plasma conditions in DIII-D using spectroscopic and probe data. *Journal of Nuclear Materials*, 337-339:256–260, 2005.

[163] H. P. Summers. *The ADAS User Manual, version 2.6 http://www.adas.ac.uk*. 2004.

[164] A. J. Wootton, B. A. Carreras, H. Matsumoto, W. A. Peebles, Ch. P. Ritz, and P. W. Terry amd S. J. Zweben. Fluctuations and anonymous transport in tokamaks. *Phys. Fluids B*, 2(12):2879–2903, 1990.

[165] A. Anders, S. Anders, I. G. Brown, M. R. Dickinson, and R. A. MacGill. Metal plasma immersion ion implantation and deposition using vacuum arc plasma sources. *Journal of Vacuum Science and Technology*, 12: 815, 1994.

[166] J. Rosén, J. M. Schneider, and A Anders. Charge state dependence of cathodic vacuum arc ion energy and velocity distributions. *Applied Physics Letters*, 89:141502, 2006.

[167] A. G. Nikolaev, E. M. Oks, G. Yu. Yushkov K. P. Savkin, and I. G. Brown. Upgraded vacuum arc ion source for metal ion implantation. *Review of Scientific Instruments*, 83:02A501, 2012.

[168] E. Byon and A. Anders. Ion energy distribution functions of vacuum arc plasmas. *Journal of Applied Physics*, 93(4):1899, 2003.

[169] K. Hoshino, A. Hatayama, N. Asakura, H. Kawashima, R. Schneider, and D. Coster. Numerical analysis of the SOL/divertor plasma flow with the effect of drifts. *Journal of Nuclear Materials*, 363-365:539–543, 2007.

[170] L. Aho-Mantila, M. Wischmeier, M. I. Airila, A. V. Chankin, D.P. Coster Ch. Fuchs, M. Groth, A. Kirschner, K. Krieger, H. W. Müller, E. Wolfrum, and the ASDEX Upgrade Team. Modelling of carbon transport in the outer divertor plasma of asdex upgrade. *Contributions to Plasma Physics*, 50(3-5):439–444, 2010.

[171] G. D. Porter, T. D. Rognlien, M. E. Rensink, A. Loarte, N. Asakura, H. Takenaga, G. Matthews, and Contributors to the EFDA-JET Work Programme. Simulation of the effect of plasma flows in DIII-D, JET, and JT-60U. *Journal of Nuclear Materials*, 313-316:1085–1088, 2003.

[172] R. Ding, A. Kirschner, M. Z. Tokar, M. Koltunov, D. Borodin, S. Brezinsek, A. Kreter, J. L. Chen, J. G. Li, and G.-N. Luo. Studies of the influence of external hydrocarbon injection on local plasma conditions and resulting carbon transport. 415:S270–S273, 2011.

Appendices

APPENDIX A

Manufacturing drawings of the injector head

THIRD ANGLE PROJECTION - DO NOT SCALE

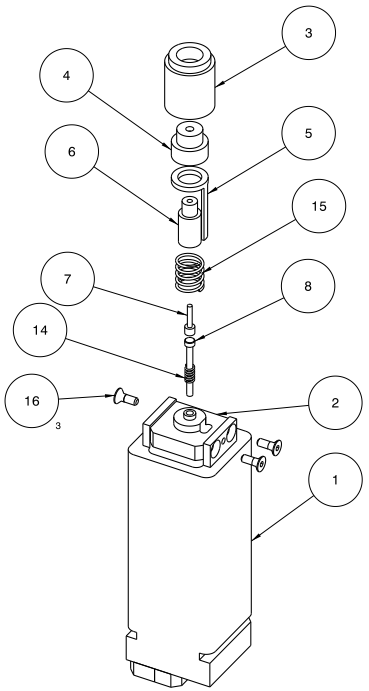

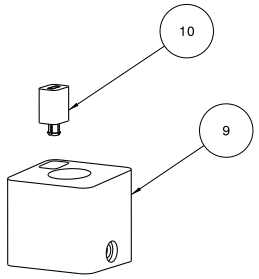

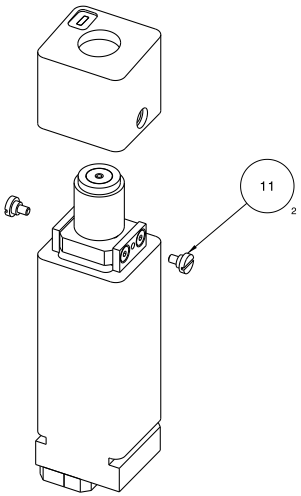

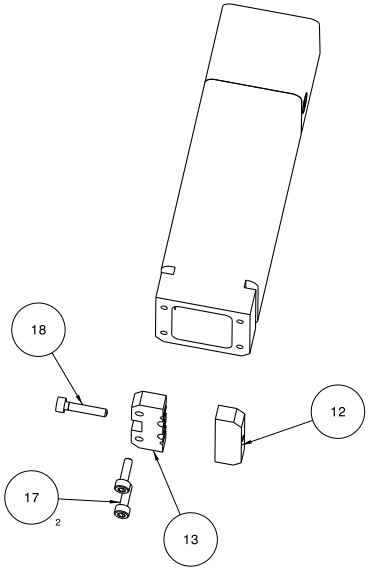

ITEM No.	PART No.	PART NAME	QTY
1	M11502061	BODY - RFEA PROBE	1
2	M11502076	BASE - SPARK PROBE	1
3	M11502072	OUTER ISOLATOR - SPARK PROBE	1
4	M11502073	OUTER ELECTRODE - SPARK PROBE	1
5	M11502078	OUTER CONNECTOR - SPARK PROBE	1
6	M11502074	INNER ISOLATOR - SPARK PROBE	1
7	M11502075	INNER ELECTRODE - SPARK PROBE	1
8	M11502077	INNER CONNECTOR - SPARK PROBE	1
9	M11502071	PROBE HEAD - SPARK PROBE	1
10	M11502080	LANGMUIR PROBE ASSEMBLY - SPARK PROBE	1
11	M11502066	SHOULDER SCREW - RFEA PROBE	2
12	M11502067	CLAMP BAR - RFEA PROBE	1
13	M11502079	CLAMP BLOCK - SPARK PROBE	1
14	JJCAF-0.6-3.7-6.5	COMPRESSION SPRING 0.6x3.7x6.5	1
15	JJCAF-0.96-10.67-12.7	COMPRESSION SPRING 0.96x10.67x12.7	1
16	JKCS-3-8	M3x8 HEX SOCKET C/SUNK HEAD SCREW	3
17	JKSS-3-10	M3x10 HEXAGON SOCKET HEAD CAP	2
18	JKSS-3-16	M3x16 HEX SOCKET HEAD CAP SCREW	1

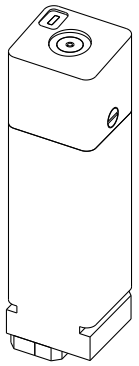

ISOMETRIC VIEW
NOT TO SCALE

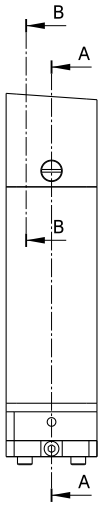

SECTION A-A

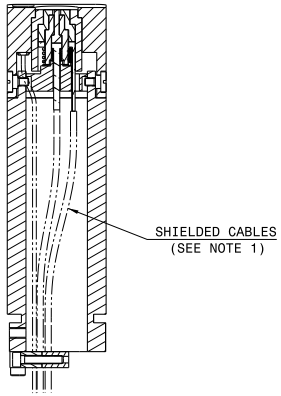

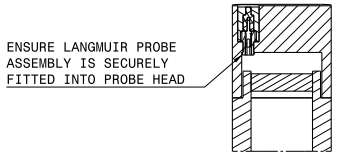

SECTION B-B

NOTES:

UNLESS OTHERWISE STATED THE FOLLOWING APPLY.

1. SHIELDED CABLED TO BE SPECIFIED BY RO AND FITTED ON ASSEMBLY.

UNLESS STATED IN NOTES ABOVE GENERAL TOLERANCE ISO 2768-mK

MATERIAL AND SPECIFICATION: SEE DRAWINGS

SURFACE TEXTURE UNLESS STATED: N/A

SURFACE TREATMENT: CLEAN

WEIGHT: 0.56 kg

INITIAL USE / REF DRAWING: (REFER TO SMARTEAM)

NOT TO BE MODIFIED BY HAND.
DIMENSIONS IN MILLIMETERS UNLESS STATED.

TECHNICAL CLASSIFICATIONS (FOR INTERNAL USE ONLY)

R/H	RAD.	VAC.	TRIT.

QUALITY CLASS

D.O. REF: DOI.067

ORIGINAL SCALE: 1:1

ISSUE	DATE	MODIFICATIONS/COMMENTS	DRN.BY	CHKD	APPD.	ECO. REF.
A	250311	FOR MANUFACTURE	IF	SB	RG	

United Kingdom Atomic Energy Authority

CCFE CULHAM CENTRE FOR FUSION ENERGY

TITLE: SPARK PROBE ASSEMBLY

DRG No: M11502070

CURRENT ISSUE: A

SHEET No 01 OF 01 SHEETS A1

THIRD ANGLE PROJECTION - DO NOT SCALE

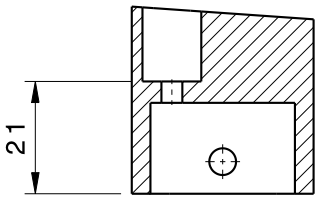

SECTION A-A

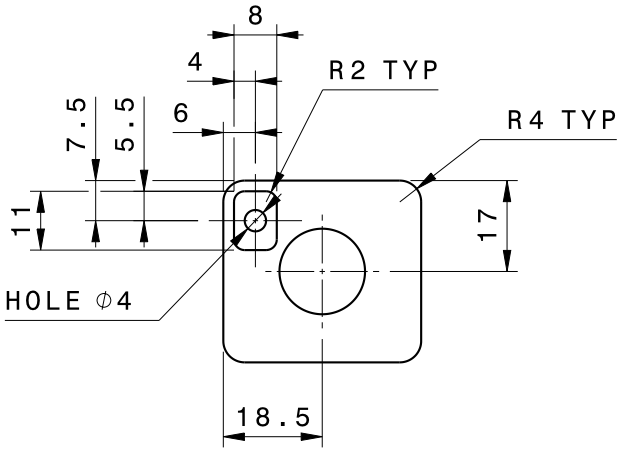

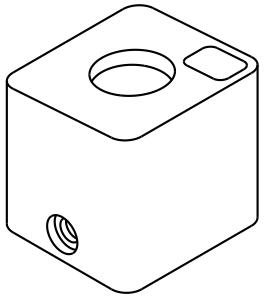

ISOMETRIC VIEW
NOT TO SCALE

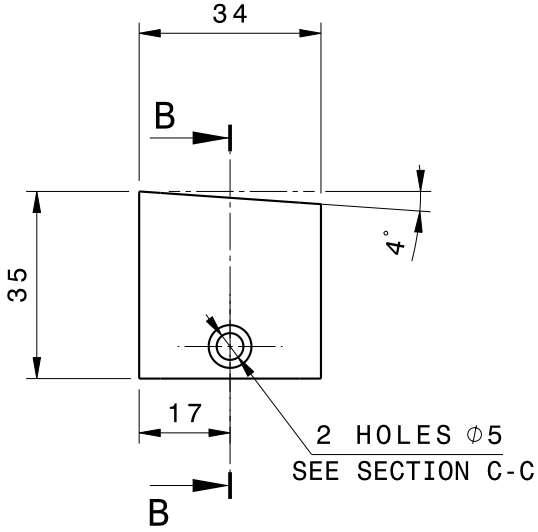

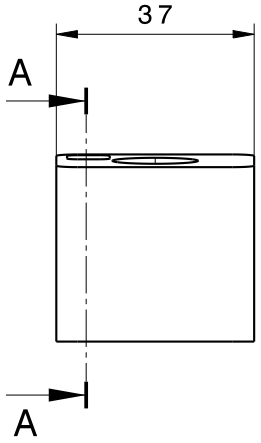

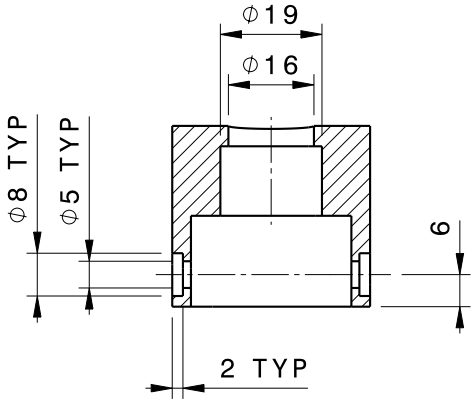

SECTION B-B

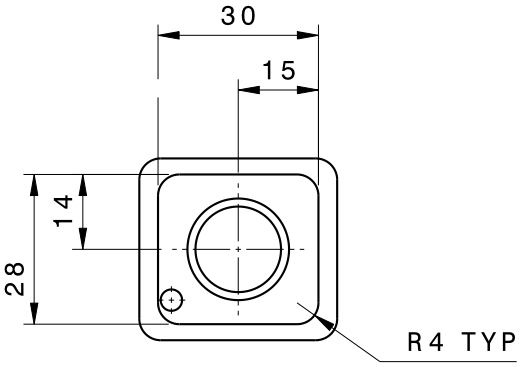

NOTES.

UNLESS OTHERWISE STATED THE FOLLOWING APPLY.

1. ALL CUT OR MACHINED SHARP EDGES TO BE DE-BURRED.

UNLESS STATED IN NOTES ABOVE GENERAL TOLERANCE ISO 2768-mK

A	250311	FOR MANUFACTURE	IF	SB	RG	ISO 1641
ISSUE	DATE	MODIFICATIONS/COMMENTS	DRN BY	CHKD	APPD	REF

MATERIAL AND SPECIFICATION: GRAPHITE

SURFACE TEXTURE UNLESS STATED: 3.2

SURFACE TREATMENT: CLEAN

WEIGHT: 0.04 kg

INITIAL USE / REF DRAWING: M11502070

(REFER TO SMARTEAM)

NOT TO BE MODIFIED BY HAND.
DIMENSIONS IN MILLIMETERS UNLESS STATED.

TECHNICAL CLASSIFICATIONS (FOR INTERNAL USE ONLY)

R/H	RAD.	VAC.	TRIT.

QUALITY CLASS

D.O. REF: DOI.067

ORIGINAL SCALE: 1:1

United Kingdom Atomic Energy Authority

CCFE CULHAM CENTRE FOR FUSION ENERGY

TITLE: PROBE HEAD - SPARK PROBE

DRG No: M11502071

CURRENT ISSUE: A

SHEET No 01 OF 01 SHEETS A3

THIRD ANGLE PROJECTION - DO NOT SCALE

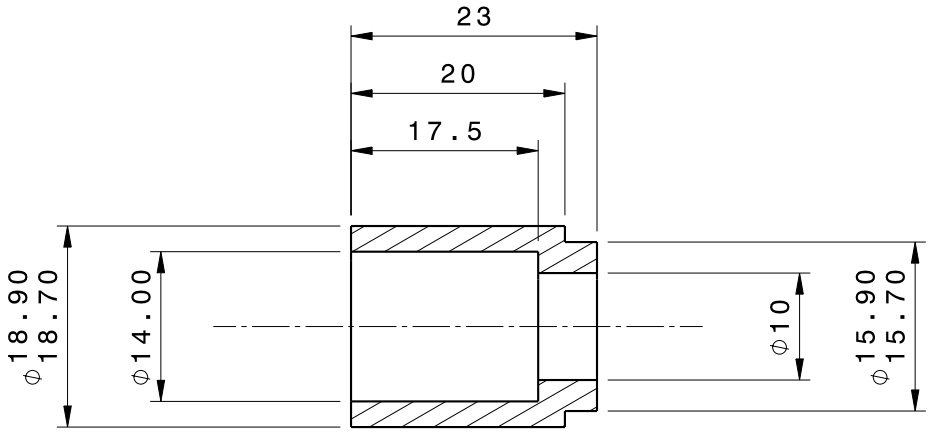

SECTION ON CENTRE LINE

ISOMETRIC VIEW
NOT TO SCALE

NOTES.

UNLESS OTHERWISE STATED THE FOLLOWING APPLY.

1. ALL CUT OR MACHINED SHARP EDGES TO BE DE-BURRED.

UNLESS STATED IN NOTES ABOVE GENERAL TOLERANCE ISO 2768-mK

MATERIAL AND SPECIFICATION
BORON NITRIDE XP

SURFACE TEXTURE UNLESS STATED
1.6

SURFACE TREATMENT
CLEAN

WEIGHT
0.01 kg

INITIAL USE / REF DRAWING
M11502070

(REFER TO SMARTEAM)

NOT TO BE MODIFIED BY HAND.
DIMENSIONS IN MILLIMETERS UNLESS STATED.

TECHNICAL CLASSIFICATIONS
(FOR INTERNAL USE ONLY)

R/H	RAD.	VAC.	TRIT.

QUALITY CLASS

D.O. REF: DOI.067
ORIGINAL SCALE: 2:1

ISSUE	DATE	MODIFICATIONS/COMMENTS	DRN BY	CHKD	APPD	ECO (MK7) REF
A	250311	FOR MANUFACTURE	IF	SB	RG	

United Kingdom Atomic Energy Authority
CCFE CULHAM CENTRE FOR FUSION ENERGY

TITLE
OUTER ISOLATOR - SPARK PROBE

DRG No: M11502072
CURRENT ISSUE: A

SHEET No 01 OF 01 SHEETS A3

THIRD ANGLE PROJECTION - DO NOT SCALE

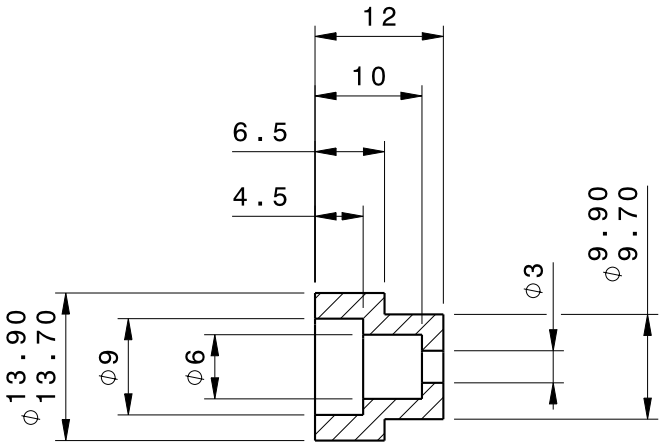

SECTION ON CENTRE LINE

ISOMETRIC VIEW

NOT TO SCALE

NOTES.

UNLESS OTHERWISE STATED THE FOLLOWING APPLY.

1. ALL CUT OR MACHINED SHARP EDGES TO BE DE-BURRED.

UNLESS STATED IN NOTES ABOVE GENERAL TOLERANCE ISO 2768-mK

MATERIAL AND SPECIFICATION: GRAPHITE

SURFACE TEXTURE UNLESS STATED

SURFACE TREATMENT: CLEAN

WEIGHT: 0.00 kg

INITIAL USE / REF DRAWING: M11502070 (REFER TO SMARTEAM)

NOT TO BE MODIFIED BY HAND. DIMENSIONS IN MILLIMETERS UNLESS STATED.

TECHNICAL CLASSIFICATIONS (FOR INTERNAL USE ONLY)

R/H	RAD.	VAC.	TRIT.

QUALITY CLASS

D.O. REF: DOI.067

ORIGINAL SCALE: 2:1

ISSUE	DATE	MODIFICATIONS/COMMENTS	DRN BY	CHKD	APPD	ECO (IMS) REF
A	250311	FOR MANUFACTURE	IF	SB	RG	

United Kingdom Atomic Energy Authority

CCFE CULHAM CENTRE FOR FUSION ENERGY

TITLE: OUTER ELECTRODE - SPARK PROBE

DRG No: M11502073

CURRENT ISSUE: A

SHEET No 01 OF 01 SHEETS A3

THIRD ANGLE PROJECTION - DO NOT SCALE

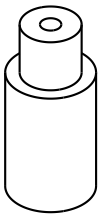

ISOMETRIC VIEW
NOT TO SCALE

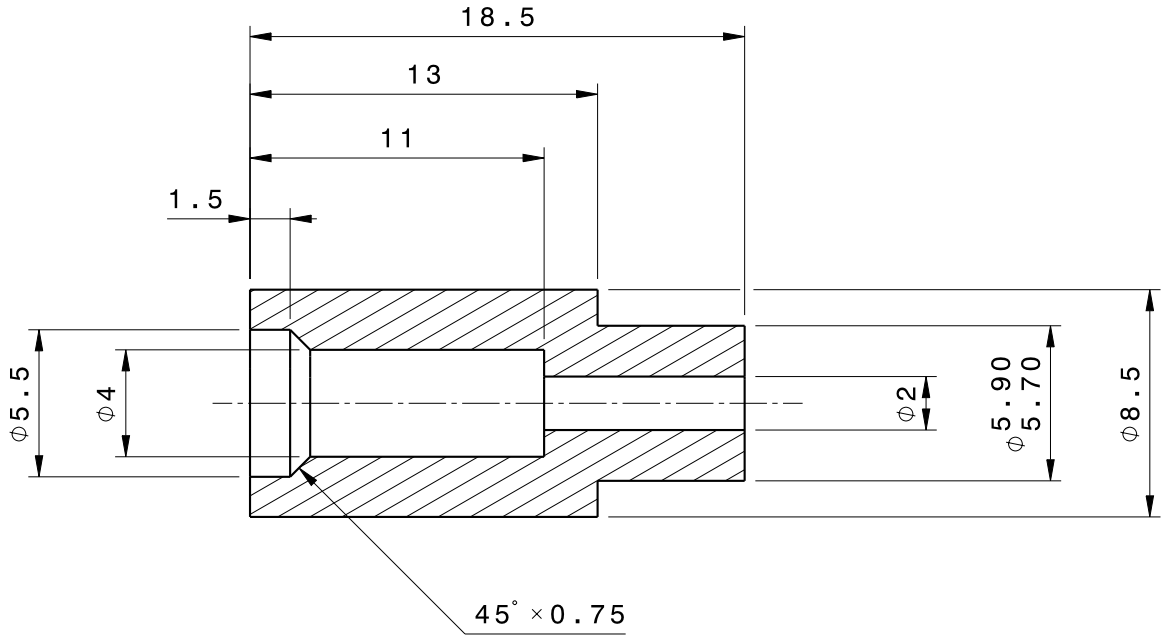

SECTION ON CENTRE LINE

NOTES.

UNLESS OTHERWISE STATED THE FOLLOWING APPLY.

1. ALL CUT OR MACHINED SHARP EDGES TO BE DE-BURRED.

UNLESS STATED IN NOTES ABOVE GENERAL TOLERANCE ISO 2768-mK

MATERIAL AND SPECIFICATION: BORON NITRIDE XP

SURFACE TEXTURE UNLESS STATED: 1.6

SURFACE TREATMENT: CLEAN

WEIGHT: 0.00 kg

INITIAL USE / REF DRAWING: M11502070 (REFER TO SMARTEAM)

NOT TO BE MODIFIED BY HAND. DIMENSIONS IN MILLIMETERS UNLESS STATED.

TECHNICAL CLASSIFICATIONS (FOR INTERNAL USE ONLY)

R/H	RAD.	VAC.	TRIT.

QUALITY CLASS

D.O. REF: DOI.067

ORIGINAL SCALE: 5:1

ISSUE	DATE	MODIFICATIONS/COMMENTS	DRN BY	CHKD	APPD	ECO (MK7) REF
A	250311	FOR MANUFACTURE	IF	SB	RG	

United Kingdom Atomic Energy Authority

CCFE CULHAM CENTRE FOR FUSION ENERGY

TITLE: INNER ISOLATOR - SPARK PROBE

DRG No: M11502074

CURRENT ISSUE: A

SHEET No 01 OF 01 SHEETS A3

THIRD ANGLE PROJECTION - DO NOT SCALE

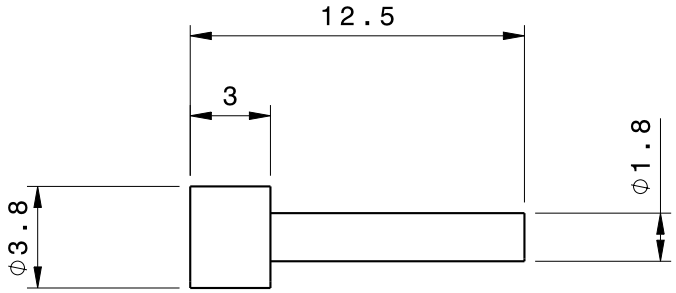

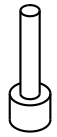

ISOMETRIC VIEW
NOT TO SCALE

NOTES.

UNLESS OTHERWISE STATED THE FOLLOWING APPLY.

1. ALL CUT OR MACHINED SHARP EDGES TO BE DE-BURRED.

UNLESS STATED IN NOTES ABOVE GENERAL TOLERANCE ISO 2768-mK

MATERIAL AND SPECIFICATION
GRAPHITE

SURFACE TEXTURE UNLESS STATED
N6

SURFACE TREATMENT
CLEAN

WEIGHT
0.00 kg

INITIAL USE / REF DRAWING
M11502070

(REFER TO SMARTEAM)

NOT TO BE MODIFIED BY HAND.
DIMENSIONS IN MILLIMETERS UNLESS STATED.

TECHNICAL CLASSIFICATIONS
(FOR INTERNAL USE ONLY)

R/H	RAD.	VAC.	TRIT.

QUALITY CLASS

D.O. REF

ORIGINAL SCALE
5:1

ISSUE	DATE	MODIFICATIONS/COMMENTS	DRN BY	CHKD	APPD	ECO (SAP)
A	250311	FOR MANUFACTURE	IF	SB	RG	

United Kingdom Atomic Energy Authority

CCFE
CULHAM CENTRE FOR FUSION ENERGY

TITLE
INNER ELECTRODE - SPARK PROBE

DRG No
M11502075

CURRENT ISSUE
A

SHEET No 01 OF 01 SHEETS A3

THIRD ANGLE PROJECTION - DO NOT SCALE

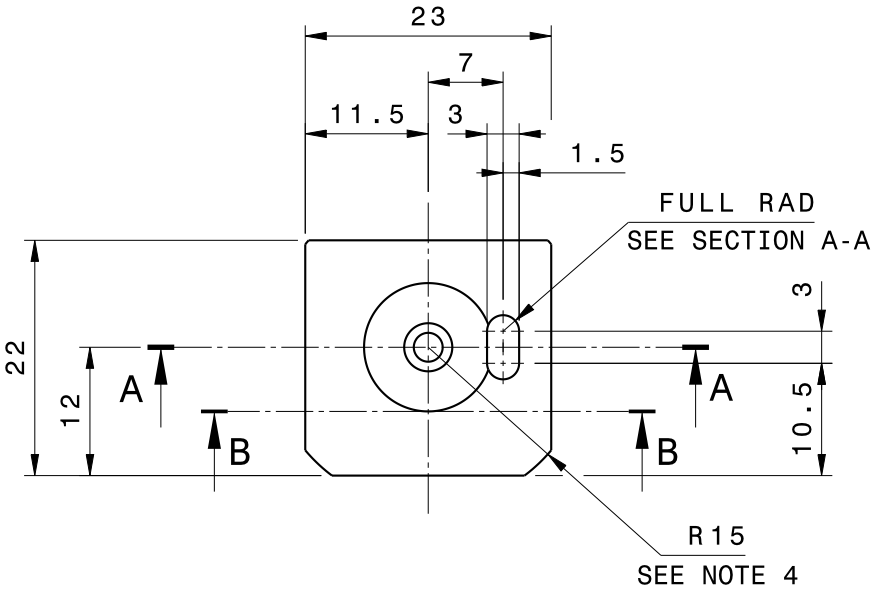

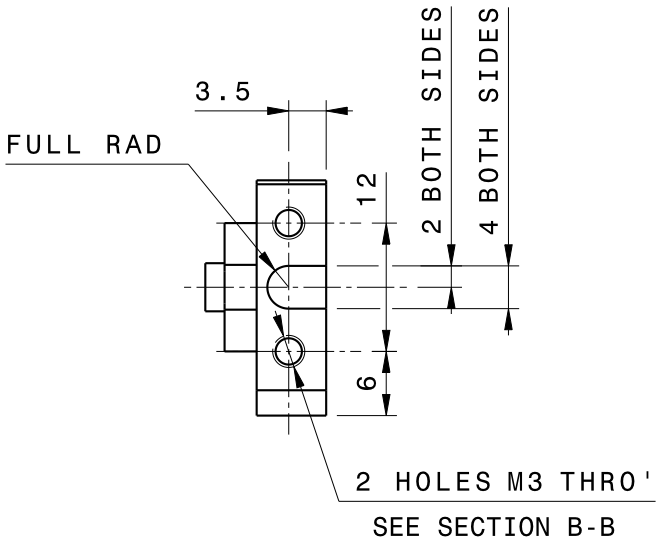

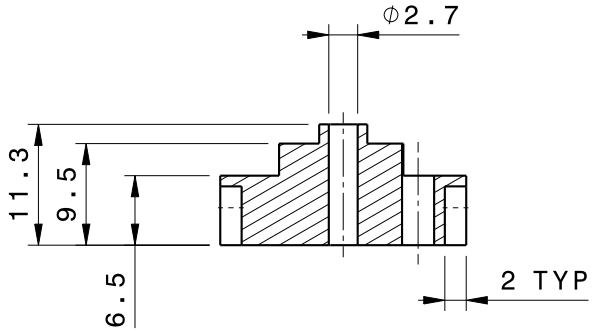

SECTION A-A

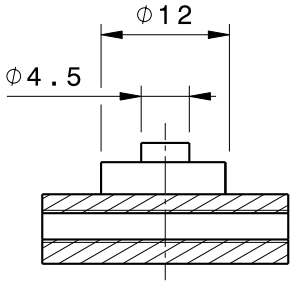

SECTION B-B

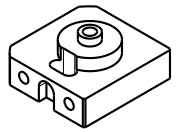

ISOMETRIC VIEW
NOT TO SCALE

NOTES.

UNLESS OTHERWISE STATED THE FOLLOWING APPLY.

1. ALL CUT OR MACHINED SHARP EDGES TO BE DE-BURRED.
2. ALL THREADS ARE METRIC COARSE SERIES 6H/6g (RIGHT HAND)
3. DIMENSION IN BRACKETS ARE FOR REFERENCE ONLY.
4. CAN BE MADE FROM Φ30 STOCK ROD.

UNLESS STATED IN NOTES ABOVE GENERAL TOLERANCE ISO 2768-mK

MATERIAL AND SPECIFICATION	PEEK 1000
SURFACE TEXTURE UNLESS STATED	1.6
SURFACE TREATMENT	CLEAN
WEIGHT	0.00 kg
INITIAL USE / REF DRAWING	M11502070 (REFER TO SMARTEAM)
	NOT TO BE MODIFIED BY HAND. DIMENSIONS IN MILLIMETERS UNLESS STATED.
TECHNICAL CLASSIFICATIONS (FOR INTERNAL USE ONLY)	R/H, RAD., VAC., TRIT.
QUALITY CLASS	
D.O. REF	DOI.067
ORIGINAL SCALE	2:1

ISSUE	DATE	MODIFICATIONS/COMMENTS	DRN BY	CHKD	APPD	ECO (MK7) REF
A	250311	FOR MANUFACTURE	IF	SB	RG	

United Kingdom Atomic Energy Authority — CCFE CULHAM CENTRE FOR FUSION ENERGY

TITLE: BASE - SPARK PROBE

DRG No: M11502076 — CURRENT ISSUE: A

SHEET No 01 OF 01 SHEETS A3

THIRD ANGLE PROJECTION - DO NOT SCALE

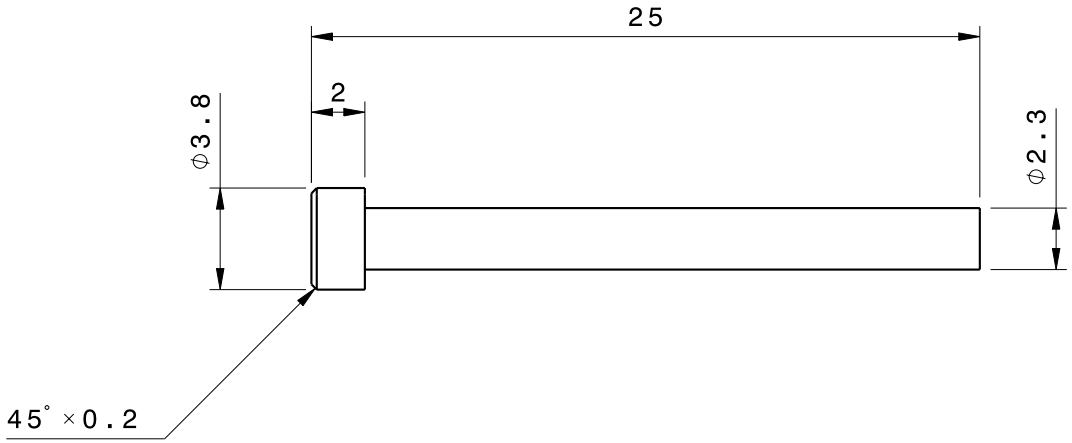

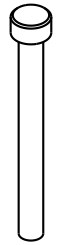

ISOMETRIC VIEW
NOT TO SCALE

NOTES.

UNLESS OTHERWISE STATED THE FOLLOWING APPLY.

1. ALL CUT OR MACHINED SHARP EDGES TO BE DE-BURRED.

UNLESS STATED IN NOTES ABOVE GENERAL TOLERANCE ISO 2768-mK

A	250311	FOR MANUFACTURE	IF	SB	RG	ISO 1641	
ISSUE	DATE	MODIFICATIONS/COMMENTS	DRN BY	CHKD	APPD	REF	

MATERIAL AND SPECIFICATION: COPPER Cr Zr

SURFACE TEXTURE UNLESS STATED: 3.2

SURFACE TREATMENT: CLEAN

WEIGHT: 0.00 kg

INITIAL USE / REF DRAWING: M11502070 (REFER TO SMARTEAM)

NOT TO BE MODIFIED BY HAND. DIMENSIONS IN MILLIMETERS UNLESS STATED.

TECHNICAL CLASSIFICATIONS (FOR INTERNAL USE ONLY)

R/H	RAD.	VAC.	TRIT.

QUALITY CLASS

D.O. REF: DOI.067

ORIGINAL SCALE: 5:1

United Kingdom Atomic Energy Authority

CCFE CULHAM CENTRE FOR FUSION ENERGY

TITLE: INNER CONNECTOR - SPARK PROBE

DRG No: M11502077

CURRENT ISSUE: A

SHEET No 01 OF 01 SHEETS A3

THIRD ANGLE PROJECTION - DO NOT SCALE

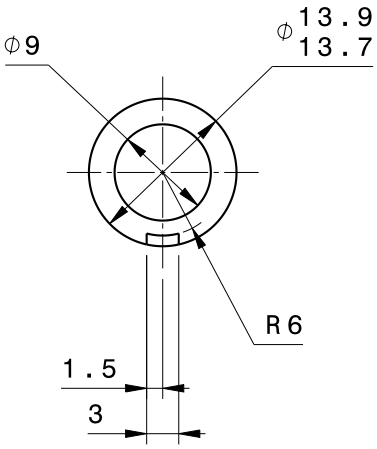

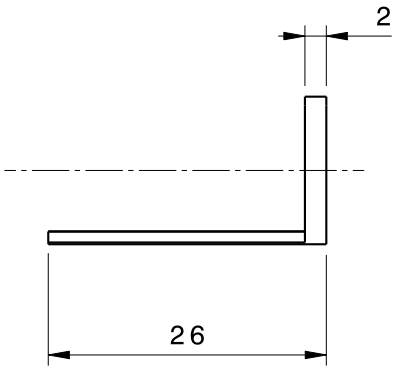

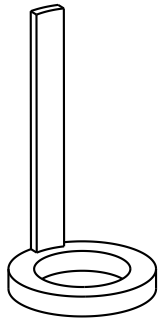

ISOMETRIC VIEW
NOT TO SCALE

NOTES.

UNLESS OTHERWISE STATED THE FOLLOWING APPLY.

1. ALL CUT OR MACHINED SHARP EDGES TO BE DE-BURRED.

UNLESS STATED IN NOTES ABOVE GENERAL TOLERANCE ISO 2768-mK

MATERIAL AND SPECIFICATION
COPPER Cr Zr

SURFACE TEXTURE UNLESS STATED
3.2

SURFACE TREATMENT
CLEAN

WEIGHT
0.00 kg

INITIAL USE / REF DRAWING
M11502070
(REFER TO SMARTEAM)

NOT TO BE MODIFIED BY HAND.
DIMENSIONS IN MILLIMETERS UNLESS STATED.

TECHNICAL CLASSIFICATIONS
(FOR INTERNAL USE ONLY)

R/H	RAD.	VAC.	TRIT.

QUALITY CLASS

D.O. REF: DOI.067
ORIGINAL SCALE: 2:1

ISSUE	DATE	MODIFICATIONS/COMMENTS	DRN BY	CHKD	APPD	ECO No.
A	250311	FOR MANUFACTURE	IF	SB	RG	

United Kingdom Atomic Energy Authority

CCFE CULHAM CENTRE FOR FUSION ENERGY

TITLE
OUTER CONNECTOR - SPARK PROBE

DRG No: M11502078

CURRENT ISSUE: A

SHEET No 01 OF 01 SHEETS A3

THIRD ANGLE PROJECTION - DO NOT SCALE

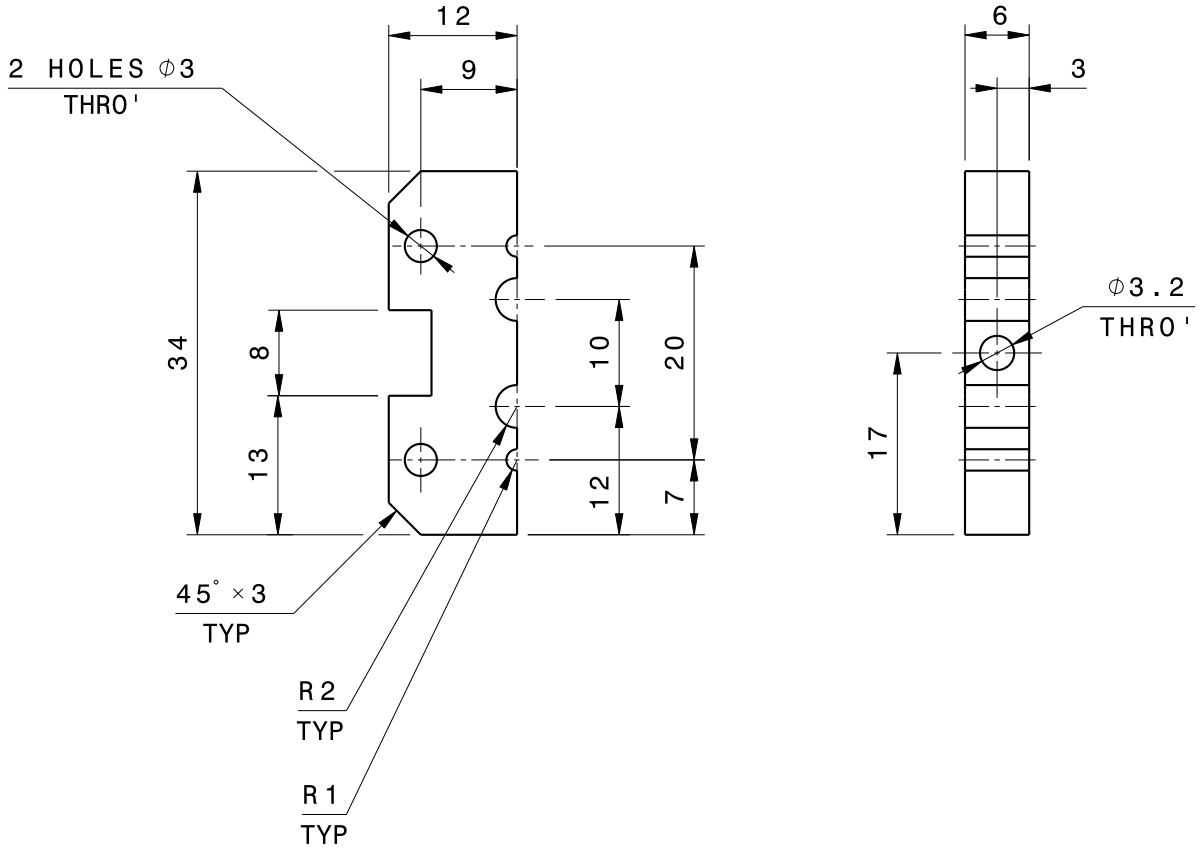

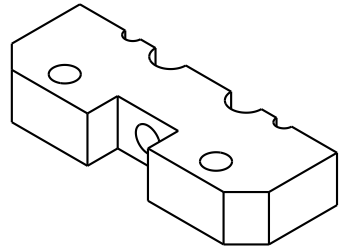

ISOMETRIC VIEW
NOT TO SCALE

NOTES.

UNLESS OTHERWISE STATED THE FOLLOWING APPLY.

1. ALL CUT OR MACHINED SHARP EDGES TO BE DE-BURRED.

UNLESS STATED IN NOTES ABOVE GENERAL TOLERANCE ISO 2768-mK

MATERIAL AND SPECIFICATION	PEEK 1000
SURFACE TEXTURE UNLESS STATED	1.6
SURFACE TREATMENT	CLEAN
WEIGHT	0.00 kg
INITIAL USE / REF DRAWING	M11502070 (REFER TO SMARTEAM)
NOT TO BE MODIFIED BY HAND. DIMENSIONS IN MILLIMETERS UNLESS STATED.	
TECHNICAL CLASSIFICATIONS (FOR INTERNAL USE ONLY)	R/H, RAD., VAC., TRIT.
QUALITY CLASS	
D.O. REF	DOI.067
ORIGINAL SCALE	2:1

ISSUE	DATE	MODIFICATIONS/COMMENTS	DRN BY	CHKD	APPD	ECO (SAP) REF
A	250311	FOR MANUFACTURE	IF	SB	RG	

United Kingdom Atomic Energy Authority

CCFE CULHAM CENTRE FOR FUSION ENERGY

TITLE: CLAMP BLOCK - SPARK PROBE

DRG No: M11502079

CURRENT ISSUE: A

SHEET No 01 OF 01 SHEETS A3

THIRD ANGLE PROJECTION - DO NOT SCALE

ITEM No.	PART No.	PART NAME	Qty
1	M11502081	ISOLATOR - LP - SPARK PROBE	1
2	M11502082	PROBE TIP - LP - SPARK PROBE	1
3	M11502083	RETAINER - LP - SPARK PROBE	1
4	M11502084	CONNECTOR PIN - LP - SPARK PROBE	1

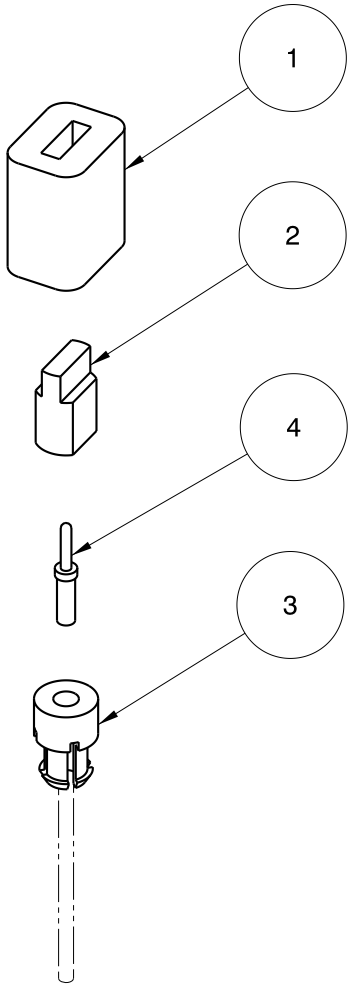

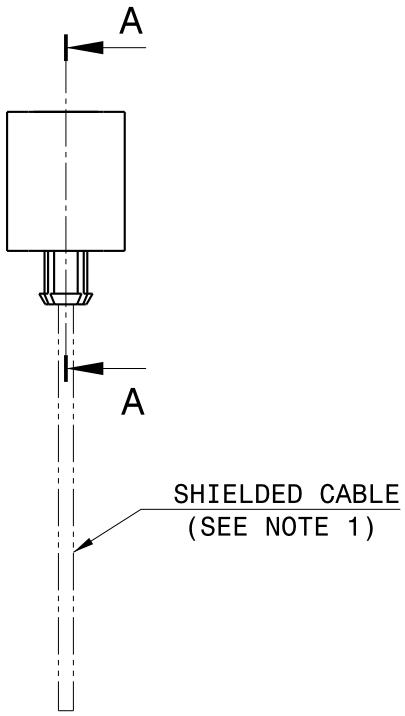

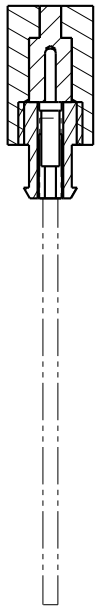

SECTION A-A

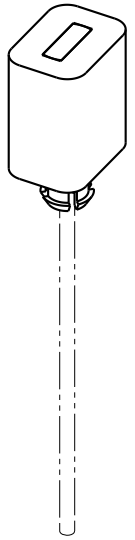

ISOMETRIC VIEW
NOT TO SCALE

NOTES:

UNLESS SPECIFIED OTHERWISE THE FOLLOWING APPLY.

1. SHIELDED CABLE TO BE SPECIFIED BY RO AND FITTED ON ASSEMBLY.

UNLESS STATED IN NOTES ABOVE GENERAL TOLERANCE ISO 2768-mK

MATERIAL AND SPECIFICATION: SEE DRAWINGS

SURFACE TEXTURE UNLESS STATED: N/A

SURFACE TREATMENT: CLEAN

WEIGHT: 0.00 kg

INITIAL USE / REF DRAWING: M11502070 (REFER TO SMARTEAM)

NOT TO BE MODIFIED BY HAND. DIMENSIONS IN MILLIMETERS UNLESS STATED.

TECHNICAL CLASSIFICATIONS (FOR INTERNAL USE ONLY)

R/H	RAD.	VAC.	TRIT.

QUALITY CLASS

D.O. REF: DOI.067

ORIGINAL SCALE: 2:1

ISSUE	DATE	MODIFICATIONS/COMMENTS	DRN BY	CHKD	APPD	REF.
A	250311	FOR MANUFACTURE	IF	SB	RG	ECO 1947

United Kingdom Atomic Energy Authority

CCFE CULHAM CENTRE FOR FUSION ENERGY

TITLE: LANGMUIR PROBE ASSY - SPARK PROBE

DRG No: M11502080

CURRENT ISSUE: B.0

SHEET No 01 OF 01 SHEETS A3

THIRD ANGLE PROJECTION - DO NOT SCALE

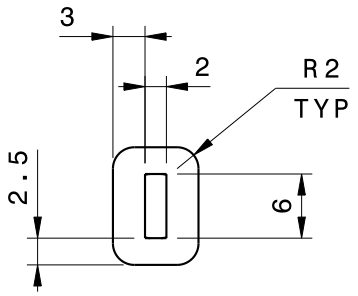

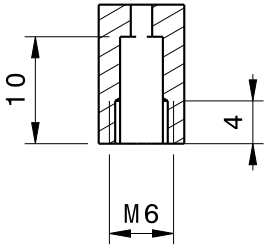

SECTION B-B

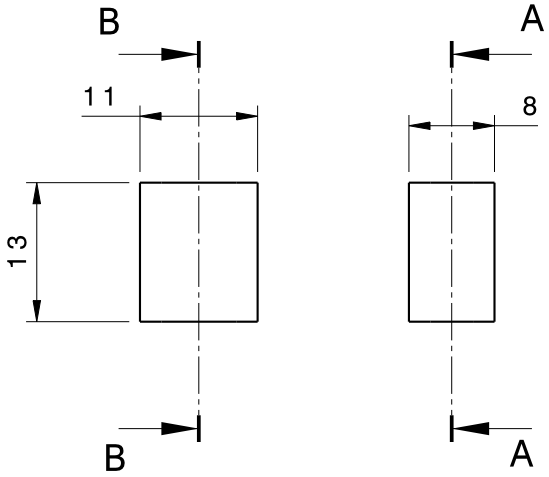

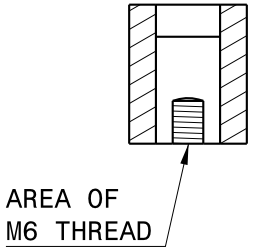

SECTION A-A

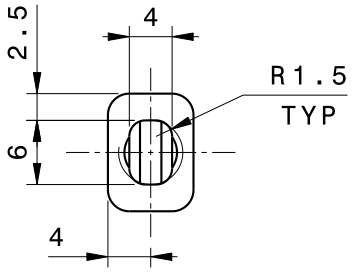

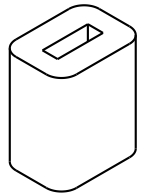

ISOMETRIC VIEW
NOT TO SCALE

NOTES.

UNLESS OTHERWISE STATED THE FOLLOWING APPLY.

1. ALL CUT OR MACHINED SHARP EDGES TO BE DE-BURRED.

UNLESS STATED IN NOTES ABOVE GENERAL TOLERANCE ISO 2768-mK

A	250311	FOR MANUFACTURE	IF	SB	RG	ISO 1641
ISSUE	DATE	MODIFICATIONS/COMMENTS	DRN BY	CHKD	APPD	REF

MATERIAL AND SPECIFICATION: BORON NITRIDE XP

SURFACE TEXTURE UNLESS STATED: 1.6

SURFACE TREATMENT: CLEAN

WEIGHT: 0.00 kg

INITIAL USE / REF DRAWING: M11502080

(REFER TO SMARTEAM)

NOT TO BE MODIFIED BY HAND.
DIMENSIONS IN MILLIMETERS UNLESS STATED.

TECHNICAL CLASSIFICATIONS (FOR INTERNAL USE ONLY)

R/H	RAD.	VAC.	TRIT.

QUALITY CLASS

D.O. REF: DOI.067

ORIGINAL SCALE: 2:1

United Kingdom Atomic Energy Authority

CCFE CULHAM CENTRE FOR FUSION ENERGY

TITLE: ISOLATOR - LP - SPARK PROBE

DRG No: M11502081

CURRENT ISSUE: A

SHEET No 01 OF 01 SHEETS A3

THIRD ANGLE PROJECTION - DO NOT SCALE

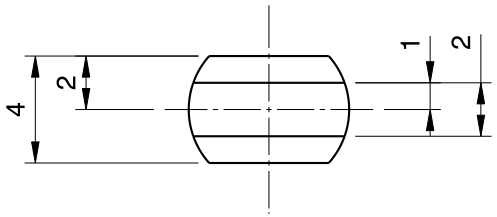

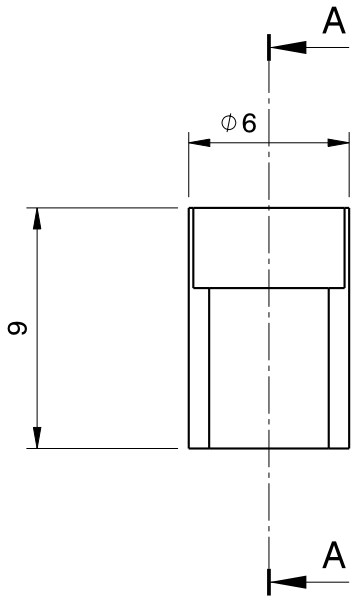

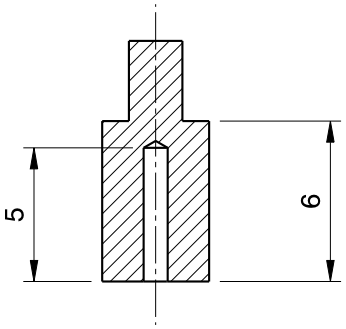

SECTION A-A

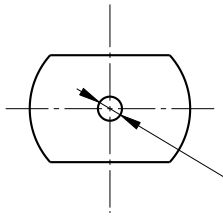

HOLE ϕ0.9
SEE SECTION A-A

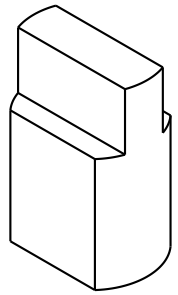

ISOMETRIC VIEW
NOT TO SCALE

NOTES.

UNLESS OTHERWISE STATED THE FOLLOWING APPLY.

1. ALL CUT OR MACHINED SHARP EDGES TO BE DE-BURRED.

UNLESS STATED IN NOTES ABOVE GENERAL TOLERANCE ISO 2768-mK

MATERIAL AND SPECIFICATION	GRAPHITE
SURFACE TEXTURE UNLESS STATED	1.6
SURFACE TREATMENT	CLEAN
WEIGHT	0.00 kg
INITIAL USE / REF DRAWING	M11502080 (REFER TO SMARTEAM)
NOT TO BE MODIFIED BY HAND. DIMENSIONS IN MILLIMETERS UNLESS STATED.	
TECHNICAL CLASSIFICATIONS (FOR INTERNAL USE ONLY)	R/H, RAD., VAC., TRIT.
QUALITY CLASS	
D.O. REF	DOI.67
ORIGINAL SCALE	5:1

ISSUE	DATE	MODIFICATIONS/COMMENTS	DRN BY	CHKD	APPD	REF.
A	250311	FOR MANUFACTURE	IF	sb	RG	ISO 1641

United Kingdom Atomic Energy Authority

CCFE CULHAM CENTRE FOR FUSION ENERGY

TITLE: PROBE TIP - LP - SPARK PROBE

DRG No: M11502082

CURRENT ISSUE: A

SHEET No 01 OF 01 SHEETS A3

THIRD ANGLE PROJECTION - DO NOT SCALE

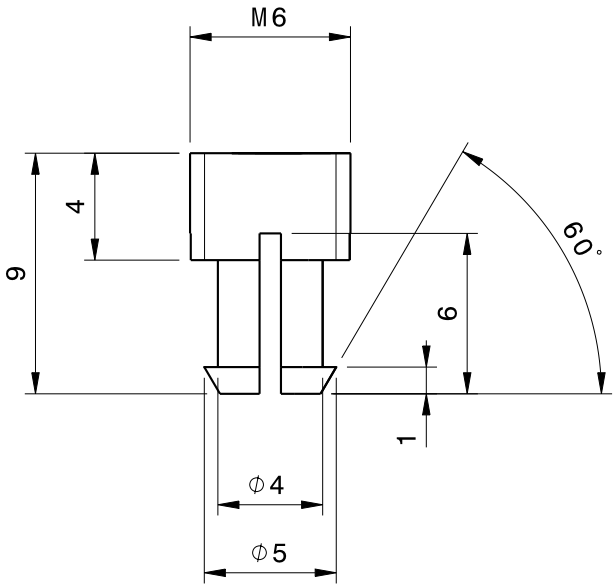

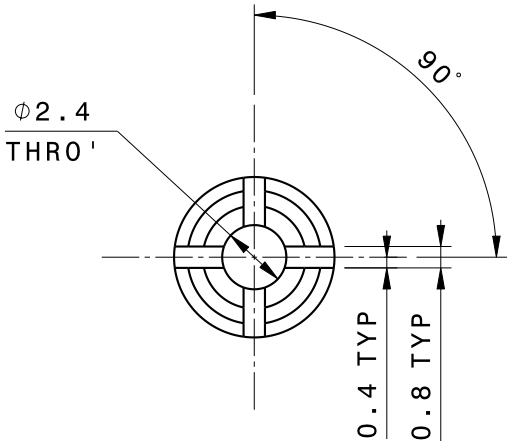

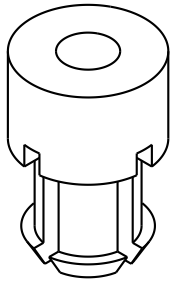

ISOMETRIC VIEW
NOT TO SCALE

NOTES.

UNLESS OTHERWISE STATED THE FOLLOWING APPLY.

1. ALL CUT OR MACHINED SHARP EDGES TO BE DE-BURRED.

UNLESS STATED IN NOTES ABOVE GENERAL TOLERANCE ISO 2768-mK

MATERIAL AND SPECIFICATION	PEEK 1000
SURFACE TEXTURE UNLESS STATED	3.2
SURFACE TREATMENT	CLEAN
WEIGHT	0.00 kg
INITIAL USE / REF DRAWING	M11502083 (REFER TO SMARTEAM)
	NOT TO BE MODIFIED BY HAND. DIMENSIONS IN MILLIMETERS UNLESS STATED.
TECHNICAL CLASSIFICATIONS (FOR INTERNAL USE ONLY)	R/H, RAD., VAC., TRIT.
QUALITY CLASS	
D.O. REF	DOI.067
ORIGINAL SCALE	5:1

ISSUE	DATE	MODIFICATIONS/COMMENTS	DRN BY	CHKD	APPD	ECO (MK7) REF
A	250311	FOR MANUFACTURE	IF	SB	RG	

United Kingdom Atomic Energy Authority

CCFE CULHAM CENTRE FOR FUSION ENERGY

TITLE: RETAINER - LP - SPARK PROBE

DRG No: M11502083

CURRENT ISSUE: A

SHEET No 01 OF 01 SHEETS A3

THIRD ANGLE PROJECTION - DO NOT SCALE

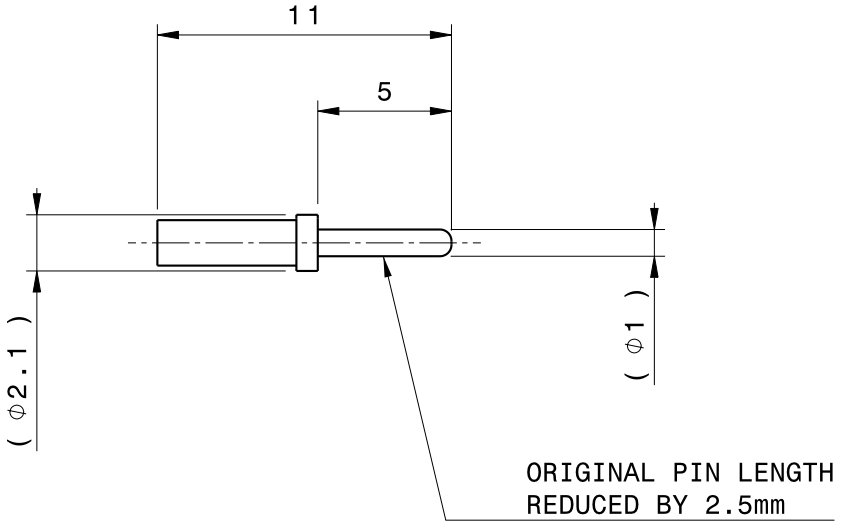

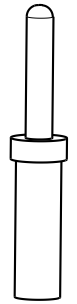

ISOMETRIC VIEW
NOT TO SCALE

NOTES.

UNLESS OTHERWISE STATED THE FOLLOWING APPLY.

1. ALL CUT OR MACHINED SHARP EDGES TO BE DE-BURRED.

2. Made from - CABURN Pt No 1510101 Contact ref:- DPINMC

UNLESS STATED IN NOTES ABOVE GENERAL TOLERANCE ISO 2768-mK

MATERIAL AND SPECIFICATION: SEE DRAWING

SURFACE TEXTURE UNLESS STATED: 1.6

SURFACE TREATMENT: CLEAN

WEIGHT: 0.00 kg

INITIAL USE / REF DRAWING: M11502080 (REFER TO SMARTEAM)

NOT TO BE MODIFIED BY HAND. DIMENSIONS IN MILLIMETERS UNLESS STATED.

TECHNICAL CLASSIFICATIONS (FOR INTERNAL USE ONLY)

R/H	RAD.	VAC.	TRIT.

QUALITY CLASS

D.O. REF: DOI.067

ORIGINAL SCALE: 5:1

ISSUE	DATE	MODIFICATIONS/COMMENTS	DRN BY	CHKD	APPD	ECO No.
A	250311	FOR MANUFACTURE	IF	SB	RG	

United Kingdom Atomic Energy Authority

CCFE CULHAM CENTRE FOR FUSION ENERGY

TITLE: CONNECTOR PIN - LP - SPARK PROBE

DRG No: M11502084

CURRENT ISSUE: A

SHEET No 01 OF 01 SHEETS A3

APPENDIX B

Electrical schematics of the MAST installation

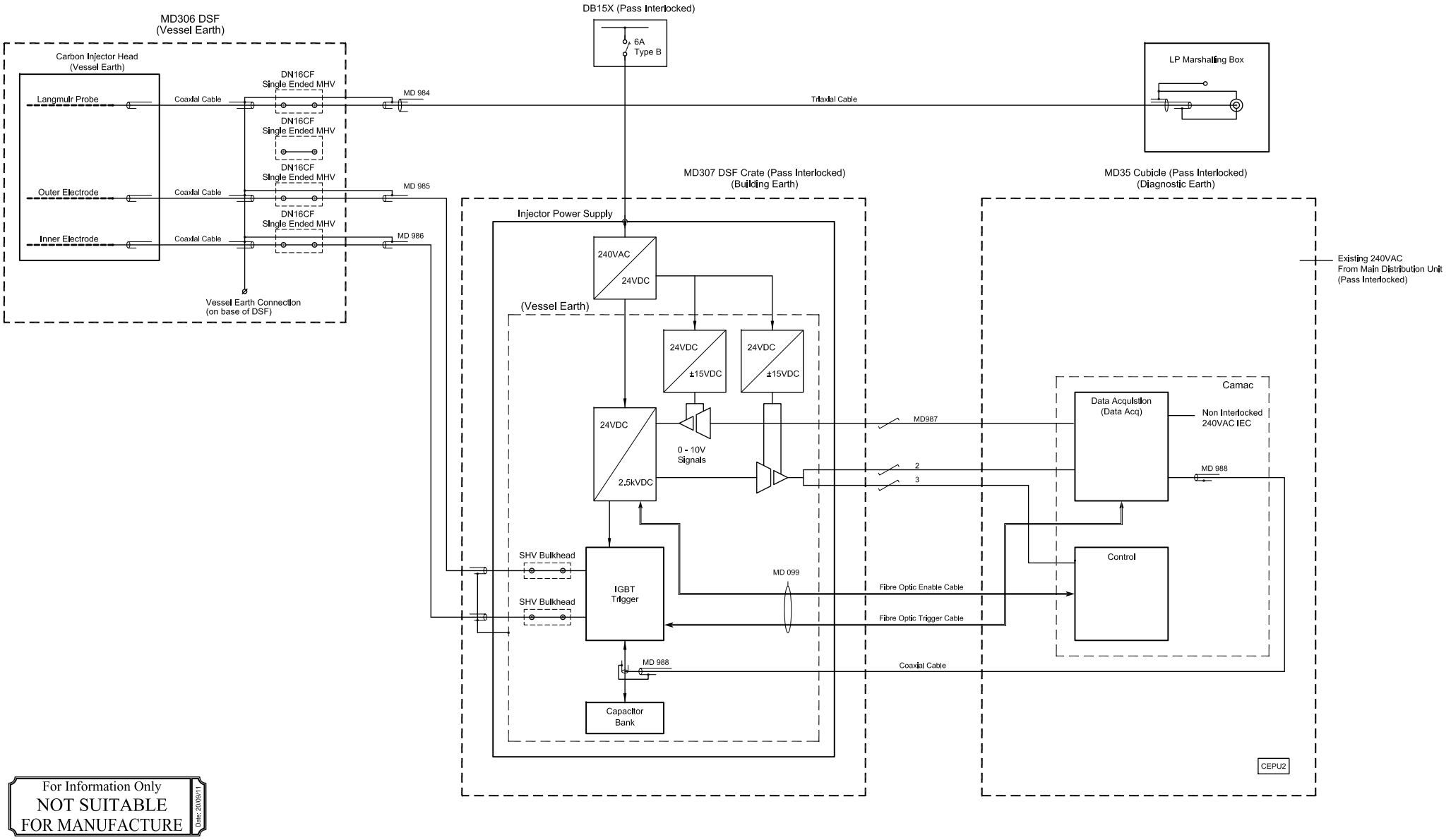

For Information Only
NOT SUITABLE
FOR MANUFACTURE
Date: 20/09/11

Issue	Date	Status/Modification	Drawn	Checked	Approved	Mod. No.
A	18/03/11	ORIGINAL	YLA			

Document created using * AutoCAD * Do not modify by hand

Dimensions in mm unless otherwise stated

Reference Drawing:

THIS DOCUMENT PRINTED : Date: 20/09/11 Time: 11:26 Hrs.

Assembly Procedure:

CADfile: M11502101

TITLE:

DSF
Connection Diagram
Sparker Schematic

United Kingdom Atomic Energy Authority

CCFE
CULHAM CENTRE FOR FUSION ENERGY

DWG. No. M115-02-101 Issue A

Quality Class: 3 Sheet No. 1 of 1 Sheets A3

Ref: EDS-A3L/JET/170107/mlv

FIRST ANGLE PROJECTION — DO NOT SCALE

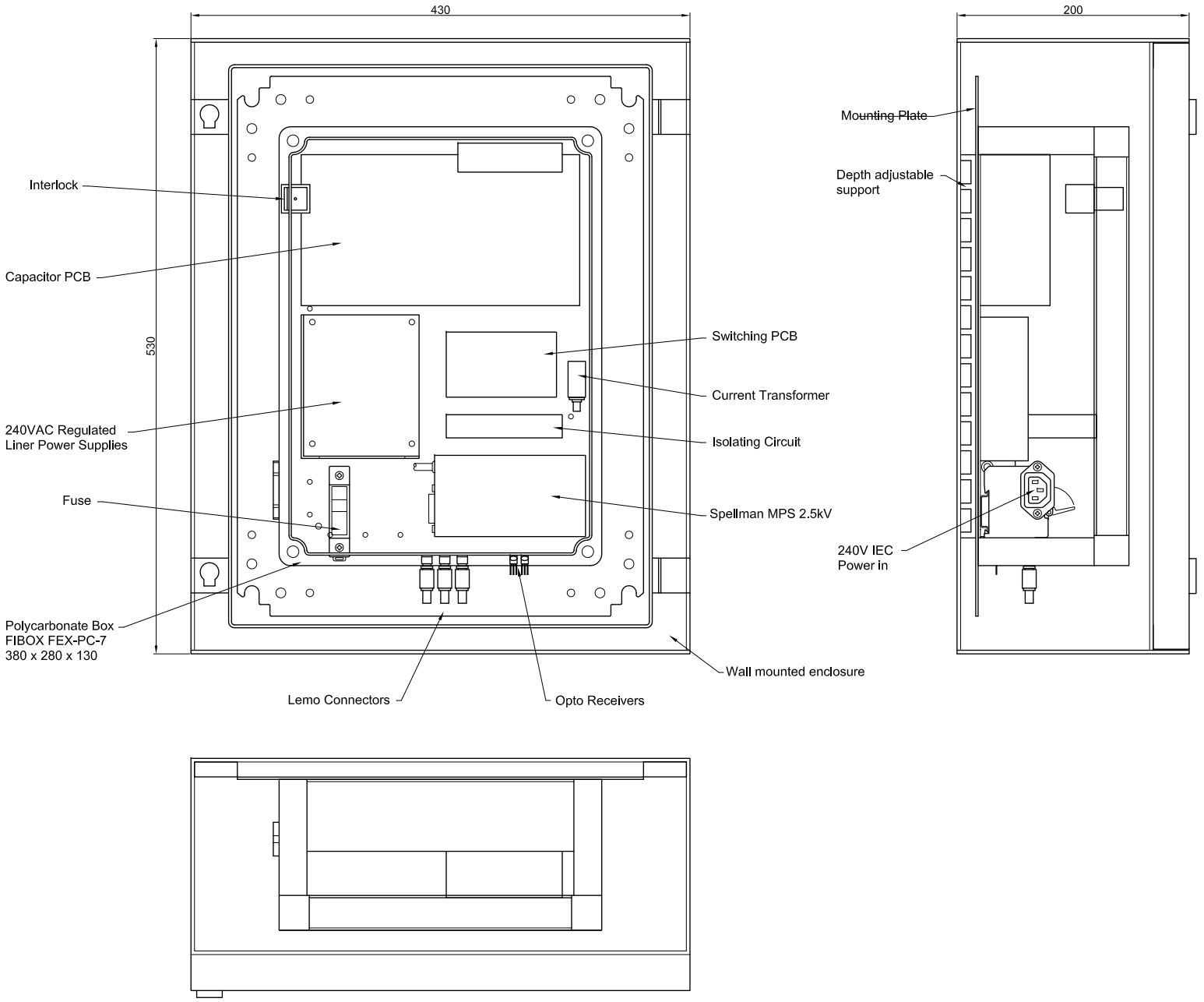

For Information Only
NOT SUITABLE
FOR MANUFACTURE
Date: 22/09/11

Issue	Date	Status/Modification	Drawn	Checked	Approved	Mod. No.
A	13/05/11	ORIGINAL	YLA			

Document created using * AutoCAD * Do not modify by hand

NOT FOR PUBLICATION
This Document shall not without prior written consent from CCFE be copied in whole or in part or used for any purpose other than that for which it is supplied

Dimensions in mm unless otherwise stated
THIS DOCUMENT PRINTED: Date: 22/09/11 Time: 15:16 Hrs.
Reference Drawing:
Assembly Procedure:
CADfile: M11502102

TITLE:
DSF Sparker
Cubicle General Layout

United Kingdom Atomic Energy Authority
CCFE CULHAM CENTRE for FUSION ENERGY

DWG. No. M115-02-102 Issue A
Quality Class: 4 Sheet No. 1 of 1 Sheets A1

Ref: EDS-ATL/JET/170107/mlv

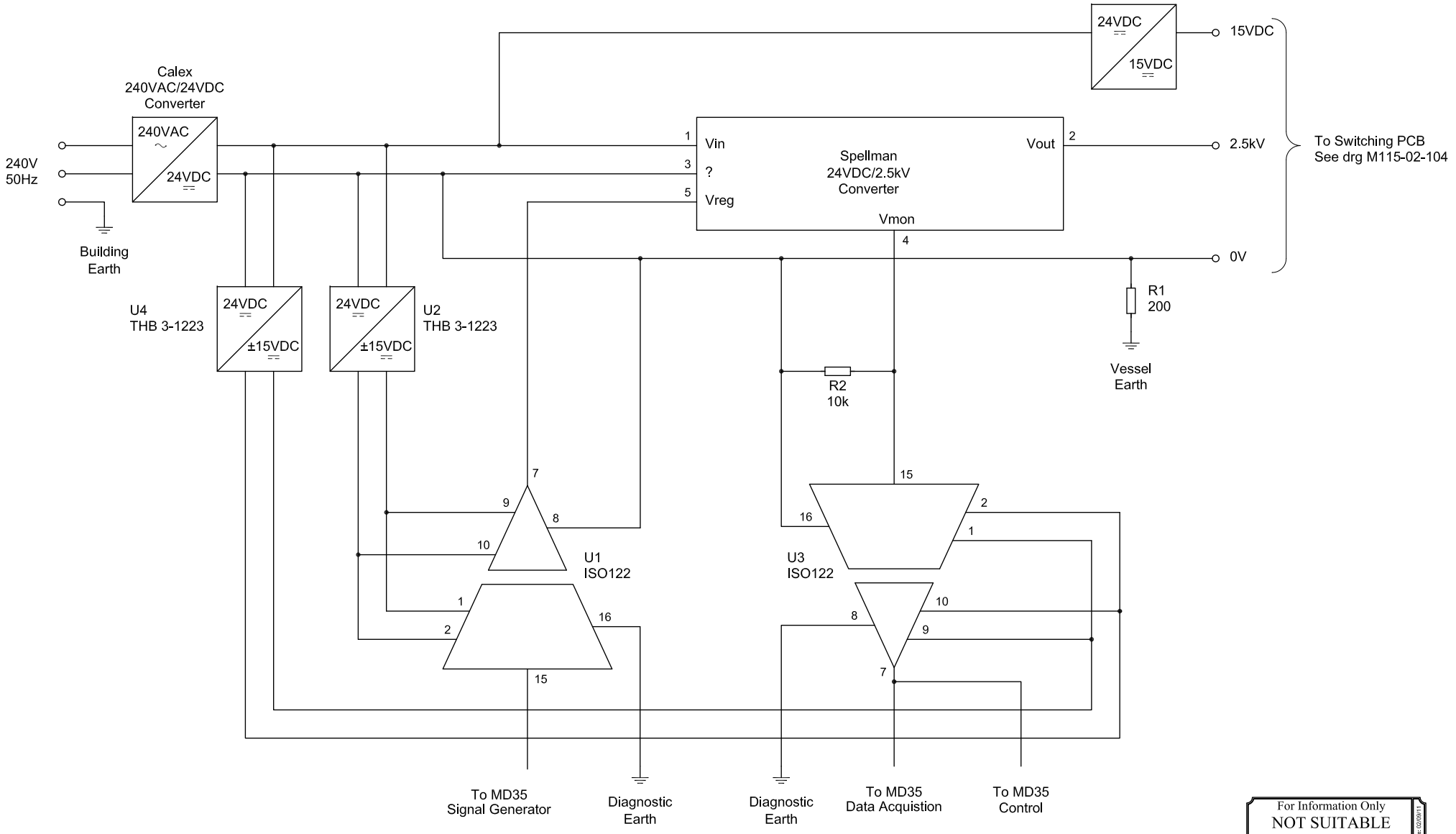

For Information Only
NOT SUITABLE
FOR MANUFACTURE
Date: 02/09/11

Document created using
* AutoCAD *
Do not modify by hand

Issue	Date	Status/Modification	Drawn	Checked	Approved	Mod. No.
A	17/06/11	ORIGINAL	YLA			

Dimensions in mm unless otherwise stated
Reference Drawing:
THIS DOCUMENT PRINTED : Date: 02/09/11 Time: 15:05 Hrs.
Assembly Procedure:
CADfile: M11502103

TITLE:
DSF Sparker
Wiring Diagram

United Kingdom Atomic Energy Authority
CCFE CULHAM CENTRE FOR FUSION ENERGY

DWG. No. M115-02-103 Issue A
Quality Class: 4 Sheet No. 1 of 1 Sheets A3

Ref: EDS-A3L/JET/170107/mlv

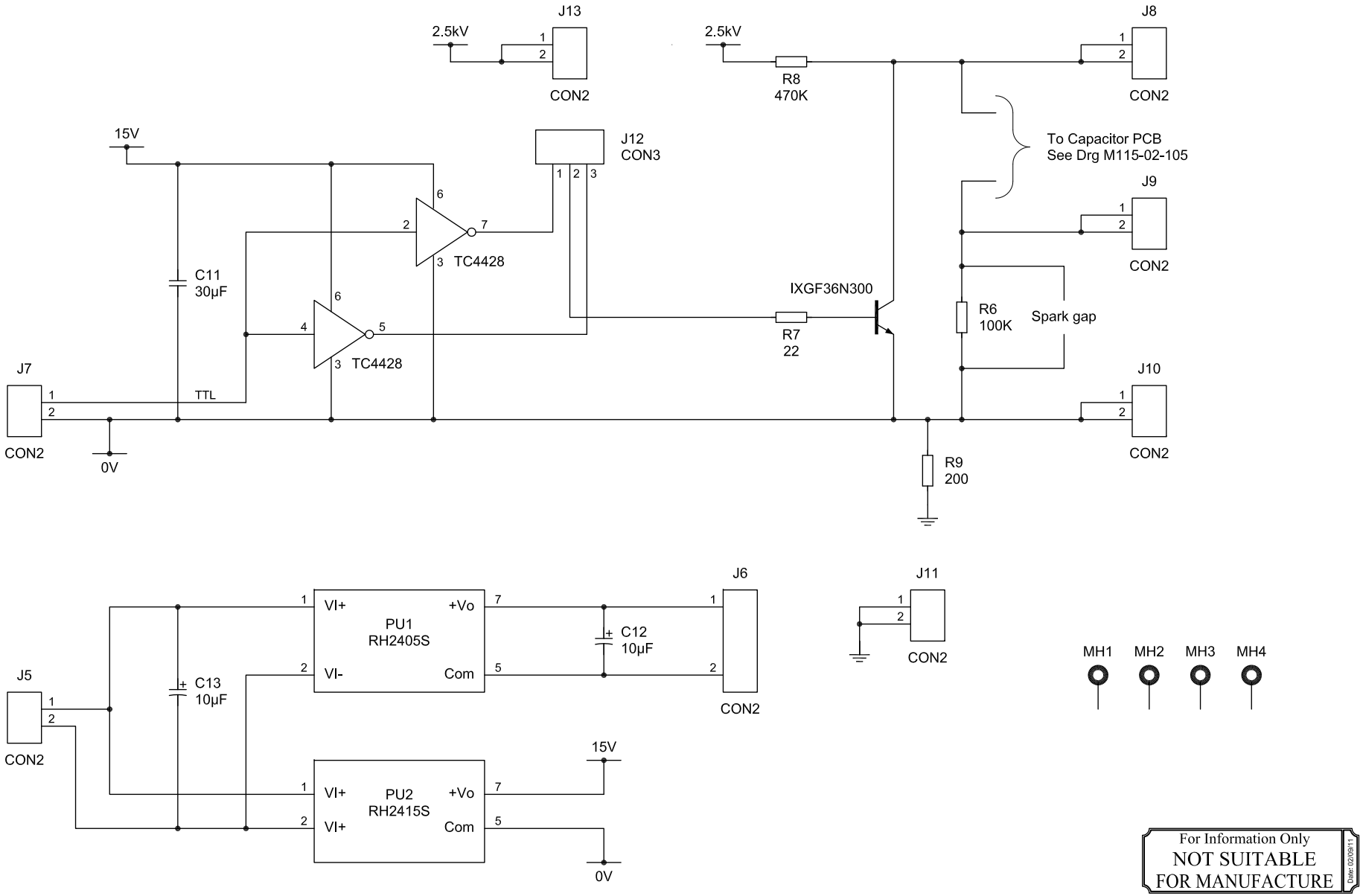

A	06/05/11	ORIGINAL	YLA			
Issue	Date	Status/Modification	Drawn	Checked	Approved	Mod. No.

Document created using * AutoCAD * Do not modify by hand

NOT FOR PUBLICATION

This Document shall not without prior written consent from CCFE be copied in whole or in part or used for any purpose other than that for which it is supplied

Dimensions in mm unless otherwise stated

Reference Drawing:

THIS DOCUMENT PRINTED : Date: 02/09/11 Time: 15:07 Hrs.

Assembly Procedure:

CADfile: M11502104

TITLE:

DSF Sparker Switching PCB Wiring Diagram

United Kingdom Atomic Energy Authority

CCFE CULHAM CENTRE FOR FUSION ENERGY

DWG. No. M115-02-104 Issue A

Quality Class: 4 Sheet No. 1 of 1 Sheets A3

Ref: EDS-A3L/JET/170107/mlv

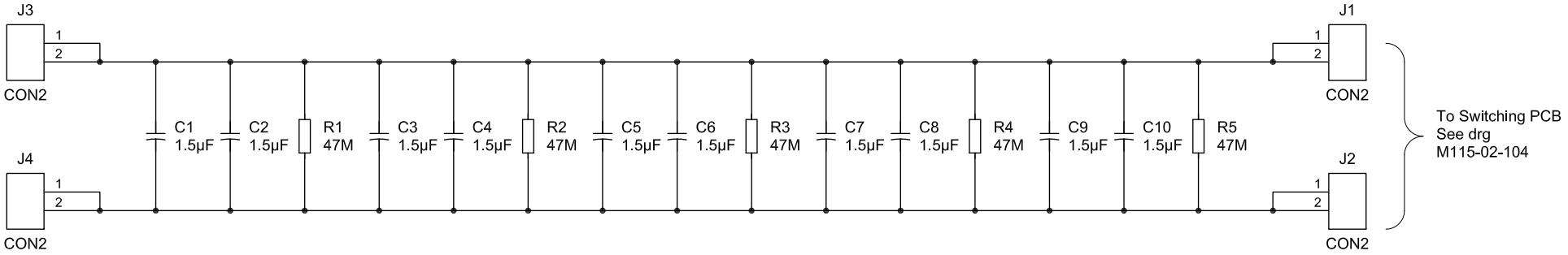

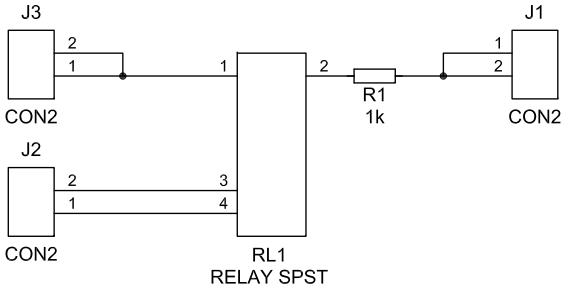

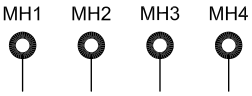

For Information Only
NOT SUITABLE
FOR MANUFACTURE
Date: 02/09/11

Document created using
* AutoCAD *
Do not modify by hand

NOT FOR PUBLICATION

Issue	Date	Status/Modification	Drawn	Checked	Approved	Mod. No.
A	06/05/11	ORIGINAL	YLA			

Dimensions in mm unless otherwise stated

Reference Drawing:

THIS DOCUMENT PRINTED : Date: 02/09/11 Time: 15:09 Hrs.

Assembly Procedure:

CADfile: M11502105

TITLE:

DSF Sparker
Capacitor PCB
Wiring Diagram

United Kingdom Atomic Energy Authority

CCFE
CULHAM CENTRE FOR FUSION ENERGY

DWG. No. M115-02-105 Issue A

Quality Class: 4 Sheet No. 1 of 1 Sheets A3

Ref: EDS-A3L/JET/170107/mlv

APPENDIX C

Commissioning and initial experiments

C.1 Commissioning and in-situ testing

The injector head was first installed on MAST on Friday 23^{rd} September 2011. Testing of the power supply was started on Wednesday 28^{th} (shot 26851) using a 300Ω dummy load without any connection to the injector head. The testing was performed during a session dedicated to other work so the spark trigger was set to 400ms, significantly after the main time of interest for the primary experiment. During this testing the capacitor bank would discharge roughly 100ms into the MAST pulse, before this time the capacitors would trigger normally, after this time no triggering was possible. No signal was observed from the current monitor during or after the voltage drop. Testing continued on Friday 30th September and the cause of the discharge was identified as the IPS box lid interlock. The magnetic relay

used in the interlock was deactivating and returning to a closed state due to the magnetic field underneath the MAST vessel. This caused the capacitors to discharge and prevented further charging. The MAST safety officer agreed that as long as the box was in-situ it would be safe to disable this interlock, provided that it was re-enabled once the IPS box was removed. Disabling the interlock solved this problem and the power supply was shown to work as expected.

The injector head was connected to the power supplies on 4th October. Although the power supplies were now known to be working and the optical trigger was being received no discharge was observed. This problem was traced to an incorrectly assembled cable and fixed the same day. The first successful firing of the injector was during pulse 26998 on Wednesday 5^{th} October.

Before injection into plasma a series of discharges at increasing voltage up to the maximum of 2.5kV were attempted into vacuum conditions. Only very small current readings were seen by the current probe and no effect was seen on any of the MAST systems. This was not unexpected as the plasma was expected to play a significant role in the breakdown. The fact that no breakdown occurred also made it unlikely that any external systems could have been affected. It was decided that test pulses into plasma shots would be required to properly test the system.

C.2 First experimental sessions - Oct 2011

Ohmic L-mode plasmas were chosen for the commissioning and initial experimental sessions. The uncertainty associated with ELMs occurring during H-mode plasma increases the complexity of both data processing and mod-

elling. It was also uncertain how the injector systems would react to high power plasmas as the injector power supplies are directly coupled to the plasma through the injector head. A relatively benign plasma would therefore be safer. Not relying on neutral beams (NBI) also removes a potential problem when running experiments.

The fixed location of the DSF and the sweeping of the MAST strike points mean that only a limited number of MAST plasma configurations are suitable for study with diagnostics on the DSF. In the large majority of pulses the strike point crosses the DSF before the current flat top is reached. Previous studies using a retarding field energy analyser fitted to the DSF[151] have developed several shots that cross the DSF at a suitable time during the shot. One of these shots, 26776, was chosen as a likely candidate for use in the carbon injection experiments. This is a low current ($400kA$) Ohmically heated shot. The MAST standard shot was also used for these experiments due to its simplicity and reliability.

C.2.1 Wednesday 5^{th} October 2011

For the first full session on Wednesday 5^{th} October it was decided to use the MAST standard shot as this was believed to be the most fail-safe approach. Unfortunately an undocumented change to the gas control system caused problems running the standard shot and the session had to be abandoned without any useful data being recorded.

C.2.2 Friday 7^{th} October 2011

During the following session on Friday 7^{th} October the injector failed to discharge. This was due to a failure of the IGBT trigger in the power supplies,

see section 2.4.3. Area entry was required to remove the power supplies and the IGBT was then replaced before the supplies were reinstalled.

C.2.3 Friday 14^{th} October 2011

The first camera data was taken on Friday 14^{th} June. The majority of these shots used MAST pulse 26776 as a reference. The spark location was varied from $\approx 4cm$ inboard of the outer strike point to $\approx 3cm$ outboard of the outer strike point. Both cameras were operated at a speed of 75kHz. A total of 17 successful shots were run in this session with shot numbers 27074 to 27090.

C.2.4 Monday 17^{th} October 2011

A follow up session was then conducted using the MAST standard shot which operates at a higher current ($770kA$) than the previous shots. Although there was excessive noise on some of these shots the image data taken was still potentially useful. A total of 10 successful shots were run in this session with shot numbers 27095 to 27103.